Improved Neutron Detection Using Zinc Sulfide with Boron

Brett Castle

Merton College, University of Oxford

Thesis submitted in partial fulfillment of the requirements for the degree of Doctor of Philosophy at the University of Oxford

Trinity Term, 2018

Acknowledgements

Firstly, I am appreciative of the financial and administrative support from the United States Air Force and its Office of Scientific Research, the department of physics at the University of Oxford, and Merton College. I am grateful to the University and Merton College for accepting me, to the United States Air Force Academy for endorsing my application, and to my mentors that set me on this life-changing path.

I am indebted to my supervisors Dr. Antonin Vacheret and Dr. Andrew Watt. Dr. Antonin Vacheret's perseverance and patience allowed me to grow as a scientist by supporting my decisions to take risks and helping me to critically analyze the results of those decisions.

Dr. Andrew Watt was indispensable in facilitating my pursuit of new ideas. He provided the resources I needed to truly explore—without these resources my learning experience would have been incomplete.

Dr. Nick Ryder and Dr. Sakari Ihantola also were immensely invaluable in this process. They listened to my ideas, challenged my thought process, and helped me from improving my code to setting up experiments.

Finally, the support of friends and family made the years of my degree enjoyable. Most importantly, I am grateful to have had this journey with my wife, Briana, and my four children. Her efforts to raise our children and support me are truly remarkable.

Abstract

Phosphor screens designed to detect neutrons by producing light are used in many applications to detect thermal neutrons including the SoLid antineutrino detection experiment. These screens are formed by binding powders of zinc sulfide and lithium-6 fluoride with an epoxy. Due to poor transparency, these screens have limited neutron detection efficiency. The current study proposes an alternate material with the potential for higher neutron detection efficiency based on sintering zinc sulfide and boron compounds to form a polycrystalline composite ceramic. A model was developed to predict neutron detection efficiency of ceramics and screens based on modifying parameters such as composition and grain size. By varying these design parameters, an optimal ceramic design was found that increased the neutron capture rate by 45% (using enriched boron) and increased the signal per neutron by 18% compared to a model of the phosphor screen used in the SoLid experiment. These design parameters were then used to fabricate ceramics by sintering commercial powders of unenriched BN and ZnS(Ag) using the FAST sintering technique. The ceramics retained the luminescent properties of ZnS(Ag) and demonstrated improved translucency. Drawbacks of this methodology include apparent carbon migration into the ceramic and difficulty reproducing the ceramics. The ceramics and a phosphor screen used in the SoLid experiment were exposed to neutrons in a custom test apparatus that collected light from either side. The results of these experiments were used to compare the neutron detection efficiency of the ceramics and the screen and compare the experimental results to the model predictions. The rate of neutrons detected and the signal produced per neutron by the ceramics were respectively 10% and 40% that of the rate and signal of the phosphor screens (the model predicted a rate roughly 35% of the phosphor screen using unenriched boron). While the experimental results did not confirm the model predictions, the effort demonstrated the feasibility of the concept and showed promise of success with further development.

Contents

List of Figures

List of Tables

Chapter 1

Neutron Detection and the SoLid Experiment

Neutrons are typically detected through nuclear reactions in target material resulting in prompt energetic charged particles that are detected using conventional radiation detection methods. An efficient detector of thermal neutrons was developed in the 1950s by combining lithium-6 fluoride (^{6}LiF–the target material) and zinc sulfide doped with silver (ZnS(Ag)–an efficient scintillating material) [1]. This combination produces a large and unique signal due to the scintillation efficiency and pulse shape characteristics of ZnS. A more efficient neutron detector was discovered with the advent of the ^{3}He proportional counters in the late 1950s/early 1960s [2]. This technology has been the predominant method for detecting neutrons until the 2000s when the source of ^{3}He became restricted due to dwindling supplies (^{3}He is the byproduct of tritium decay which is only produced in limited amounts by the US and Russia for their weapons programs) [3]. Because of this shortage, there has been renewed development of materials like ^{6}LiF:ZnS(Ag) to find alternatives to ^{3}He [3]. This thin phosphor screen has

been employed in applications ranging from time-of-flight measurements [4], material characterization using neutron diffraction [5], portal security [6,7], medical imaging [8], and antineutrino experiments [9].

The nominal neutron detection efficiency (probability of a detectable neutron signal per neutron crossing) of these screens is in the range of 23 to 34% (although Kojima, *et. al.*, claim to have developed a screen with a detection efficiency as high as 43.5%) [10–15]. This degree of efficiency represents multiple efforts over a half century to optimize the screen composition and thickness [11, 13, 14, 16]. In applications like the Short baseline neutrino Oscillations with a novel Lithium-6 composite scintillator Detector (SoLid) experiment that employs these screens, this efficiency represents the limiting factor in the overall efficiency for detecting antineutrinos. If the neutron detection efficiency of the screen could be improved, the overall efficiency of a second-generation SoLid detector (or other applications that employ these screens) would increase.

An increase in neutron detection efficiency is only possible through increasing the probability of capture. It is possible to improve the light yield of the screens; however, this will only increase the probability of detecting those neutrons captured on the screen without increasing the number of neutrons captured. Based on the similarities between the reported neutron detection efficiency and the theoretical probability of capture (both are 27%), it is expected that increasing the light yield will have minimal improvement on the neutron detection efficiency [17]. Therefore, significant improvement can only come through increasing the probability of capture. Prior efforts that increase the probability of capture, by either increasing the thickness or ^{6}Li content, found these changes had deleterious effects on the light yield and a corresponding decrease in neutron detection efficiency as a higher percentage of captured neutrons go undetected [1, 11, 13, 14, 14,

16, 18, 19].

This effort seeks to develop a material with higher probability of neutron capture, but similar form and function as the ^{6}LiF:ZnS phosphor screens to be used in a subsequent iteration of the SoLid detector. Higher probability of capture can be achieved with a material based on ^{10}B rather than ^{6}Li and has been attempted using boron nitride (BN) bound to ZnS with an epoxy like the ^{6}LiF:ZnS screens [20]. A significant disadvantage of using boron rather than lithium is the reduced energy released per neutron capture which results in diminished light yield. Modeling the microscopic structure of the material indicates a material based on boron and ZnS can achieve similar light yield and higher neutron capture if the material is fabricated without a binder, like a composite ceramic. Such ceramics were fabricated from ZnS(Ag) and BN and then exposed to neutrons to demonstrate the feasibility of this approach.

1.1 Short-baseline Antineutrino Measurements

Neutrinos, ν, (and antineutrinos—$\bar{\nu}$) are neutrally-charged leptons that are a product of flavor-changing weak interactions. Depending on the type of reaction, the neutrino is produced in one of three flavor eigenstates—electron, muon, and tau. Although neutrinos are created in one flavor eigenstate, they propagate through space in mass eigenstates that are a superposition of the flavor eigenstates. Depending on the energy and distance traveled the neutrino has some probability of being measured in different flavor eigenstates due to the superposition of mass states. The probability, $P(a, b)$, that a neutrino produced in flavor eigenstate, a, oscillates to flavor eigenstate, b, is described as,

$$P(a, b) = \sin^2(2\theta) \sin^2\left(1.27\Delta m^2 \frac{L_\nu}{E_\nu}\right), \tag{1.1}$$

where θ is a mixing angle described by the PMNS matrix, Δm^2 is the difference of the square of the mass eigenstates, L_ν is the distance the neutrino has traveled, and E_ν is the energy of the neutrino [21, 22].

This oscillatory behavior was first observed when solar and atmospheric neutrino experiments revealed a neutrino flux consistent with a model of oscillating neutrinos rather than static mass states [23–25]. Other experiments confirmed the oscillation phenomenon through measuring neutrino fluxes at short distances from reactors and neutrino beams [26]. Initially there was good agreement between the measured flux and predicted flux of these short-baseline experiments; however, when the flux models were revisited in 2011, an unexplained 5% deficit was discovered (called the reactor anomaly) [27, 28]. A similar deficit was also observed in calibration experiments of the SAGE and GALLEX detectors (solar neutrino detectors using large-volumes of gallium) using radioactive sources at a similar L/E (see Figure 1.1b) [29–31]. These deficits suggest some other phenomenon is occurring. One theory suggests this anomalous behavior is the manifestation of the neutrino oscillating at these short-baselines to another mass state that only interacts with matter via gravity and is therefore "sterile" [27, 32].

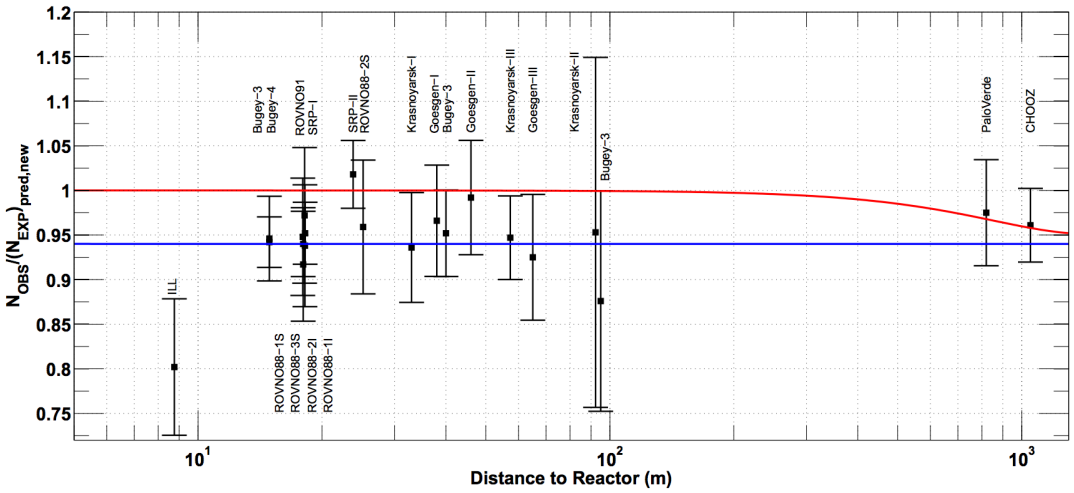

(a) Illustration of the short baseline reactor antineutrino anomaly. Experimental results are compared to a three-active neutrino mixing model (red line) and a model with a new neutrino mass state (blue line). Figure reproduced with permission from [27].

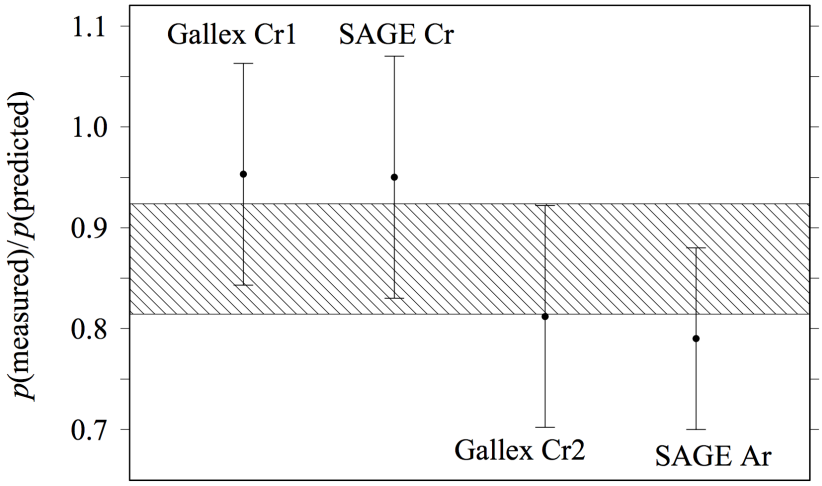

(b) Ratio of observed $\bar{\nu}$ events to the number of predicted events in the GALLEX and SAGE detectors from radioactive sources (^{51}Cr and ^{37}Ar) at close distance. Figure reproduced with permission from [33].

Figure 1.1: Anomalous observations in antineutrino data collected at short-baselines from the source. (a) Comparison of a mixing model of three active neutrino mass states (red line) with experimental results from multiple short-baseline reactor experiments shows an ~5% deficit. (b) Ratios of observed antineutrino events to the predicted in two gallium-based detectors when calibrated with portable radioactive sources at close distance. The weighted average of the four experiments (shown as the hashed region) shows a deficit in observed events from the predicted value.

Several recent reactor antineutrino measurements (RENO [34], Daya Bay [35], NEOS [36], and Double Chooz experiments) to explore the reactor anomaly all confirm the deficit from the three-mixing model, but also revealed an additional anomaly in the spectral data. Each of these experiments revealed an excess of events at 5 MeV (see Figure 1.2) that is likely to be associated with the reactor power. This additional anomaly confirms the need for better models to explain the production and nature of neutrinos associated with reactors.

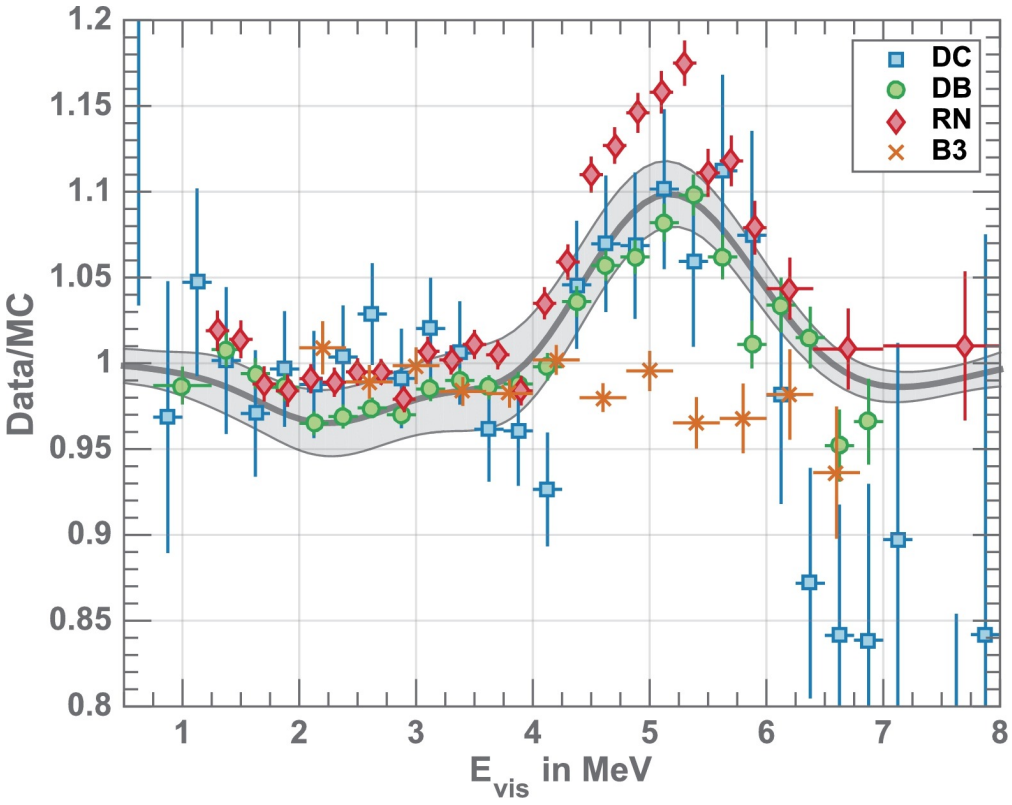

Figure 1.2: Ratio of observed reactor antineutrino spectral data to the predicted values from four short-baseline reactor experiments (Double Chooz (DC), Daya Bay (DB), RENO (RN), Bugey 3 (B3)). A global best fit of these ratios (gray curve) shows a significant deviation around 5 MeV. Figure reproduced with permission from [37].

1.2 The SoLid Experiment

The SoLid experiment aims to better understand this anomalous behavior by measuring the neutrino flux and energy spectrum a few meters from the BR2 reactor in Mol, Belgium. This facility is well-suited to short-baseline experiments as it provides the opportunity to take measurements as close as 5.5 m from the reactor core (see Figure 1.3). Furthermore, the BR2 reactor core is a compact core made of highly enriched uranium which introduces less systematic variation and produces a simpler energy spectrum than cores with mixed fuels.

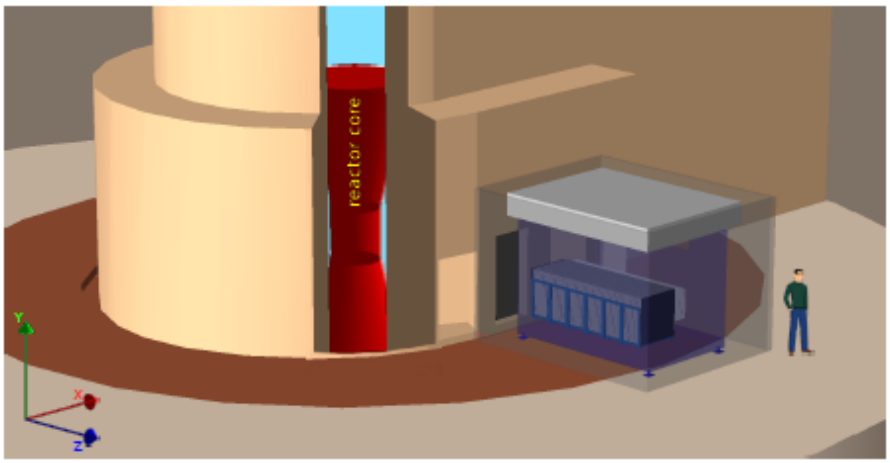

(a) Schematic of the SoLid detector at the BR2 Research Reactor. The detector consists of 1.6 tons of active material located 6.2 m from the reactor core. Figure reproduced with permission from [38].

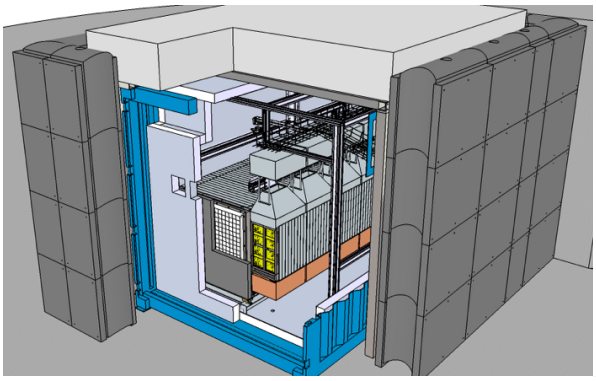

(b) Rendering of the SoLid detector. The active material and instrumentation is housed in a shipping container surrounded by water-filled containers and a slab of plastic on the roof that act as shielding. Figure reproduced with permission from [39].

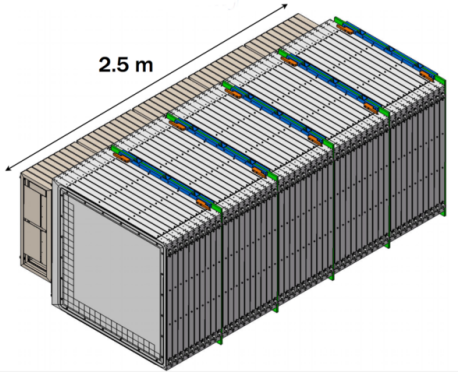

(c) The active detector consists of 5 modules. Each module consists of 10 planes. Each plane consists of 256 cubes in a 16 by 16 array and 64 channels to read out data. Figure reproduced with permission from [40].

Figure 1.3: Schematic of the SoLid experiment showing (a) the detector in relation to the reactor core, (b) the detector in a sealed shipping container and surrounded by shielding to reduce background events, and (c) the segmentation of 1.6 tons of active material.

1.2.1 SoLid Antineutrino Reconstruction

The experiment employs a novel approach to detecting neutrinos using 1.6 tons of optically-isolated segmented cubes for high fidelity event reconstruction first described in [17]. Each segment consists of a $5 \times 5 \times 5$ cm cube of scintillating polyvinyl toluene (PVT) and two 260 μm thick ^{6}LiF:ZnS(Ag) phosphor screens produced by Scintacor on the xz and yz faces of the cube. Neutrinos with energy greater 1.806 MeV interact with protons in the hydrogen-rich PVT causing the proton to undergo inverse beta decay (IBD) [41],

$$\bar{\nu}_e + p^+ \rightarrow e^+ + n, \tag{1.2}$$

producing a neutron and positron. The positron can travel up to 30 cm, causing immediate scintillation in the origin PVT cube and possibly neighboring cubes. The neutron thermalizes (the hydrogen in the PVT has a cross-section for scattering the neutron between 1 and 30 barns depending on the energy) and either captures on the ^{6}Li (cross-section of 940 barns for thermal neutrons) in the phosphor screen or hydrogen (cross-section of 330 mbarns) in the PVT or escapes the detector altogether. Those neutrons captured on ^{6}Li produce a second signal some 10s of microseconds after the positron signal as shown in Figure 1.4a (the mean time between signals is 60 μs [42]). The separation between the positron event and the neutron events is 2 cubes or less for 90% of the IBD events [42]. The waveform of signals produced from neutron capture on the ^{6}LiF:ZnS(Ag) screens is typified by an intense peak with decaying intensity that lasts a few μs (seen as the second pulse in Figure 1.4c). The light from these events is extracted by intersecting wavelength shifting fibers (WSF) which propagate the signals to photodetectors on the edge of the detector (see Figure 1.4b).

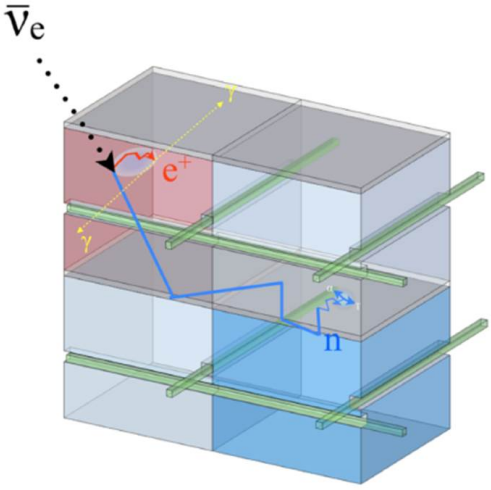

(a) IBD results in a positron and neutron. The positron causes the PVT to scintillate in the cube where the IBD occurred. The neutron travels some centimeters until captured by a phosphor screen that creates a second signal. Figure reproduced with permission from [17]

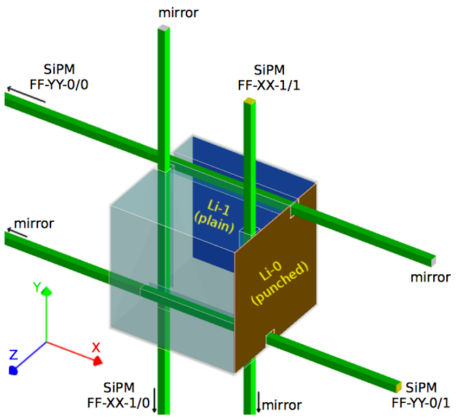

(b) The detector element consists of the PVT cube, two phosphor screens on the faces, and four WSF fibers. Signals from the IBD event are transmitted to photodetectors on the edge of the detector by the WSF.

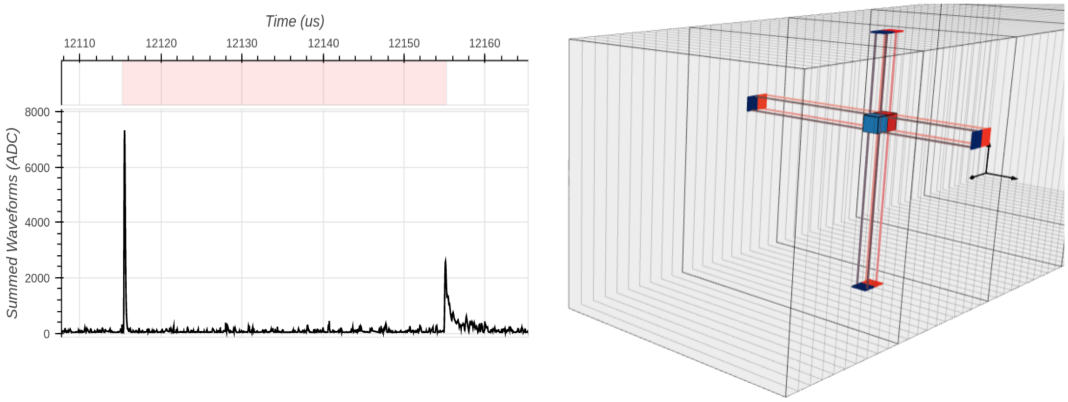

(c) Data from an IBD event in SoLid showing the time and spatial correlation of the positron and neutron signal. The positron occurs first followed by the neutron signal. The positron signal occurs in the cube highlighted in red and the neutron signal in the blue cube. Figure reproduced with permission from [42]

Figure 1.4: Illustration of IBD reconstruction within segmented cubes of the SoLid detector. (a) An IBD event results in two signals from the positron and neutron. (b) The light from these signals is collected by four WSF and transmitted to photodetectors on the edge of the detector. The orientation of the fibers allows the localization of the signal. (c) Data from an IBD event showing the relation of the positron and neutron signals both temporally and spatially.

IBD events are reconstructed from events recorded within a space-time region relative to the readout trigger. Due to the high rate of reactor gammas that mimic the IBD positron, the readout trigger is designed to trigger solely on the unique waveform of IBD neutrons [42]. The algorithm to identify the neutron signal uses a rolling tally of local maxima within a time window known as the trigger variable (see Figure 1.5). When the trigger variable exceeds 14 peaks on any channel, all events within a space-time region relative to that channel is read out. This space-time region consists of all channels within 3 planes and all events 500 μs before and 200 μs after the trigger event utilizing a history time buffer [42]. This allows for offline reconstruction of the IBD event topology.

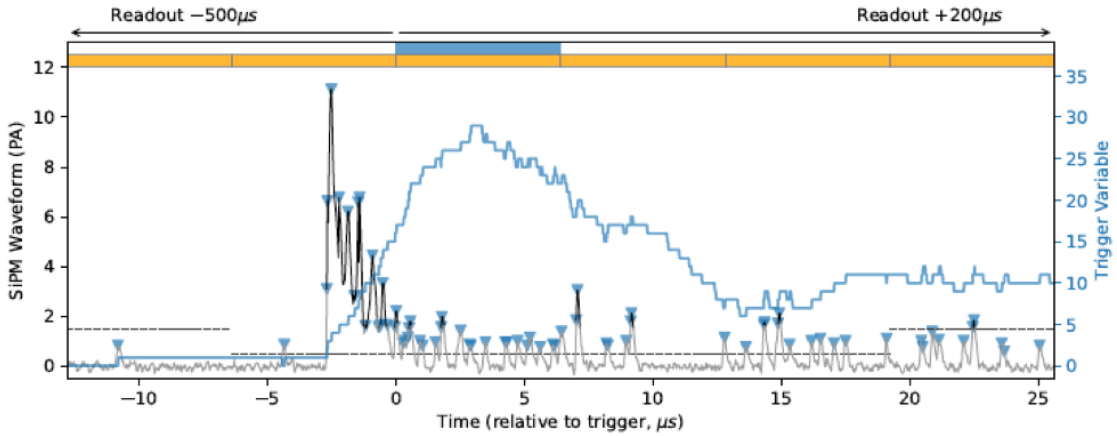

Figure 1.5: Example of SoLid trigger using the unique neutron waveform (solid black line) from [42]. The neutron signal from ZnS(Ag) is typified by an intense peak followed by peaks of decaying intensity over an $O(1)$ μs. The trigger variable (solid blue line) is a rolling tally of local maxima (blue diamonds) that exceed 0.5 PA over a window of 256 samples (6.4 μs). For this illustration, the readout is triggered if the trigger variable exceeds 14 peaks, although the nominal trigger variable threshold is a more restrictive 17 peaks. Figure reproduced with permission from [42]

1.2.2 Neutrino Efficiency and Sensitivity

IBD detection efficiency is the ratio of IBD events recorded to the total IBD interactions and is dependent on properties of neutron detection within the detector. The IBD detection efficiency is a product of the probability, P, of successfully reconstructing the IBD event given an IBD neutron was detected, the neutron detection efficiency, $\epsilon_{\text{neutron}}$, and the percentage of events lost to cutting the background, Γ,

$$\epsilon_{\text{detector}} = P(\text{IBD reconstruction} \mid \text{neutron detected}) \times \epsilon_{\text{neutron}} \times \Gamma. \tag{1.3}$$

The IBD reconstruction is a product of the efficiency of detecting the positron and the probability the positron is within the space-time region of the readout when triggered by the neutron event. As the positron readily interacts with the PVT, the positron efficiency is solely based on the amplitude of the positron signal, the efficiency of collecting that light and converting it to an electronic signal, and the threshold set to eliminate noise and background. The positron efficiency is estimated to be greater than 80% [17]. It is estimated the positron has no less than 90% probability of being within the space-time readout considering the mean time between events and the spatial separation discussed in Section 1.2.1. This implies the probability of IBD reconstruction given a neutron is detected is in excess of 0.72 and is probably greater than 0.95.

Neutron detection efficiency is the product of the probability of capture on a phosphor screen and the probability the signal meets the criteria to trigger the readout,

$$\epsilon_{\text{n}} = P(\text{neutron capture}) \times P(\text{neutron detection} \mid \text{neutron capture}). \tag{1.4}$$

The probability of detecting the neutron given a neutron was captured on the screen is

dependent on the signal meeting the trigger criteria which is related to the light yield, the efficiency of light collection and conversion, and the trigger criteria itself. This is also known as the trigger efficiency. The neutron trigger efficiency for SoLid was measured using an AmBe source and models to predict the deficit, resulting in an estimated trigger efficiency of near 80% [42]. The estimated probability of neutron capture per crossing of the Scintacor screens is 27%. With two screens per cube, the neutron will cross a screen on average 2.4 times equating to a total probability of capture of 66%, as shown in the results of simulations conducted in [17] (see Table 1.1). Not all of the captured neutrons result in a detectable signal. Consequently, the detector has a total neutron detection efficiency of 52%. Neutrons not captured on a screen either escape the detector or are captured by other nuclei like the hydrogen in the PVT cubes.

Table 1.1: Probability of Capture Based on the Number of Phosphor Screens Per Cube. Table reproduced with permission from [17].

Number of phosphor screens	Probability of neutron capture in phosphor screen	Mean time from IBD event until neutron capture in screen (μs)	Probability of neutron capture in PVT
1	0.51	102	0.28
2	0.66	65	0.17
3	0.73	49	0.12

The last factor related to the IBD efficiency is offline analysis related to separating background from signal. Some sources of background, like fast neutrons, radioactive contamination, or coincidental backgrounds create a series of signals that trigger the readout and mimic an IBD. An experimental challenge of conducting the experiment at the BR2 reactor is the increased background created by the scarce over-burden to shield the detector from high-energy particles generated by cosmic ray showers. Offline analysis is used to eliminate these events.

With this offline analysis, the reported IBD detection efficiency of the detector is 42% [17]. Given an estimated probability of IBD reconstruction of 0.95 and a neutron detection efficiency of 0.52, (1.3) would suggest the purity of the offline cuts is about 85%. The IBD efficiency could be improved by increasing the probability of neutron capture. Not only would this increase the neutron capture efficiency it would also reduce the mean time between events which would allow for a more stringent space-time readout that would eliminate some background and improve the purity cut. A quantified illustration of how increased neutron capture would improve the IBD efficiency is provided in Section 1.5.1

1.3 Neutron Detection

Neutrons are subatomic particles found in all isotopes except ^{1}H. The strong nuclear interactions provided by neutrons allow protons to overcome repulsive Coulombic forces to form a stable nucleus. Outside the nucleus, neutrons are unstable and will transform to a proton via beta decay with a half-life of about 10 minutes.

$$n \rightarrow p^+ + e^- + \bar{\nu}_e \tag{1.5}$$

Free neutrons are therefore a signature of a nearby nuclear reaction. These reactions might include radioactive decay, spontaneous fission, induced fission, fusion, spallation, or inverse beta decay (and hence a signature of an antineutrino).

Neutron detection relies predominantly on detecting the products of the strong interactions with nuclei in the target material—namely scattering (either elastic or inelastic) or capture. These products are commonly γ or ions. Neutrons that elastically collide

with nuclei of low mass—like hydrogen, lithium, and sometimes carbon—impart sufficient energy to the recoiling nucleus to produce a detectable signal in the surrounding medium. Some nuclei have high cross-sections for inelastic collisions that cause the nucleus to assume an energetic state. De-excitation typically results in the emission of a characteristic spectrum of gammas. Finally, neutron capture by some nuclei result in either emission of a γ or fission of the nucleus, which produces energetic recoiling ions.

Particular isotopes have higher probabilities for these reactions making them better suited for use in neutron detection. The probability of these reaction is called a cross-section, and is measured in units of area (the most common unit is the barn which is 10^{-28} m^2). This cross-section is based on the isotopic nuclear structure and the neutron energy. Table 1.2 provides the examples of cross-sections for capture of thermal neutrons (~0.025 eV) for many common isotopes used in neutron detection. As the energy of the neutron increases, the cross-section changes, as shown in Figure 1.6.

Table 1.2: Thermal neutron capture cross sections for isotopes common to neutron detection.

	Cross Section (barns)	
Isotope	Capture	Scattering
Hydrogen-1	0.33	30
Helium-3	5 300	3.9
Lithium-6	940	0.78
Boron-10	3 800	2.3
Cadmium-113	20 000	25
Gadolinium-157	250 000	1 000

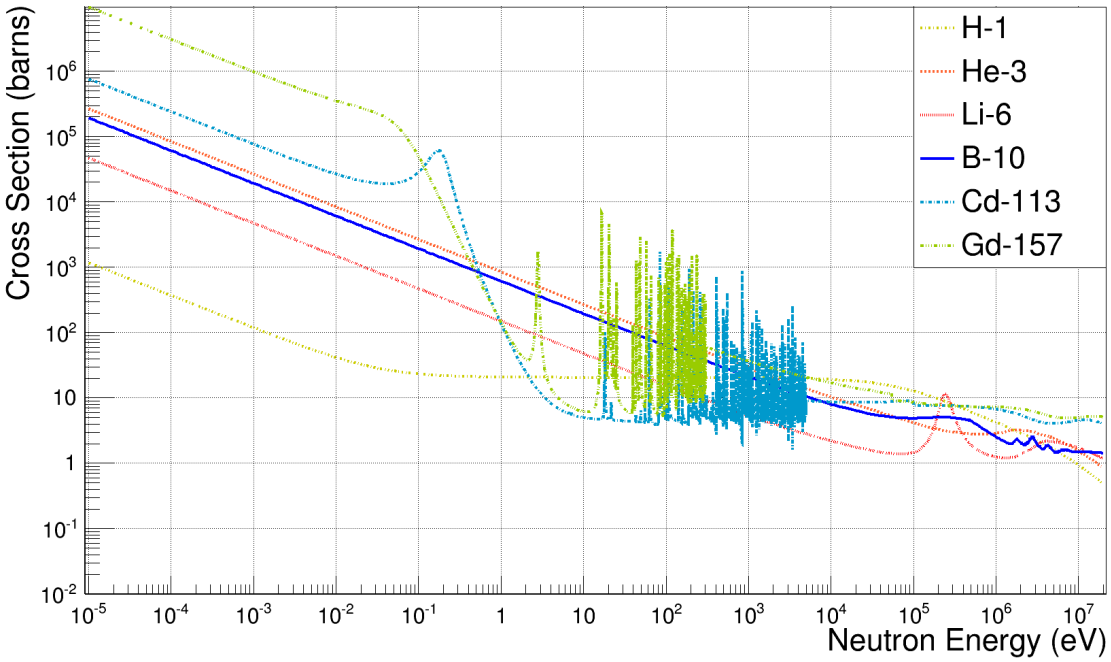

Figure 1.6: Total cross sections for nuclei common to neutron detection [43].

Neutron detection efficiency was introduced in (1.4) as the product of the probability of neutron capture and the probability the signal from the products of the capture are detected given the capture occurred. More general terms of neutron detection efficiency would modify this equation to include all interactions in addition to capture. The probability a neutron interacts with the material depends on the cross-section, σ, and the total number of isotopes available in the volume of the detector. For neutrons traveling along a path of length, t, the probability of interaction can be estimated by,

$$P = 1 - e^{-t\sigma N}, \tag{1.6}$$

where N is the isotopic density of the material.

Identification efficiency—the number of events identified as a neutron given a neutron interaction occurred—incorporates numerous elements including signal produc-

tion, collection, and analysis in addition to the background-to-noise present during data collection. Because the signals produced are stochastic in nature, not all signals are distinguishable from background and signal analysis is often needed to identify the neutron events. Identification efficiency in general can be improved through increasing the magnitude and uniformity of the signal, limiting the number of background events, and improving the techniques to differentiate the signal from noise. Many systems incorporate materials with high probability of neutron interaction and that produce large enough signals to easily identify the event.

A common background that is prevalent in many applications detecting neutrons is gammas. All active neutron detectors that detect the byproducts of a neutron interaction, whether a semiconductor, gas detectors, or scintillating detectors, are all sensitive to gammas as well as neutrons. Furthermore, the energy deposited by gammas in these detectors is often similar in energy to the energy deposited by the neutron byproducts. This means simple amplitude discrimination is often insufficient (unless the detection method is based on identifying characteristic gammas from neutron capture, in which case the background are gammas that have energies coinciding with the signal).

One means of discriminating gammas from neutrons is using pulse-shape discrimination. Gammas typically deposit energy over a large volume, whereas heavy ions produced from neutron capture deposit energy in a very small volume within the detecting medium. This high ionization density can result in changes in the signal produced by the medium. This is one reason why ^{6}LiF:ZnS(Ag) phosphor screens are preferred in many neutron detecting applications.

1.4 LiF:ZnS Phosphor Screens

Based on their form and function, the ^{6}LiF:ZnS(Ag) phosphor screens have relatively high neutron detection efficiency. This is in large part due to the scintillation efficiency and pulse shape characteristics of ZnS(Ag) powders. ZnS(Ag) was one of the first phosphors discovered [44] and has a reported scintillation efficiency between 75 000 [45] and 90 000 [46] photons per MeV making it one of the most efficient scintillators (as shown in Figure 1.7).

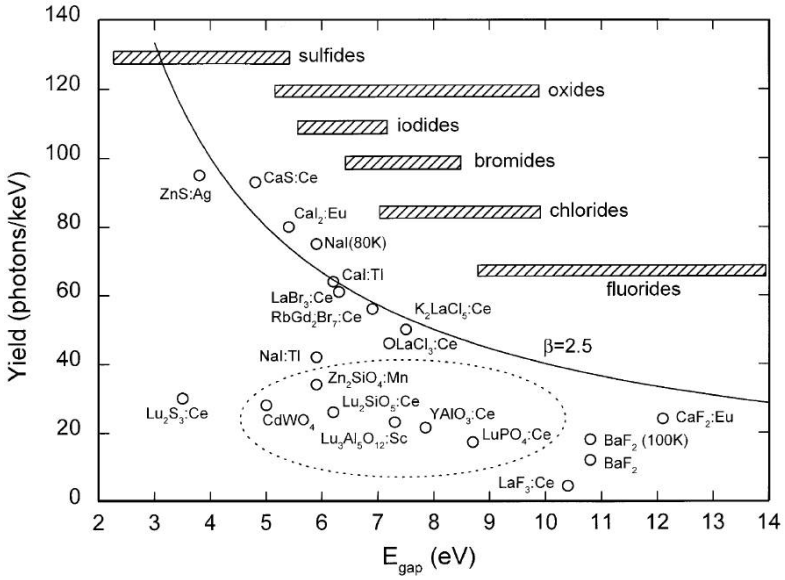

Figure 1.7: Light yield of scintillators and cathode ray tube phosphors. Figure reproduced with permission from [46].

In the 1950s, these screens were adapted to detect neutrons by incorporating compounds with hydrogen, lithium, boron, thorium, or uranium [47]. Most studies found ^{6}Li preferable to other isotopes due to the amount of energy released upon capturing a thermal neutron despite its relatively low cross-section (see Table 1.2) [48]. When ^{6}Li

captures a neutron, it decays into a triton and α particle via the exothermic reaction:

$$^{6}\mathrm{Li} + \mathrm{n} \rightarrow \ ^{3}\mathrm{H}\,(2.73\mathrm{MeV}) + \alpha\,(2.05\mathrm{MeV}) \tag{1.7}$$

The charged particles travel some tens of microns in the phosphor material (approximately 6-12 μm for the α and 30-70 μm for the triton [49]) in opposite directions. These particles scatter off the atoms in the ZnS(Ag) resulting in excitation or ionization. The resultant free charge carriers will cause secondary and tertiary free carriers as they thermalize to the bottom of the conduction band. The population of free carriers migrate in the conduction band until captured by a luminescent center, which then relaxes producing a photon [50].

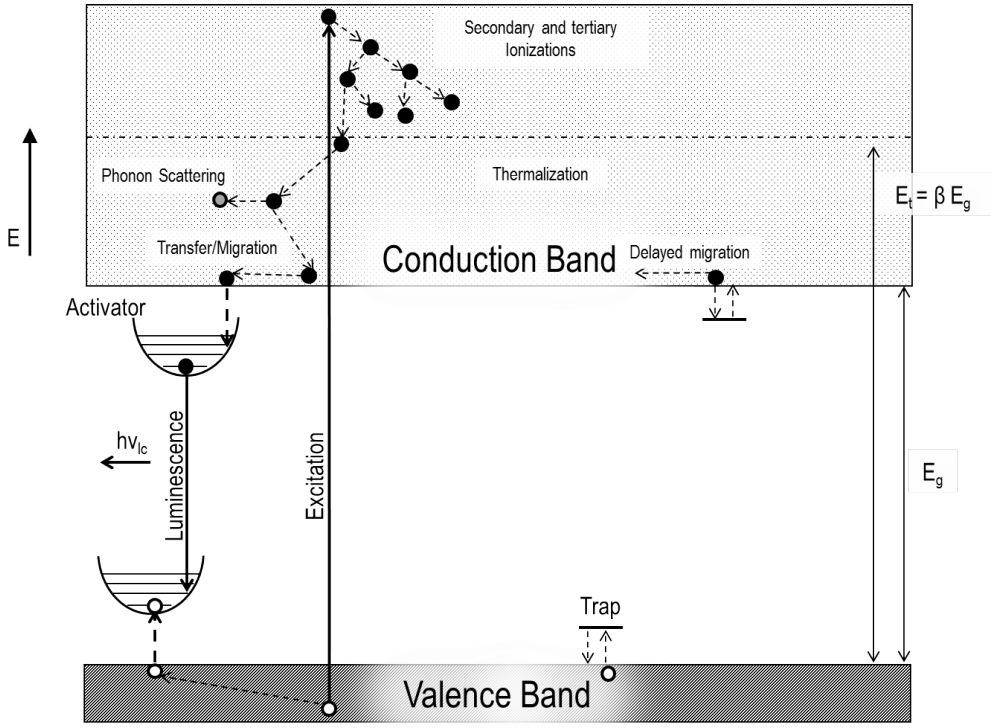

Figure 1.8: Schematic of scintillation process in inorganic crystal via impurities/defects.

The specific energy loss related to the triton and α result in delayed luminescence which contributes to pulse shape discrimination (PSD). The high specific energy loss of these particles (discussed in more detail in Chapter 2) results in the deposition of a significant amount of energy in a small volume which equates to high ionization density. The high ionization density saturates local luminescent centers which leads to capture of charge carriers on more distant luminescent centers and a higher likelihood of charge carriers being captured by trap states [51].

The delayed capture of charge carriers by the luminescent centers results in delayed scintillation that is distinguishable from scintillation caused by gammas. The scintillation from a neutron is distinguished by the exponentially decaying intensity over some

microseconds after the initial pulse (as shown in Figure 1.5) [52]. This distinct signal from the ^{6}LiF:ZnS(Ag) screens is a significant part of successful IBD reconstruction in SoLid.

The difference in neutron and gamma signals is supported by independent experiments of other ^{6}LiF:ZnS(Ag) products. Figure 1.9 shows the response of Eljen EJ-426HD2, a ^{6}LiF:ZnS(Ag) screen of 500 μm thickness and 1:2 ratio, to neutrons from Cf-252 (blue trace) and gammas from Cs-137 (red trace).

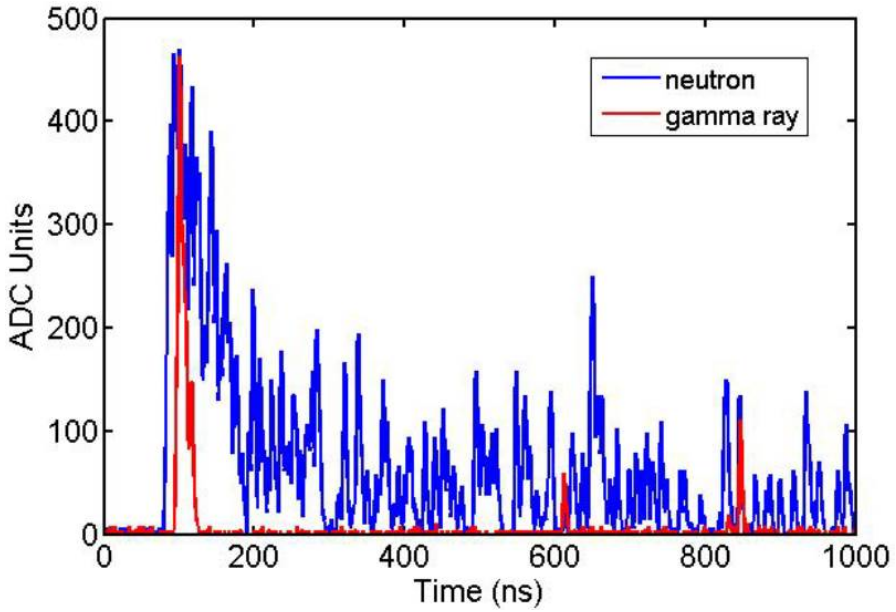

Figure 1.9: Example pulses of scintillation from an Eljen EJ-426HD2 screen due to excitation from a γ from Cs-137 and a neutron event from Cf-252. Figure reproduced with permission from [53].

The light emitted from ^{6}LiF:ZnS(Ag) phosphor screens has been estimated to be between 160 000 [54] and 174 000 [11] photons per captured neutron. In two studies comparing the light yields of neutron sensitive materials, ^{6}LiF:ZnS(Ag) phosphor screens produce two to three times the light over the next brightest material [45, 54]. The light yield and the distinctive pulse created by neutrons are key factors in the neu-

tron detection efficiency.

The neutron detection efficiency of these phosphor screens ranges from 23 to 34% [10–15]. This efficiency represents the results of over a half century of work to optimize the screens through controlling parameters such as the ratio of ^{6}LiF to ZnS to binder, the thickness, the grain size of the particles, and the type of binder. Mass ratio studies all conclude the optimal ratio of LiF:ZnS is between 1:2 and 1:4 [11, 13, 14, 16]. At these ratios, it is estimated only 1.3 to 1.8 MeV of the 4.78 MeV released is transferred to the ZnS [55]. Increasing the percentage of ^{6}LiF content beyond these ratios would reduce the average amount of energy deposited in ZnS resulting in a higher population of low-intensity signals that are indistinguishable from background. At these ratios, the optimal thickness of the screens is between 250 to 500 μm. Greater thicknesses result in greater opacity which similarly produce a higher population of low amplitude signals [1, 14, 18, 19]. Based on the results of these efforts, it appears only slight gains in neutron capture and detection efficiency are possible through revisiting the optimal parameters of the ^{6}LiF:ZnS(Ag) screens. This effort looks to develop a new material with similar form and function as an alternative to the phosphor screens.

1.5 Improvement to Neutron Efficiency through Composite Ceramics

An alternative material with improved performance requires increased probability of capture while maintaining similar levels of identification efficiency. Increased probability of capture comes with higher amounts of neutron-sensitive material or materials with isotopes of higher cross-sections than ^{6}Li. The design choices made to increase

the probability of capture must also consider means to maintain the intensity of the signal. Furthermore, any alternate material should have similar form (i.e. an easily handled solid of similar dimensions), function (peak wavelength of emission and distinct neutron pulse shape), and cost.

One possible material solution is a polycrystalline ceramic made from commercial powders of ZnS(Ag) and boron. Such a material could achieve a higher probability of capture, can be fabricated to dimensions approximating the phosphor screen, maintain the emission characteristics of ZnS, and is potentially cheaper. Higher probability of capture from a material based on ^{10}B rather than ^{6}Li is expected due to the differences in cross-section (shown in Table 1.2). Natural boron also has a higher abundance of ^{10}B (20%) compared to ^{6}Li in natural lithium (7.5%). This is a likely reason that ^{10}B is five to ten times cheaper than ^{6}Li. ZnS and many boron compounds are also conducive to high-temperature manufacturing processes such as sintering. Sintering alleviates the need for a binder (which detracts from the energy transferred to ZnS) and offers the potential for improved transparency which would reduce attenuation losses [56–60].

The disadvantage of using ^{10}B as the neutron sensitive isotope is the energy of decay products. ^{10}B typically produces a ^{7}Li, α, and γ; but occasionally only produces the former two, as shown in,

$$\begin{aligned} {}^{10}\mathrm{B} + \mathrm{n} \rightarrow {}^{11}\mathrm{B} \rightarrow {}^{7}\mathrm{Li}\,(0.84\mathrm{MeV}) + \alpha\,(1.47\mathrm{MeV}) + \gamma\,(0.48\mathrm{MeV}) \quad 94\% \\ {}^{10}\mathrm{B} + \mathrm{n} \rightarrow {}^{11}\mathrm{B} \rightarrow {}^{7}\mathrm{Li}\,(1.01\mathrm{MeV}) + \alpha\,(1.78\mathrm{MeV}) \quad 6\%. \end{aligned} \tag{1.8}$$

The difference in energy released per neutron capture and the shorter particle range (on the order of 2 to 5 μm [49]), means less energy is likely to transfer to ZnS. This discrepancy can be overcome by optimizing the ratio of boron to ZnS and taking advantage of

the improved transparency resulting in similar or better energy deposition in ZnS than the phosphor screens—while still increasing the probability of capture.

A boron and ZnS(Ag) ceramic has the added benefit of potential cost-savings due to the price differential between ^{10}B and ^{6}Li. Furthermore, the optimal ratios are likely to require significantly less boron by weight. With improved neutron detection efficiency at a lower cost, such a material should improve the data collection efficiency and cost of the SoLid detector.

1.5.1 Redesigning Neutron Detection with Boron and ZnS Powders

Replacing the phosphor screens in SoLid with a boron and ZnS based ceramic offers the potential to improve the probability of capture while retaining the light yield and excellent PSD provided by ZnS. These factors lead to improved neutron detection efficiency, IBD efficiency, sensitivity, and cost for a follow-on SoLid detector. The IBD efficiency of a modified detector was estimated by simulating neutron capture in a model of the detector using Monte-Carlo N-Particle version 6 (MCNP6). The model consists of $3 \times 3 \times 3$ PVT cubes with a 260 μm thick ceramics on every xz and yz face as currently configured in SoLid. Adding more cubes to the simulation was found to have little effect on the results and the $3 \times 3 \times 3$ cube arrangement had the best agreement with results reported in [17]. The simulation originated thermal neutrons at a random location in the center cube and then tallied each capture within the ceramic. The IBD efficiency is assumed to be proportional to probability of capture or the number of neutrons captured by a ceramic divided by the number of simulated neutrons. This assumption represents a worst-case scenario where the IBD trigger efficiency remains constant, when it is expected to improve with the reduction in mean time between positron and neu-

tron signal. It is also assumed that the signal produced by the ceramics is similar to the phosphor screens. The results of the simulation using varying ratios of ^{10}B:ZnS are presented in Table 1.3. A ratio of 80:1 ZnS to ^{10}B in the two-screen configuration demonstrates the similarities between the probability of capture per crossing and the total probability of capture estimated in [17], *et. al.*, (see Table 1.1) for the un-modified detector. From these simulations, it is apparent that improving the neutron capture efficiency through the ceramics has the potential to improve the overall IBD efficiency of a second-generation SoLid detector.

Table 1.3: Improvements to IBD Efficiency from Improving the Probability of Capture per Crossing

Mass ratio ZnS:^{10}B	Probability of capture per crossing	Probability of capture on a screen	IBD efficiency	Mean time until capture (μs)
80:1	0.26	0.69	0.44	42
50:1	0.37	0.77	0.48	36
25:1	0.60	0.84	0.53	29
15:1	0.76	0.87	0.55	26
7.5:1	0.93	0.89	0.57	24

Table 1.3 also shows how improving neutron capture efficiency reduces the time until neutron capture which will reduce the coincidental background and improve sensitivity. Per [17], using cuts based on a mean time of capture of 65 μs after the positron signal, the coincidental background occurs at a rate of 0.09 Hz. This is a significant rate of background events in comparison to the expected rate of 7.3 $\times 10^{-3}$ Hz for IBD events. Reducing the mean time of capture would reduce this background rate based on the distribution of background events for a given Δt. Reducing this window also reduces the data cache requirement for positron events.

Finally, the screens represent a significant cost to the detector and replacing them with a cheaper material would represent substantial cost-savings. With just two screens per cube, the screens represent 30-50% of the total material costs of the entire detector. The cost of the screens is likely due to the cost of procuring enriched lithium, and was the prime reason a third screen was not added to each cube to improve the neutron detection. If the ceramic can be manufactured at 10-20% the cost of the phosphor screens, this would reduce the cost of the neutron sensitive material in SoLid to just 4-17% of the total cost of the detector.

A simple estimate of the neutrinos recorded per day reveals how improving the neutron detection efficiency (and consequently IBD efficiency) can impact the overall experiment. Operating at a nominal power of 60 MW, the BR2 reactor should produce $\sim 1.2 \times 10^{19}$ ν s^{-1} or $\sim 1.04 \times 10^{24}$ ν per day [61]. Once emitted, antineutrinos travel isotropically from the source in all directions. A fraction will pass through the detector determined by the area of the detector normal to the incoming antineutrinos divided by $4\pi r^2$, where r is the detector distance from the source. $5 \times 5 \times 5$ cm^3 cubes are arranged in 50 planes of 16 cubes by 16 cubes with all planes normal to the detector (see Figure 1.3a) presenting an area of 0.64 m^2. At 6.5 m from the reactor core, 0.12% of the antineutrinos produced in the reactor will pass through the detector, or about 1.25×10^{21} per day when the reactor is on. Based on an expected IBD cross section (on the order of 10^{-44} cm^2), an estimated flux of 5.2×10^{22} ν per cm^3, and a detector thickness of 250 cm; up to 1 600 antineutrinos will cause an IBD in the detector. Based on an estimated detector efficiency of 42%, about 630 of these IBD events are recorded per day. Improving the probability of capture per crossing to 60% improves the IBD efficiency to 53% which would result in 848 IBD events recorded per day or 35% increase.

1.6 Summary

^{6}LiF:ZnS(Ag) screens are efficient neutron detectors for many niche applications with neutron detection efficiencies in the range of 23-34%. A polycrystalline composite ceramic of ZnS and a boron compound offers an alternative to these phosphors screens with the potential to improve the neutron detection efficiency at a lower cost. This would improve the effectiveness of applications from nuclear security to experimental particle physics like SoLid.

The expected changes to light yield were explored through simulating neutron capture and charged particle transport through models representing the micro-structures of the phosphor screens and ceramics. The results of these modeling efforts demonstrate the plausibility of the ceramics exceeding the neutron detection efficiency of the screens and provided insights into fabricating the ceramics. Ceramic fabrication was focused on demonstrating the feasibility of fabricating a composite ceramic from commercial ZnS(Ag) and BN powders. While multiple sintering methods are possible, this effort focused on the FAST technique. Finally, the ceramics were exposed to neutrons to confirm whether the ceramics could detect neutrons and make comparisons to the phosphor screens.

Chapter 2

Predictive Model of Neutron Detection Efficiency

This chapter discusses the models developed to predict a ceramic design that exceeds the neutron detection efficiency of the ^{6}LiF:ZnS(Ag) phosphor screens. Neutron detection efficiency can be modeled using a combination of mathematical models and Monte-Carlo simulations to estimate neutron capture, energy deposition in ZnS, and the attenuation of light as it transports out of the material. Parameters of thickness, composition, and grain size were optimized in these models to find a ceramic design that exceeds the detection efficiency of the screens.

As discussed in Chapter 1, neutron detection efficiency is a product of the probability of neutron capture and light yield. Probability of neutron capture is dependent on the microscopic cross section of the neutron capture isotope and the density of those isotopes within the material. Light yield is a product of the energy deposited in ZnS per neutron capture, the scintillation efficiency of the ZnS, and the transparency of the material. A ceramic based on ^{10}B offers a four-fold increase in microscopic cross-section, but

introduces a roughly two-fold decrease in energy released per neutron capture. The reduced energy per neutron capture requires optimization of the ceramic design to achieve similar light yield to the phosphor screens. Otherwise, the signals produced by the ceramic may be below threshold for detection within the SoLid data acquisition.

The neutron detection efficiency is estimated using simulations and mathematical models that represent the processes involved in neutron detection. Neutron capture efficiency is essentially a macroscopic phenomenon and can be modeled using simple mathematical models or Monte-Carlo simulations. Because the charged particles released from neutron capture only travel between a few to tens of microns, the energy deposition in ZnS is highly dependent on the microscopic grain sizes and composition of the material. This microscopic phenomenon is simulated using Monte-Carlo methods and represents the bulk of this modeling effort.

Light yield is also dependent on the scintillation efficiency of ZnS and the attenuation of the light as it travels out of the material. The scintillation efficiency is dependent on the chemical composition and the grain size of ZnS, but is beyond the scope of this effort and therefore was assumed to be a constant between the ceramic and screens. Attenuation is based on the scattering and absorption of light which is dependent on several microscopic factors within the material. Estimating the impact these microscopic features have on the attenuation length is also beyond the scope; therefore, estimates of attenuation were limited to simplified mathematical models based on the thickness and a macroscopic average attenuation length. This attenuation length was also assumed constant between the ceramics and screens.

The products of these separate processes were combined to predict neutron detection efficiency. Each piece is validated against either experimental results or similar model. The bulk of the validation focused on comparing the simulated energy deposi-

tion to simulations using a similar model and comparing the simulated total light yield to experimental results. The accuracy of these models is based on the accuracy of the known physical parameters. Some parameters, such as binder density, were unknown and therefore were estimated based on likely possibilities. Consequently, additional simulations were conducted to explore the validity of the model based on the range of these unknown parameters.

After validation, the neutron detection efficiency of the Scintacor screen was estimated to determine the benchmark for efficiency. Then the approach was applied to hypothetical ceramics based on feasible compositions, thicknesses, and grain sizes. Due to the lack of binder in the ceramic, the model used in the Monte-Carlo energy deposition simulations was modified. These modified models could not be validated as the ceramics are a novel concept with no experimental or simulated precedence.

2.1 Model

Neutron detection efficiency as described in (1.4) is compartmented into the probability of capture and the probability of detection given a neutron was captured. Efficiency is modeled based on this compartmented approach by simulating a flux of neutrons through the material to determine how many neutrons are captured and then simulating the processes to generate a signal to determine whether the signal would meet the threshold for detection. The processes from neutron capture to signal processing in this approach are illustrated in Figure 2.1.

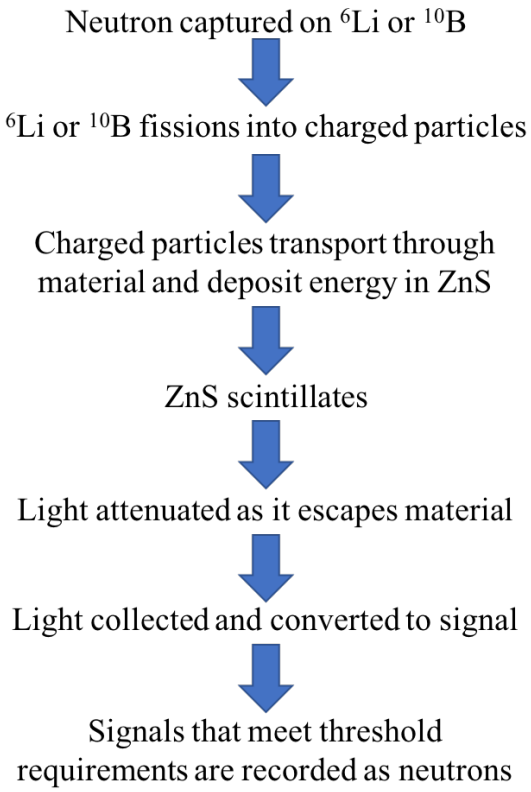

Figure 2.1: Process flow of neutron detection.

The simulations used to model these processes as they relate to neutron detection efficiency is illustrated in Figure 2.2. The model is limited to material properties and does not attempt to estimate system-level efficiencies such as light collection or signal analysis other than using a simple threshold.

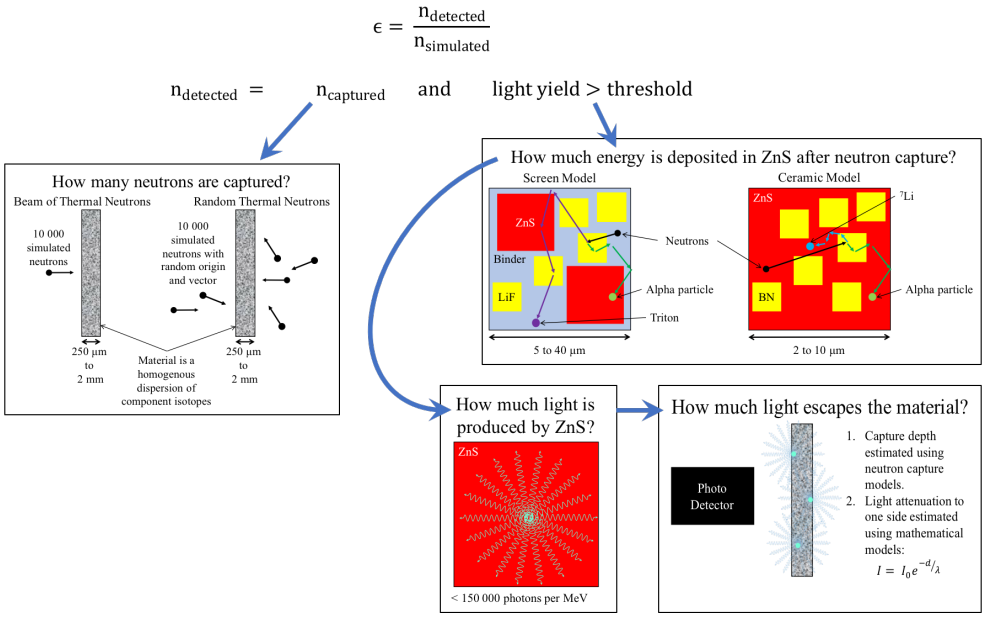

Figure 2.2: Approach to simulating neutron detection efficiency. Neutron detection efficiency was compartmented into an estimation of the number of neutrons captured and an estimate of the light escaping the material relative to a detection threshold. The light escaping the material was estimated using a combination of energy deposition simulations, an estimate of scintillation efficiency, and a model for the attenuation of light. A neutron is "detected" if it is captured and the light yield escaping to one side of the material exceeds an arbitrary threshold for detection.

Facets of this approach are similar to previous efforts to estimate aspects of neutron detection through modeling. The first computer-aided simulation estimated energy deposition in ZnS by approximating the phosphor screen as thin slabs of alternating ZnS and LiF [62]. This crude approximation neglected the affects due to the binder and the individual grains of ZnS and LiF. Stephans, *et. al.*, improved upon this model by representing ZnS as randomly dispersed microscopic spheres suspended in bulk material approximated as lithiated glass. Particle transport was simulated using a modified version of TRIM [63]. Yehuda approximated the phosphor screen as spheres placed in an ordered structure resembling a face-centered cubic (FCC) lattice [64]. This approach is

computationally much simpler than approximating randomized micro-structures; however, early attempts by the author to use this same approximation found this geometry requires altering the sphere size to unrealistic dimensions to match the macroscopic mass ratios. This geometry also tends to overestimate the energy deposition in ZnS—a trend found in other efforts using ordered micro-structures to approximate stochastic dispersion [65].

More recently, Herzkamp developed a model that randomized spheres in a box to mimic the microscopic structure of the phosphor screens and used GEANT4 to simulate the transport of the capture products through the material to estimate the energy deposition in ZnS. This model had relatively good agreement with experimental results [55]. Herzkamp took the model further by estimating the number of photons escaping one side of the material for a neutron capture event using,

$$N_{\text{exit}} = E_{\text{dep}} \cdot C \cdot \alpha_l(x). \tag{2.1}$$

For each event, E_{dep} is sampled from the simulated probability distribution using the GEANT4 model, C is the estimated scintillation efficiency of ZnS, and $\alpha_l(x)$ is the loss due to attenuation at an event depth, x, (measured from the edge of the material where detection occurs). The event depth is sampled from an exponential distribution based on the neutron attenuation length. Herzkamp's approach is taken further in this effort to estimate the neutron detection efficiency by comparing the output from (2.1) to some threshold for detection.

2.1.1 Monte-Carlo N Particle version 6

The model developed for estimating neutron detection efficiency is dependent on Monte-Carlo simulations to simulate neutron and charged particle transport through the material. These simulations are predominantly executed in Monte-Carlo N-Particle version 6 (MCNP6) because of its rich history of validation [66]. The foundations of MCNP began with the U.S. nuclear weapons program to predict criticality. Today, MCNP6 is widely used in defense, nuclear power and safety, and academia. The ability to simulate a variety of particle interactions or phenomenon including particle scattering and capture make this tool ideal for the current problem.

2.1.2 Neutron Capture

The fraction of neutrons captured by the material can be estimated using a mathematical model like equation (1.6) or MCNP6 simulations. Equation (1.6) provides a simplistic estimate of neutron capture that neglects interactions with isotopes other than the neutron capture isotope, assumes a mono-energetic neutron, and assumes the path is normal to the material surface. The accuracy of the model is largely dependent on the accuracy of the measured thickness and estimated isotopic density of neutron-sensitive isotopes.

MCNP6 simulations can incorporate the stochastic nature of neutron transport and capture through the material. This improved realism provides more accurate estimates of neutron capture. Using both methods, however, provides some confirmation and cross-check of the validity of the estimate.

Like the mathematical model, the accuracy of the MCNP6 estimate is dependent on values used for thickness, composition, and isotopic density to model the material. These values were gathered from the available information or inferred from common

values where applicable. For the mathematical model, the isotopic density was calculated using,

$$N = \frac{R_{\mathrm{NC}} \cdot E \cdot F_A}{M \cdot \sum \frac{R_i}{\rho_i}}, \tag{2.2}$$

where R is the mass fraction of the neutron capture compound, E is the percent enrichment, F_A is the number of neutron capture atoms per molecule, M is the molar mass of the neutron capture compound, and the summation in the denominator sums the mass fraction divided by the density of each compound included in the material. For the MCNP6 simulations, the mass fraction of each atom had to be calculated along with the overall density of the material. The mass fraction of each atom was calculated by,

$$A = \frac{M_A \cdot F_A \cdot R_{\mathrm{molecule}}}{M_{\mathrm{molecule}}}, \tag{2.3}$$

where M_A is the molar mass of the atom, R_{Molecule} is the mass fraction of the molecule that consists of the atom. For molecules including the neutron capture isotope (either lithium and boron), the atomic fraction of individual isotopes had to be accounted for which required a separate calculation for each isotope that included the enrichment. The density of the material for the MCNP6 simulations was calculated using

$$\rho_{\mathrm{material}} = \frac{1}{\sum \frac{R_i}{\rho_i}}. \tag{2.4}$$

Each calculation was made using reported mass ratios and enrichment. Where density was not reported, ideal densities of the compounds were used. In the case of the phosphor screens, the binder density is rarely reported requiring an estimated density based on common binders.

The MCNP6 models were designed to estimate neutron capture given a standard

flux of 100 000 thermal neutrons. These standard fluxes provide a systematic means of comparing neutron capture. Two scenarios were used to generate the flux depending on the application of the model. The first scenario simulates thermal neutrons originating from at a point source 1 mm from the face of the material with a uniform trajectory along the normal axis. This scenario was used to estimate a general comparison of neutron capture and when comparing models to experimental results where the neutron source was stationed on one side of the material and the neutrons were collimated. The second scenario generates thermal neutrons at a random position outside of the material and given a random direction. The space outside the material where neutrons originated was bounded with a reflecting boundary to reflect all neutrons back towards the material. This ensures all simulated neutrons pass through the material and are eventually captured. This scenario was used to estimate the depth of neutron capture within the material.

Materials are modeled as a cuboid of 5×5 cm with a thickness of 250 μm (or of varying thickness to explore how this parameter impacts overall detection efficiency). The cell around the shape was absent of any material simulating a vacuum so as not to interact with the neutrons prior to their incidence on the surface. The number of neutrons captured in the cell are tallied and normalized to the number of simulated neutrons. When estimating the neutron capture depth, the material is essentially segmented into bins based on the normal distance from the face of the material.

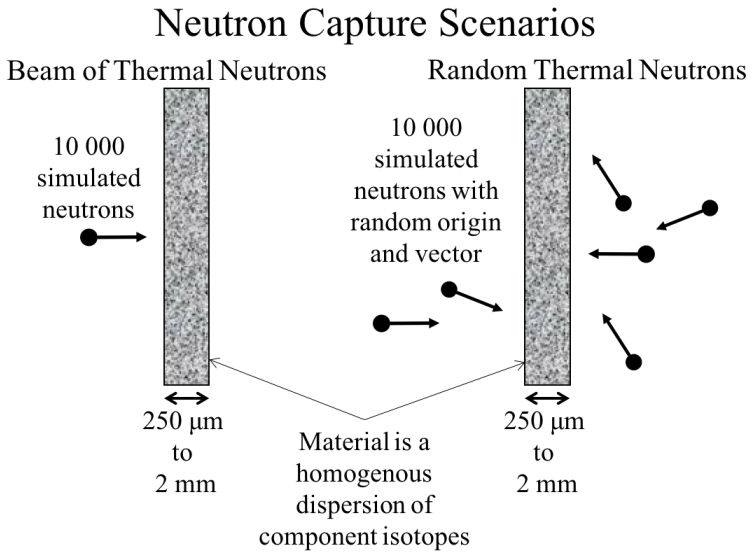

Figure 2.3: Rendering of simulations used to model neutron capture.

2.1.3 Energy Deposition in ZnS

After neutron capture, ^{6}Li and ^{10}B fission into charged particles consistent with equations (1.7) and (1.8), respectively. These particles travel in opposite directions a distance of a few microns up to tens of microns. As the particles scatter through interactions with atoms in the environment, their paths resemble a random walk. Energy is transferred via Coulombic interactions with atomic electrons for each scattering event until the particles reach thermal equilibrium.

The amount of energy deposited in ZnS will depend on the number of scattering events that occurred within the ZnS and the particle velocity whilst traveling through the ZnS. Because the particles' paths most closely resemble a random walk and the distance traveled is on the order of the grain sizes of the particles, the amount of ZnS encountered along the random walk is dependent on the constituent ratio of ZnS in the material, the grain size of the material constituents, and the origin depth within the

neutron capture grain. These factors all have a stochastic nature and therefore contribute to the consequent statistical distribution of energy deposition in ZnS.

The velocity of the particle, v, whilst traveling through the ZnS impacts the rate of energy loss (also known as the specific energy loss), S. This dependence is illustrated through the mean rate of energy loss described in the Bethe-Bloch formula [67],

$$\left\langle -\frac{dE}{dx} \right\rangle = -Kz^2\rho\frac{Z}{A}\frac{c^2}{v^2}\left[\frac{1}{2}\ln\frac{2m_e v^2\gamma^2_{\text{Lorentz}}W_{\max}}{I^2} - \left(\frac{v}{c}\right)^2\right], \tag{2.5}$$

where K is,

$$K = \frac{1}{(4\pi\epsilon_0)^2}\frac{2\pi N_A e^4}{m_e c^2}, \tag{2.6}$$

I is the effective ionization potential of the material averaged over all atomic electrons ($I \sim 10Z$ eV) [68], and $W_{\max}$ is the maximum amount of energy transferred in a scattering event [67],

$$W_{\max} = \frac{2m_e v^2\gamma^2}{1 + \frac{2\gamma m_e}{M} + \left(\frac{m_e}{M}\right)^2}. \tag{2.7}$$

Based on these equations, it is apparent the energy transferred to ZnS will change with changing particle velocity. With each interaction and the corresponding transfer of energy, velocity decreases resulting in an increase in the specific energy loss until it reaches a maximum. After this maximum, the specific energy rapidly decreases with decreasing particle velocity. Accordingly, much energy is deposited near the end of the particle track where the particle is traveling slower and specific energy loss is greatest. This increase in specific energy loss at the end of the track is known as the Bragg peak [19]. Figure 2.4 shows the Bragg peak using a SRIM simulation for the particles relevant to neutron capture on ^{10}B and ^{6}Li traveling through zinc sulfide. The Bragg peak for the ^{7}Li particle is not apparent as the particle velocity is low enough that the

specific energy maximum has already been exceeded.

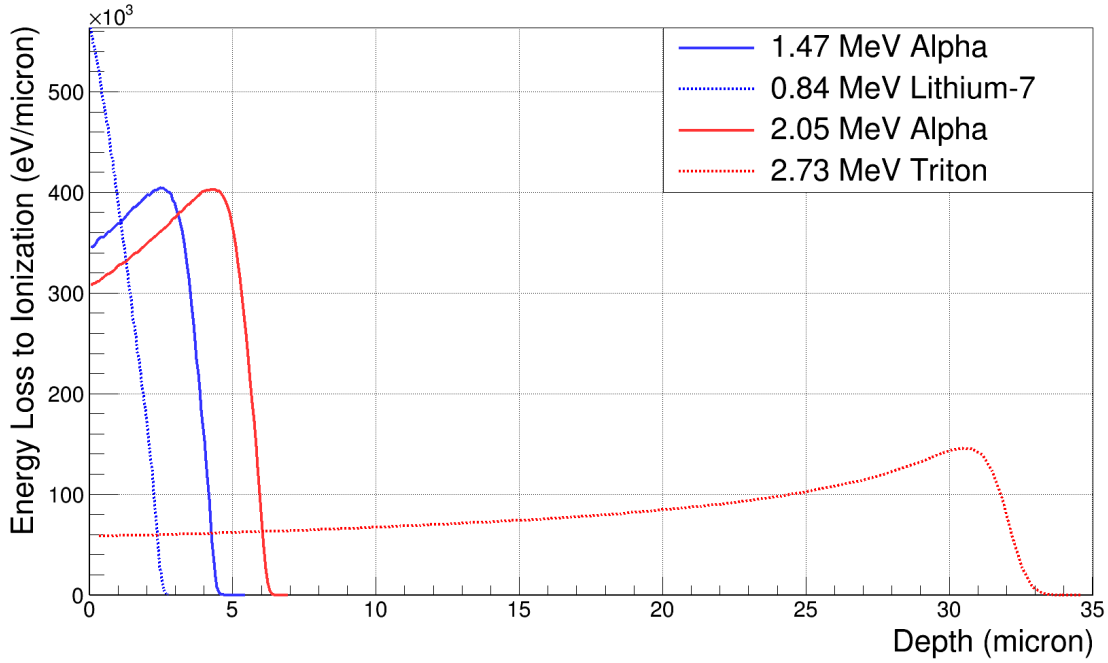

Figure 2.4: Specific energy loss for particles of a neutron capture on ^{10}B (in blue) and ^{6}Li (in red) traveling through zinc sulfide [49].

The specific energy loss has some dependence on the material properties of the transport medium and characteristics of the particle. The specific energy loss dependence on material density, ρ, is linear. The nuclear composition (i.e. Z/A) of the target material only varies slightly from 1/2 and therefore creates a minor difference. Charge, z, has a significant impact when the particles are heavy and highly-ionized.

To estimate the energy deposited in ZnS, neutron capture, the consequential generation of charged particles, and their subsequent transport and thermalization was simulated using an MCNP6 model representing a microscopic "cell" of the material. The modeled "cell" consists of a box enclosing small randomly-distributed cubes representing the various constituent grains within the material. Randomization of the cubes is achieved by segmenting the box and assigning each cube at random to an available seg-

ment. The position of the cube within the segment is also randomized. This prevents unrealistic overlap of grains and but also prevents grains from touching to meet constraints of the simulation. The size of each cube is assigned a value based on average values reported in other efforts, by the manufacturer, or selected to explore the impact of changing dimensions. To reduce computational burden and ensure proper mass ratios, no attempt was made to replicate the stochastic nature of grain size. Grains of the constituents more closely resemble polyhedrons, but cubes might be considered the worst-case scenario. Using cubes also reduces the computational burden of generating random polyhedral shapes. The number of interior cubes and the size of the outer box were selected based on the macroscopic mass ratio of the constituents. The particulars of how these models were applied to the phosphor screen and ceramics is described in greater detail in subsequent sections.

Each MCNP6 simulation tracked 10 000 thermal neutrons originating from a random location within the box (excluding cubes representing the neutron capture grains). Neutron transport was simulated as a random walk through the cell until captured by one of the grains of neutron capture material which then generated the corresponding charged particles consistent with equations (1.7) and (1.8). Simulation of the neutron transport and capture provides a more accurate representation of where capture occurs within the grain relative to the grain boundary and provides ease in simulating the random and correlated vectors of the charged particles. The simulation continued with tracking the random walk of the charged particles through the cell from their origin. As the particles pass through each material, the energy deposited in the material was estimated using built-in energy deposition tallies. In MCNP6, “tallies” are used to record the information of interest for each simulated particle. The resultant tally of energy deposited in ZnS for each simulation was binned and presented as histograms representing

the probability of energy deposition in ZnS.

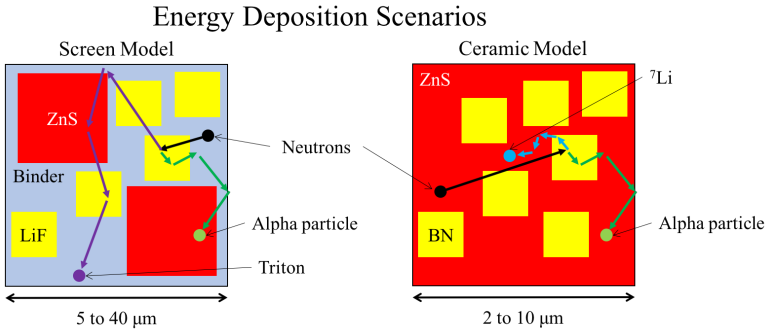

Figure 2.5: Rendering of simulations used to model energy deposition.

To ensure all neutrons and charged particles remain within the cell, the boundaries of the box were set to reflect all particles. Reflecting boundaries simplified the simulations and essentially created an infinite lattice of alternating mirror images of the box. This contrivance introduced long distance order to the model and potential for bias in the estimates. To ensure one particular cube arrangement did not bias the results, the simulations were repeated for 100 randomized arrangements. The histograms of energy deposition for the 100 randomizations were then averaged.

Because this model focuses on microscopic processes, it does not account for macroscopic phenomenon like edge effects. Neutrons captured near the edge of the material create a higher probability that the charged particles escape the material without depositing all their energy. Using additional MCNP6 simulations for the macroscopic material, it is estimated that less than 7% of all capture events result in significant edge-effect losses and that loss is more prevalent for tritons in the phosphor screens than for the α or ^{7}Li particles in a boron-based ceramic.

Model of Phosphor Screens

Applying the random-cube model to the phosphor screen includes two types of interior cubes representing ZnS and LiF. The intermediate material between cubes represents the binder (see Figure 2.6).

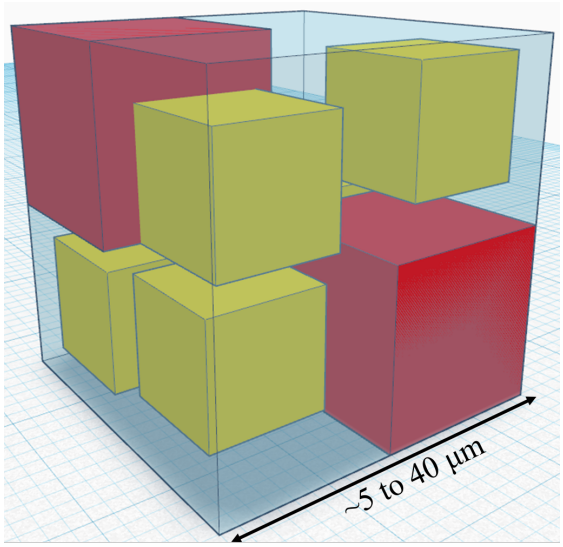

Figure 2.6: Rendering of the random-cube model applied to a ^{6}LiF:ZnS screen. The ZnS is represented as the red cubes; LiF as yellow cubes; and the binder as the transparent blue of the large cube. ZnS cubes first fill a random quadrant within the cell and then LiF cubes occupy the available space at random positions such that there is no overlap between cubes.

The number of cubes used in each scenario is based on the mass ratio of the scenario, the dimensions of the cubes, and the density of each material. The density of ZnS and LiF is assumed to be 4.09 and 2.635 g cm^{-3}, respectively, based on common values. The binder used in these scenarios is modeled after either polyethylene or polydimethylsiloxane based on the scenarios. Polyethylene is mentioned as the binder in the Spowart report, therefore, scenarios simulating these screens use C_2H_4 as the composition [12]. The actual binder used by the Scintacor screens is unknown; but, based on an unpub-

lished report, the composition is understood to include hydrogen, carbon, oxygen, and silicon in a 6:2:1:1 ratio, which resembles polydimethylsiloxane, C_2H_6OSi. The density of either binder is also unknown. Consequently, a density of 0.93 g cm^{-3} was selected for use with both binders; however, when comparing the Spowart simulated screens to the Herzkamp results, the binder density was increased to 1 g cm^{-3} to be consistent with Herzkamp's estimation of the binder density. As the binder density presents a large unknown, additional SRIM simulations were conducted to see how binder density affects the particle track length and comment on the limitations of the model with this unknown.

The grain size of the ZnS and LiF also represents a large unknown. The Spowart report claims an optimal ZnS grain size of 10 μm and mentions LiF grain sizes of 7 μm although these values were never explicitly cited as the actual grain sizes in the screens studied [12]. Herzkamp also used a ZnS grain size of 10 μm to simulate the Spowart screens, but uses a LiF grain size of 2.5 μm consistent with other simulated screens [55]. For the Scintacor screens, the simulations used a base ZnS grain size of 5 μm and a LiF grain size of 2 μm. These values were selected based on typical grain sizes reported by manufacturers, various reports (including Herzkamp's [6, 55, 69]), and SEM images of the screens presented in Chapter 3 (see Figure 3.23).

Model of Ceramics

For scenarios involving ceramics, the random-cube model was modified to approximate the resultant material from sintering. During sintering, the grains of BN remain roughly unchanged while ZnS grains grow into the volume of the surrounding voids. The ceramic model fills the outer box with ZnS rather than binder and only cubes of boron are placed at random within the segmented box. This configuration resembles particles sus-

pended in a matrix which has been used in previous modeling efforts [63]. This model makes no attempts to include residual voids or control the separation between boron compounds which is expected to be dependent on the distribution of ZnS grain sizes. Presumably finer ZnS grains allow the boron compounds to be more evenly dispersed whereas larger grains might force BN to coalesce resulting in greater heterogeneity.

The ratio of boron to ZnS is controlled by changing the number of cubes and the size of the outer box. In most scenarios, the number of cubes was kept at 12 and only the dimensions of the outer box were changed to modify the amount of ZnS. This value varied between 2 to 10 μm. A few scenarios mandated minimal segmentation of the box (i.e. 8 segments) and therefore required the number of cubes be less than 8.

Although these ceramics could be fabricated with a variety of boron-compounds such as pure boron, boron carbide, and boron oxide, the models focused on boron nitride as the compound of choice (a limited number of scenarios using other boron compounds were included to explore potential benefits of these alternatives). Hexagonal boron nitride powder is a cheap source of boron and is easily incorporated in the sintering process. To approximate the graphite-like shape of hexagonal BN, the cubes were modified such that one dimension was always 0.5 μm. The other dimensions were kept at 1 μm consistent with dimensions reported by manufacturers. The BN cuboid is also randomly rotated such that the short dimension is normal to one of the three axes, as shown in Figure 2.7. The density of BN used in all these simulations is 2.29 g cm^{-3}, consistent with manufacturer specifications.

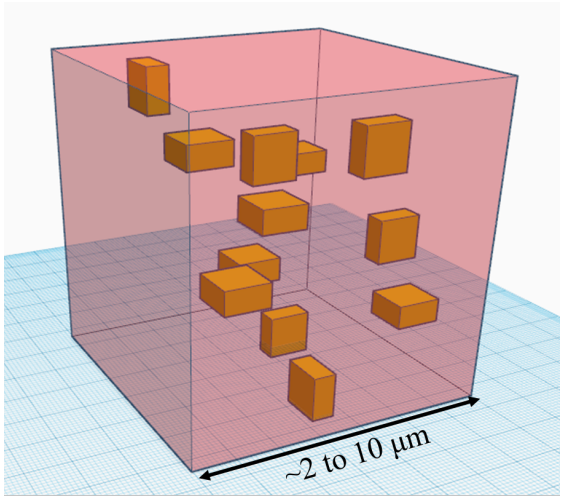

Figure 2.7: Rendering of an average cell of a ceramic using randomized cubes. The ZnS is represented as the transparent red cube and boron nitride as the random yellow cubes.

2.1.4 Scintillation Efficiency of ZnS

With estimates of energy deposition in ZnS, it is possible to estimate the number of photons generated per neutron capture. This estimate is based on the scintillation efficiency of ZnS (the process of scintillation was introduced in Section 1.4; specifically, see Figure 1.7) . The scintillation efficiency describes the amount of energy converted to light and is often described as energy efficiency, η, or light yield, L. Energy efficiency is the ratio of energy converted into photons and light yield is the number of photons created per unit of energy deposited in the scintillator. Energy efficiency can be represented as [50],

$$\eta = \frac{\alpha_{\text{e-h}}}{\beta_{\text{threshold}}} \frac{h\nu}{E_g}. \tag{2.8}$$

where $h\nu$ is the energy of the emitted photon, and E_g is the band gap of the host crystal. In the case of ZnS(Ag), the energy of the photon is about 2.76 eV (450 nm wavelength)

and the band-gap energy of bulk sphalerite (cubic) ZnS has been reported as 3.54 eV [70]. The other two terms represent various aspects of the scintillation process. $\alpha_{\text{e-h}}$ is the ratio of e-h pairs that radiatively recombine to emit a photon compared to the total number of electron holes created (i.e. $\alpha_{eh} = (N_{ph}/N_{eh}) \leq 1$). This value is typically 0.9±0.1 for common phosphors [71]. $\beta_{\text{threshold}}$ is threshold coefficient that accounts for losses in the excitation process. One model attributes these losses to vibronic coupling and thermalization of carriers in excess of the requisite energy to excite a carrier above the band gap [72]. The theoretical minimum of the threshold coefficient for ZnS is 1.5 and is based on conservation of momentum and energy for the generation of free carriers [50]. Experimental measurements of the threshold coefficient indicate the value to be 2.9±20% with an energy efficiency of 21% for ZnS(Ag) [71].

Light yield, L, is a measure of the number of photons per MeV and is often a more relevant quantity in experimental measurements. Related to energy efficiency, light yield is simply [50]:

$$L = \frac{\alpha_{eh}}{\beta_{\text{threshold}} E_g} \tag{2.9}$$

In the ideal case, $\alpha_{eh} = 1$, resulting in a theoretical light output of roughly 150 000 photons MeV^{-1} for ZnS(Ag). Experimental measurements of light yield from ZnS(Ag) have been reported from 75 000 [45] to 90 000 [46] photons MeV^{-1}. The range in values for the reported light yield is not surprising considering this value can vary based on parameters such as grain size, dopant concentration, crystalline phase, etc. For the purposes of predicting the neutron detection efficiency, the light yield is assumed to follow a normal distribution centered on the theoretical value of 150 000 photons MeV^{-1}, unless otherwise specified for unique scenarios.

2.1.5 Attenuation of Light

Not all light emitted by the ZnS will escape the material. This loss in light can be a significant determining factor whether a neutron is detected or not. Therefore, the model for neutron detection efficiency developed in this effort accounts for the attenuation of light escaping the screen using mathematical models. These models treat the phenomenon macroscopically using an average attenuation length and a prediction of the origin of the light in relation to the depth within the material.

Light is scattered and absorbed by the many grain boundaries and defects in the material. The simplest model of the attenuation of light is an exponential decay function,

$$I = I_0 e^{\frac{-x}{\lambda_l}}, \tag{2.10}$$

where x is the depth of the origin of the light normal to the surface and λ_l is the average attenuation length of the material. This model approximates the attenuation length based on the mean free path of photons through the material. It also assumes light travels normal to the surface of the material.

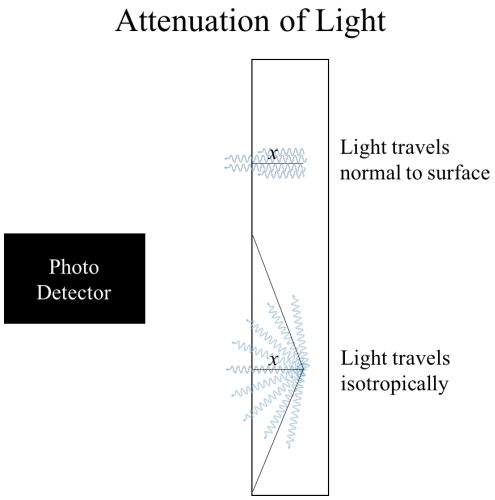

Figure 2.8: Rendering of scenarios considered for attenuation.

Light emitted from scintillators travel isotropically, meaning most of the path lengths are longer than the shortest path to escape the material, and consequently experiences greater attenuation. A more complete model would account for the additional attenuation experienced as light travels at larger angles from the normal. Herzkamp, *et. al.*, developed a correction factor to account for the conical projection of light escaping to one side of a material [55],

$$\alpha_l(x) = \frac{1}{2}\left(e^{-\frac{x}{\lambda_l}} - \frac{x}{\lambda_l}\int_{\frac{x}{\lambda_l}}^{\infty}\frac{e^{-y}}{y}dy\right). \tag{2.11}$$

This model assumes the light originates from a point source and does not account for any reflection at surfaces. The transport of the charged particles after neutron capture may result in some dispersion of light over the few to tens of microns the particles travel. When the light reaches the surface, there will be some reflection due to the change in index of refraction. Light that is incident on the surface with an angle that exceeds the critical angle will reflect into the sample and not be transmitted. SoLid also

uses phosphor screens with a diffuse reflective backing on one side which increases the amount of light detected per event. This model does not account for either of these effects.

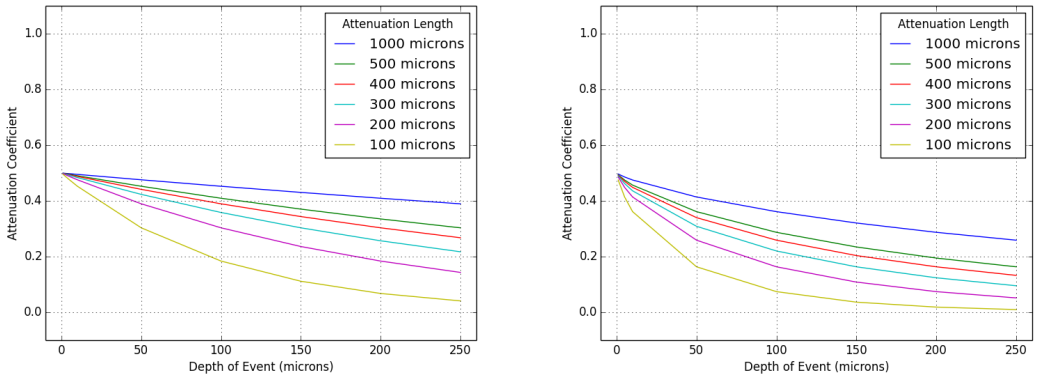

(a) Without correction for isotropic dispersion.

(b) With correction for isotropic dispersion.

Figure 2.9: Attenuation coefficient for different depths and attenuation lengths, (a) without the correction for isotropic dispersion, and (b) with the correction.

Overall, equation (2.11) should provide a more accurate estimation of losses due to attenuation than the simple attenuation model. Figure 2.9 shows how the attenuation length and the correction term for isotropic dispersion impact attenuation. Considering the worst-case scenario, namely light originating at the far-side of the material, about 3% of light is lost for every 100 nm reduction in attenuation length. Based on previous measurements by the SoLid collaboration and others, it is expected that the attenuation length of the phosphor screens is on the order of hundreds of microns and is estimated to decrease with increased ZnS content [55]. However, without precise measurements or a microscopic model of photon transport through the material, it is difficult to estimate the actual attenuation length of the material. For this model and for comparison, the attenuation length is approximated to be 410 μm for both the Scintacor screen and

ceramics which is based on approximations made by Herzkamp [55].

The thickness and depth of capture are also important parameters in this model. 250 μm is the thickness reported for the screens studied by Spowart in [12] and the approximate thickness of the Scintacor screens. In the Spowart measurements a collimated neutron source is directed at the screen from the side opposite the light collection. This results in the depth of the capture event, x, resembling an exponential distribution,

$$P_n(x) = e^{\frac{-x}{\lambda_n}}, \tag{2.12}$$

where, λ_n is the neutron attenuation length given by,

$$\lambda_{\mathrm{n}} = \frac{1}{N\sigma}, \tag{2.13}$$

where N is the isotopic density and σ is the cross-section for thermal neutron capture introduced in Chapter 1. Isotopic density is estimated based on mass ratios, molar ratios of the various compounds, and an estimated enrichment of 95%.

This scenario of a collimated neutron source from one side is not consistent with the SoLid experiment where neutrons are expected to be incident from all angles and therefore represents the worst-case scenario where the distribution of capture events is biased to the side of the material furthest from the light collection. In the case where neutrons originate from both sides, the distribution is expected to be equally weighted to either side. Furthermore, because the incidence occurs at random angles, more events are expected to be biased towards the sides rather than the interior of the material. Figure 2.10 presents results of MCNP6 simulations demonstrating the effects of capture depth within a screen based on the location of the source and the ^{6}Li content in the screen.

These distributions are representative of the distributions used to sample the neutron capture depth when estimating the attenuation length coefficient.

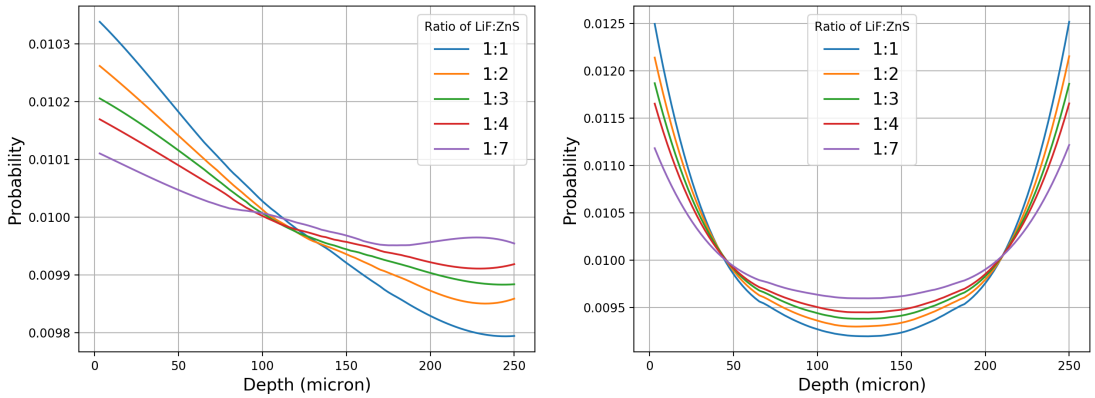

(a) Collimated source (b) Random source

Figure 2.10: The probability density for depth of neutron capture in a ^{6}LiF:ZnS screen predicted using MCNP6 for (a) a collimated source at one side of the screen, and (b) neutrons generated at random locations and angles in the surrounding environment. When the source is collimated at one side of the screen, neutron capture is more probable near that side. As the ^{6}Li content increases, neutron capture becomes more probable near the edges of the screen.

2.1.6 Threshold of Detection

The last factor of neutron detection efficiency is the threshold of detection used by the data acquisition to identify a signal as a neutron. In many detectors, the light emitted by the material must be collected and converted to an electronic signal. It is estimated that tens to hundreds of thousands of photons escape the phosphor screen with every neutron capture but only hundreds of photons reach the photodetectors in SoLid [17]. If the signal created by the incident photons exceeds the threshold for noise, it is then processed by the application-specific trigger algorithms to determine whether the signal is the result of a neutron. In the case of SoLid, the trigger is designed to count the peaks

of the pulse over a rolling window. The combination of light collection efficiency and trigger efficiency is unique to each application.

To mimic the effects of a trigger threshold, a somewhat arbitrary value of 7883 photons was selected as the threshold. This value represents a light yield where only 0.2 MeV of energy is deposited in the ZnS and the attenuation is within the 15th percentile of greatest attenuation. This only represents a small fraction of the total events in each scenario, but impacts the neutron detection efficiency of materials that have a high probability of low energy deposition.

2.2 Validation of the LiF:ZnS Model

A series of studies were conducted to validate the approach of this combined neutron detection efficiency model (with an emphasis on the energy deposition simulations), provide a baseline of performance based on the Scintacor screens to make comparisons, and to study design parameters of ceramics as they relate to detection efficiency enabling optimization of these parameters. Figure 2.11 provides a schematic of the multiple studies conducted in this effort categorized into one of these three areas.

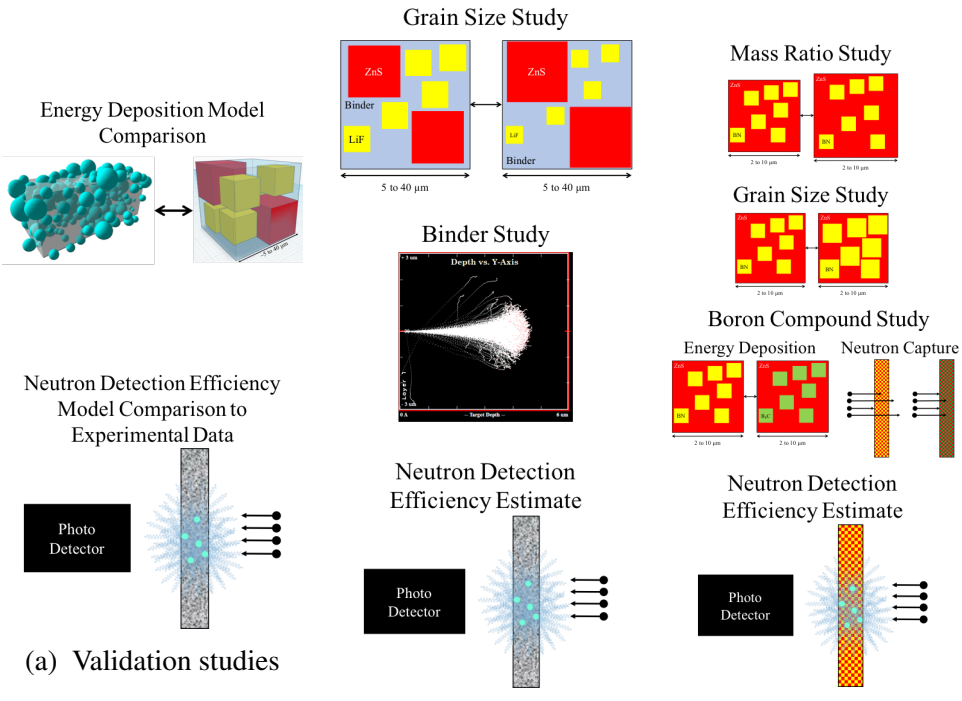

(a) Validation studies

(b) Scintacor screen studies

(c) Ceramic studies

Figure 2.11: Schematic of modeling and simulation studies to predict neutron detection efficiency of ceramic designs to include (a) studies to validate the energy deposition model and neutron detection efficiency model, (b) studies of the Scintacor screen to predict neutron detection efficiency, and (b) studies of ceramic design parameters to achieve optimal neutron detection efficiency and compare to the Scintacor screen.

To assess the validity of the model, the energy deposition simulations were applied to screens studied by Spowart and compared to similar simulations conducted by Herzkamp using GEANT4. This model provides a fitting comparison because of its good validation with experimental data, the format of the model results allows for a straightforward comparison, and the similarities in the models make for an interesting comparison.

Additional validation came by comparing the model to experimental measurements made by Spowart [12]. Spowart measured the optical density (OD) of photographic

films exposed to phosphor screens while the screens were exposed to a controlled dose of 1.5×10^7 thermal neutrons cm^{-2}. Presumably these screens had a controlled thickness, standard binder, and same grain size distributions. Making such a comparison required slightly modifying the model to simulate total photon yield instead of neutron detection efficiency.

2.2.1 Comparison with Herzkamp Microscopic Model

Herzkamp developed a model to simulate the entire process of neutron detection for a spallation neutron experiment detector that uses phosphor screens similar to SoLid. This validation focused on the models of light production in the screens that simulated energy deposition in ZnS from the neutron capture products of ^{6}Li using GEANT4 [55]. The model approximates the phosphor screens as a $100 \times 40 \times 40$ μm box with randomly distributed spheres of ZnS with no overlap (see Figure 2.12). The radii of the ZnS spheres followed a stochastic distribution with a mean value. The intervening material between spheres consisted of a homogeneous mixture of binder and LiF simulating the combined effect of binder and LiF. Charged particles were simulated to originate from a random location within a single grain of ^{6}LiF and then transport through the rest of the box. Energy deposition in the spheres of ZnS was tallied and binned to provide a probability distribution and average value.

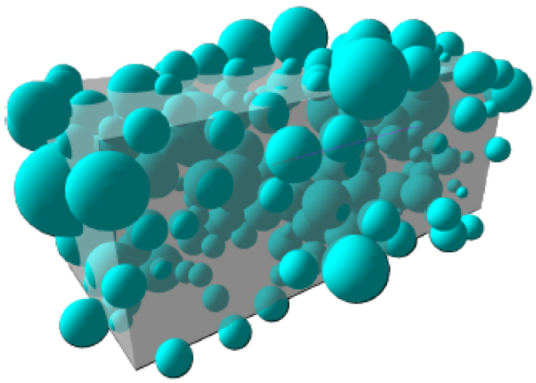

Figure 2.12: Grain box module used in Geant4 simulations to quantify energy transfer to ZnS. Figure reproduced with permission from [55].

In addition to modeling the screens used in the neutron detector, Herzkamp also applied these models to screens studied by Spowart in [11]. These screens had ^{6}LiF:ZnS mass ratios of 6:1, 3:1, 1:2, 1:3, and 1:6. Based on Spowart's suggestion of optimal grain size, Herzkamp assumed a mean size of 10 μm for the ZnS spheres. For the LiF grains, a mean size of 2.5 μm was used based on estimates from other screens. Spowart mentioned optimal LiF grain sizes of 7 μm in [12] which may not have been available to Herzkamp. There is some ambiguity in Herzkamp's simulations as to whether these values represent the sphere diameter, which is more consistent with the definition of grain size reported by Spowart, or as a radius as reported in the summary of simulation parameters.

Herzkamp also made assumptions regarding the binder composition and density. Herzkamp discusses different binders and mentions Lucite (poly methyl methacrylate—PMMA) as the binder with the best optical properties, but does not specify which binder is used in the simulations. Based on neutron attenuation simulations, Herzkamp estimates the binder density would have to be between 0.3 and 0.6 g cm^{-3} to match the experimental data. Because these values are well below common densities of binders,

instead, Herzkamp sets the binder density to 1, consistent with the default value used in his other simulations. The results of the simulations were presented as the mean energy deposited in ZnS and probability distributions for each mass ratio.

For validation, the random-cube model with the MCNP6 simulation was applied to scenarios that mimicked the screens that Herzkamp modeled. The parameters of each MCNP6 scenario are provided in Table 2.1. The density of the binder in these scenarios was set to 1 consistent with parameters used by Herzkamp, but the binder used was representative of polyethylene rather than PMMA.

Table 2.1: Parameters of MCNP6 Simulations for Model Comparison

Screen	Mass Ratio ^{6}LiF:ZnS:Binder	Number of LiF Cubes	Number of ZnS Cubes	LiF Length (μm)	ZnS Length (μm)	Cell Length (μm)
HSpowart61	6 : 1 : 1	596	1	2.5	10	24.3
HSpowart31	3 : 1 : 1	298	1	2.5	10	21.4
HSpowart12	1 : 2 : 1	50	1	2.5	10	15.6
HSpowart13	1 : 3 : 1	33	1	2.5	10	14.2
HSpowart16	1 : 6 : 1	17	1	2.5	10	12.6

The probability distributions and average energy deposition in ZnS for scenarios simulated by Herzkamp and the MCNP6 randomized-cube model show relatively good agreement. The simulated average energy deposited in ZnS from these scenarios is provided in Figure 2.13. The error in the MCNP6 random-cube model is from the statistical variation of the 100 randomized cube arrangements.

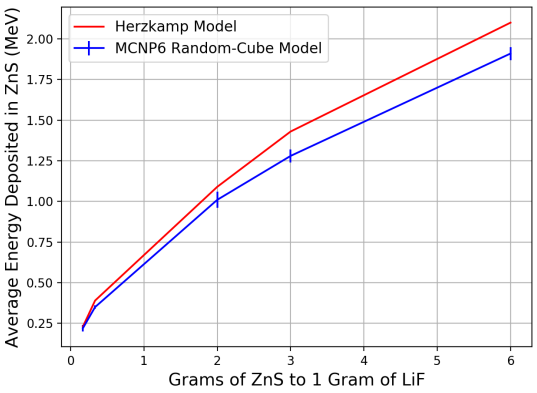

Figure 2.13: The average energy deposited in ZnS for LiF:ZnS screens with varying ratios of LiF as estimated by the Herzkamp microscopic model and MCNP6 Random-Cube model.

While not all values are in statistical agreement, the values are within about 11% and demonstrate the same general trend. Specific differences that are likely to contribute significantly include:

- the shape of the grains (sphere versus cube),
- the reflection at boundaries in the random-cube model,
- the intermediary material is represented as a combination of LiF and binder rather than LiF grains in Herzkamp's model, and
- the differences between GEANT4 and MCNP6.

The shape used to model grains within the material is the most likely reason the random-cube model predicts less energy is deposited in the ZnS than the Herzkamp model. The sphere is an optimized shape and likely represents the best-case scenario, whereas the cube is likely the worst-case scenario.

The simulated probability distributions for energy deposition in ZnS are presented in Figure 2.14. Both simulated probability distributions show trends to higher energies as the ZnS content is increased as expected.

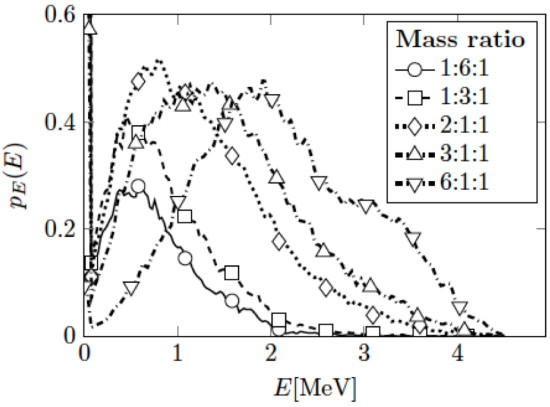

(a) Simulated probability distribution of energy deposited in ZnS for mass ratios studied by Spowart. Figure reproduced with permission from [55].

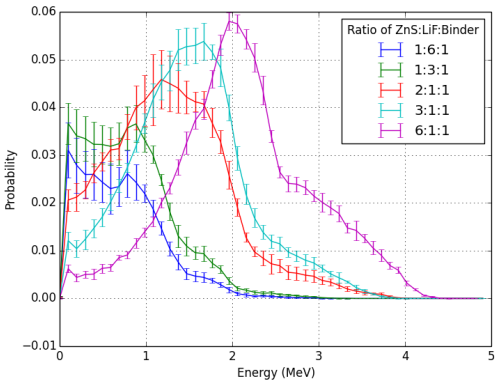

(b) Simulated probability distribution of energy deposited in ZnS for mass ratios studied by Spowart using the randomized-cube model.

Figure 2.14: Probability distributions for simulated energy deposition in ZnS using the (a) Herzkamp grain-box model and (b) the random-cube model. Mass ratios are reported as ZnS:LiF:Binder.

2.2.2 Total Light Yield Comparison with Spowart Data

The model was compared to the Spowart data using (2.1) to sum the number of photons escaping the screen, N_{photons} for each neutron captured, N_{neutrons},

$$N_{\text{photons}} = \sum_{n=1}^{N_{\text{neutrons}}} N_{\text{exit}}. \tag{2.14}$$

This provides a set of values that should be proportional to OD measurements presented by Spowart. The films have an exponential response to increasing photon flux, as reported in [12], but no attempt was made to incorporate this response into the comparison

as the format of the reported values made it difficult to interpret.

The number of neutrons captured was estimated using MCNP6 simulations that modeled a flux of 1.5×10^7 thermal neutrons cm^{-2} on screens with areas of 2.5×2.5 cm^2. The results of the simulations were compared to estimates using (1.6) and presented in Table 2.2. The MCNP6 simulations are consistently higher than the estimates using (1.6), which is likely due to the inclusion of more realistic interactions.

Table 2.2: Results of Neutron Capture Estimates for Spowart Scenarios

Screen	Mass Ratio ^{6}LiF:ZnS:Binder	Estimated ^{6}Li Density (Eqn (1.6))	% of Neutrons Captured (Eqn (1.6))	Estimated ^{6}Li Density (MCNP6)	% of Neutrons Captured (MCNP6)	Neutrons Captured
Spowart61	6 : 1 : 1	3.81×10^{22}	59.2	3.81×10^{22}	60.0(3)	$5.62(3)\times10^8$
Spowart31	3 : 1 : 1	2.79×10^{22}	48.1	2.79×10^{22}	49.0(3)	$4.59(3)\times10^8$
Spowart11	1 : 1 : 1	1.34×10^{22}	27.1	1.35×10^{22}	28.2(5)	$2.64(5)\times10^8$
Spowart12	1 : 2 : 1	1.17×10^{22}	24.1	1.17×10^{22}	25.0(6)	$2.35(5)\times10^8$
Spowart13	1 : 3 : 1	1.04×10^{22}	21.8	1.04×10^{22}	22.5(6)	$2.11(6)\times10^8$
Spowart16	1 : 6 : 1	7.81×10^{21}	16.8	7.81×10^{21}	17.4(7)	$1.63(7)\times10^8$

Energy deposition simulations using the random-cube model were conducted using LiF grain sizes of 7 μm and a binder density of 0.93 that the author thought was more consistent with the screens described by Spowart in [12]. The parameters used in these simulations are provided in Table 2.3 and the results of the energy deposition simulations are presented in Figure 2.15.

Table 2.3: Parameters of MCNP6 Simulations for Spowart Scenarios

Screen	Mass Ratio ^{6}LiF:ZnS:Binder	Number of LiF Cubes	Number of ZnS Cubes	LiF Length (μm)	ZnS Length (μm)	Box Length (μm)
Spowart61	6 : 1 : 1	81	3	7	10	35.3
Spowart31	3 : 1 : 1	68	5	7	10	36.9
Spowart11	1 : 1 : 1	18	4	7	10	30.3
Spowart12	1 : 2 : 1	5	2	7	10	20.1
Spowart13	1 : 3 : 1	5	3	7	10	20.9
Spowart16	1 : 6 : 1	3	4	7	10	20.1

The expected trend of increased energy deposition in ZnS with increased ZnS con-

tent is apparent. The results show what appears to be asymptotically decreasing energy deposition in LiF. This asymptotic minimum is likely related to the energy deposited in the grain where neutron capture occurs and is likely dependent on the grain size. What is more conspicuous in these results is the amount of energy lost to the binder. In many cases, significantly more energy is deposited in the binder rather than the ZnS which contributes to decreased light yield. These results justify re-designing the screens with minimal amounts of binder.

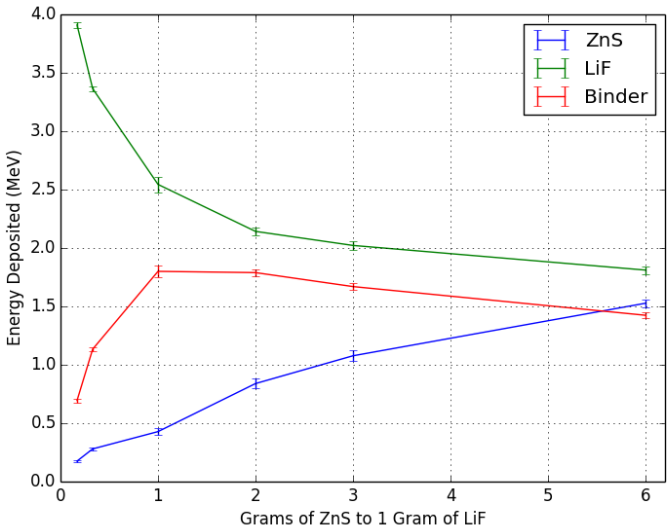

Figure 2.15: Simulated average energy deposition in the various materials in ^{6}LiF:ZnS screens studied by Spowart.

Figure 2.16 shows the results of these same simulations as probability distributions of energy deposition in ZnS. These distributions are broken down by the individual particles and the combination of the two, indicating the triton has the greatest contribution to the light yield.

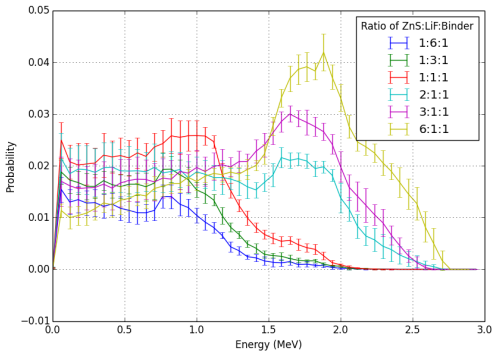

(a) Simulated probability distributions for energy deposited in ZnS from 2.73 MeV triton

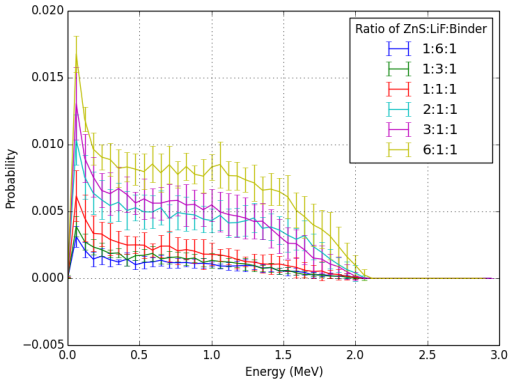

(b) Simulated probability distributions for energy deposited in ZnS from 2.05 MeV α

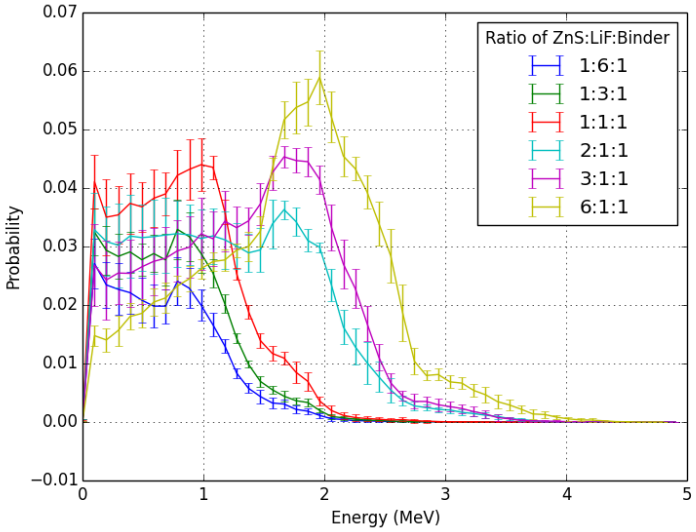

(c) Combined energy deposition in ZnS from the products of neutron capture on ^{6}Li

Figure 2.16: Simulated probability distributions for energy deposited in ZnS from (a) tritons and (b) α produced from neutron capture in ^{6}LiF:ZnS(Ag) for varied mass ratios.

These probability distributions were then used with equation (2.14) to calculate the total number of photons escaping from one side of the screen. The number of neutrons captured, N_{neutrons}, in equation (2.14) was taken from the results presented in Table 2.2.

N_{exit} in equation (2.14) was calculated using equation (2.1), an attenuation length of 410 μm, and a scintillation efficiency of 249 000 photons MeV^{-1} based on estimates made by Herzkamp. These values were used to be consistent with Herkamp's methodology, but both values seem high compared to other reports. Herzkamp measured the attenuation length of modern phosphor screens to be closer to 230 μm. This scintillation efficiency exceeds the theoretical limit for ZnS light yield reported by [50] as mentioned in Section 2.1.4. However, these values only introduce proportional bias in equation (2.14) which can be negated by normalizing the results to unity, as presented in Figure 2.17.

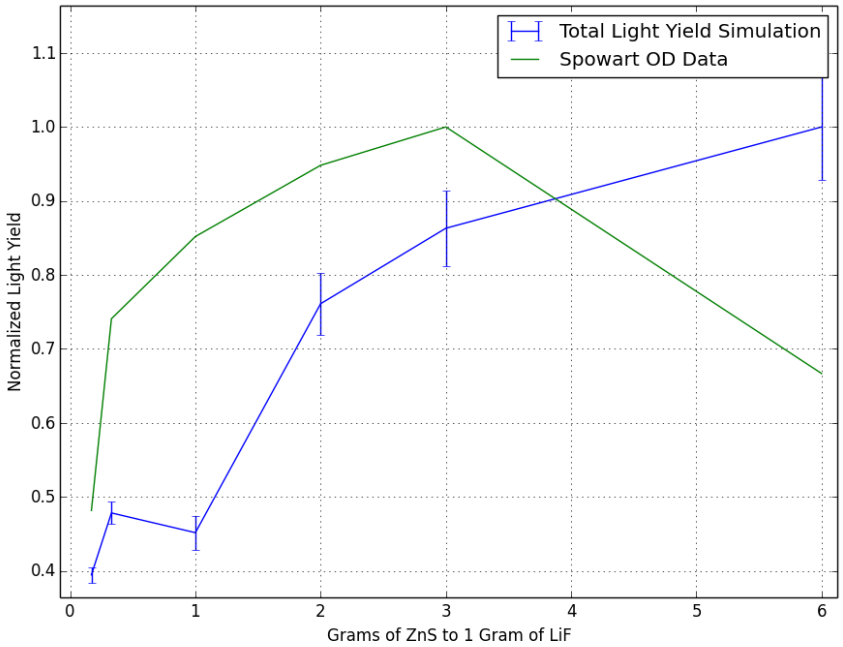

Figure 2.17: Estimated number of photons using the simulated probability distributions for energy transfer.

Comparing these results to the OD data presented by Spowart shows some agreement in the trend of increasing photon production up to a ratio of 1:3:1. However, the

simulation shows a break in the smooth trend of increasing photon production at lower ZnS content (points at the far-left). The break appears to be due to an overestimate of light yield for the 6:1:1 and 3:1:1 (LiF:ZnS:Binder) simulations. This overestimate could be due to an energy threshold effect in the MCNP6 energy deposition simulations. The MCNP6 simulations neglect cumulative energy deposition less than 1 keV resulting in the discontinuity seen in Figure 2.16. This threshold effect becomes problematic for the high LiF content scenarios (i.e. ≥1 gram of LiF to 1 gram of ZnS) where the probability for <1 keV deposition could be relatively high but is not represented, resulting in artificially high number of events with energies >1 keV.

Discrepancies in Model for High ZnS Content Screen

At the other limit of the simulation (to the right of the 1:3:1 ratio), the trend in the model diverges from the trend in the experimental data. The OD data decreases by about 35% between the 1:3:1 and 1:6:1 screens. The initial expectation is that the reduction in total light production is due to a decrease in the number of neutrons captured associated with the higher ZnS content. Based on neutron capture estimates, however, this difference should only be about 5%. The reduction in light, therefore, cannot be solely attributed to the decrease in neutrons captured. Another explanation might be related to saturation of the photographic films used to estimate the photon flux. The increase in ZnS would increase the light yield per neutron captured which may saturate the films and decrease the proportionality of the OD data to photons produced from the screen (a phenomenon not accounted for in the comparison).

Alternatively, the model may be overestimating light production due to a combination of unaccounted changes to attenuation of light and unaccounted phenomenon that reduces energy deposition. The attenuation length is reported to decrease with increased

ZnS content—a phenomenon ignored in this model [12,55]. Most approximations claim the change in attenuation length is at most a factor of 2 which would reduce the attenuation coefficient by at most 10% [55].

Additional reduction in light yield may be due to neglected edge effects in the energy deposition simulation. The max range of the triton is between 30 and 60 μm in the material meaning there is a decent chance the triton terminates its track outside the 250 μm thick material. This phenomenon should have the most impact on simulations that estimate tritons depositing a significant amount of energy in the ZnS near the end of its track, as shown in Figure 2.4. As shown in Figure 2.16a, much of the energy deposited in ZnS in the 1:6:1 scenario is due to a marked increase in tritons depositing energy greater than 1.5 MeV. These high-energy deposition events are likely related to tritons terminating their tracks in ZnS and are therefore more susceptible to edge-effects. Cursory analysis through MCNP6 simulations suggest the losses due to tritons escaping the material may be as high as 11%, which is insufficient to account for the entirety of the light reduction. This suggests the discrepancy between the model and experimental data is likely to be a result of the cumulative effect of multiple factors.

2.3 Scintacor Screen Study

The neutron detection efficiency model was applied to the Scintacor screen using the random-cube MCNP6 simulations to estimate energy deposition. Prior to the detection efficiency estimates, variations of unknown phosphor screen parameters were simulated in the random-cube MCNP6 energy deposition to explore how these parameters might affect the results. The neutron detection efficiency of the Scintacor screen was estimated using the best-case parameters from the energy deposition simulations. This estimate is

used in Section 2.4.2 to compare the results of the neutron detection efficiency model of the hypothetical ceramics to predict performance.

2.3.1 Energy Deposition Simulations

The energy deposition simulations were based on parameters collected from an unpublished report used to predict neutron capture in the SoLid detector. While this report provides information like mass ratios, thicknesses, and binder composition, it does not provide information like grain sizes or the density of each material used. Where information was lacking, parameters were selected based on information from other sources. These unknown parameters reduce the precision of the validity of the energy deposition results. Consequently, additional studies were designed to explore how these parameters might affect the results. The effect of grain size was explored directly through the MCNP6 energy deposition simulations while the effects of binder type and density were explored through SRIM simulations to estimate track depth.

The mass ratio indicated in the report is 1:2:0.83 (LiF:ZnS:binder) with a binder consisting of hydrogen, carbon, oxygen, and silicon in a 6:2:1:1 ratio. The estimated binder density is 0.93 g cm^{-3} based on the known parameters and is within the range for common epoxy densities (0.9 to 1.4 g cm^{-3}). The report provided no information regarding the grain size distribution of the powders or the density of the powders. Based on various reports for other screens, the size of the ZnS particles is estimated to have a mean diameter of 5 μm and the LiF particles are estimated to have a diameter on the order of 2 μm [6, 55]. These values are also consistent with the grain sizes reported for powders from various manufacturers. These manufacturers specifications also report powder densities of 4.09 and 2.635 g cm^{-3} for ZnS and LiF, respectively.

Grain Size

The energy deposition for varying grain sizes in a 1:2 mass ratio (LiF:ZnS) screen was explored by varying ZnS grain sizes between 3 and 10 μm and LiF grain sizes between 1 and 5 μm. The varying grain sizes of each scenario requires complementary variation in the number of cubes in the model and the length of the box to maintain the 1:2 mass ratio. The parameters of each scenario are presented in Table 2.4. It is worth noting that not all combinations of grain sizes could be simulated. This is due to packing factors that limit which combinations are viable without violating the mass ratios or densities.

Table 2.4: Parameters of MCNP6 Simulations for Scintacor Scenarios

Scenario	LiF Length (μm)	ZnS Length (μm)	Number of LiF Cubes	Number of ZnS Cubes	Box Length (μm)
Scint13	1	3	21	1	4.60
Scint15	1	5	97	1	7.66
Scint17	1	7	266	1	10.7
Scint23	2	3	16	6	8.37
Scint25	2	5	12	1	7.66
Scint27	2	7	33	1	10.7
Scint210	2	10	97	1	15.3
Scint33	3	3	9	7	9.57
Scint35	3	5	18	5	13.1
Scint37	3	7	10	1	10.7
Scint310	3	10	29	1	15.3
Scint53	5	3	3	18	12.1
Scint55	5	5	7	9	15.9
Scint510	5	10	19	3	22.1
Scint73	7	3	4	65	18.5
Scint77	7	7	7	9	22.3

The results of the simulations for Scintacor scenarios are presented in Tables 2.5 and 2.6 and Figures 2.18 and 2.19. Most of the energy released from neutron capture is

deposited in the LiF—about half of this energy is attributed to the α. About a third of the energy is deposited in the binder and the remaining 25-30% of the energy is deposited in the ZnS. Most of the variation in energy deposition in ZnS over the range of these scenarios is attributed to the α particle. For a 1:2 mass ratio screen, the triton deposits about a third of its energy equally between the ZnS, LiF, and binder and accounts for nearly two-thirds of the total energy deposited in ZnS, as seen in Tables 2.5 and 2.6. The energy deposited in ZnS by the triton only varies by about 40 keV over the range of grain sizes explored. Greater variation is seen in the energy deposited in ZnS by the α particle as this value spans a range of about 220 keV.

Table 2.5: Average Energy Transferred in Scintacor Study for Increasing ZnS Grain-Size

		Average Energy Deposited (MeV)			
Screen	Material	^{3}H	α	Total	% Total
Scint23	ZnS	0.91 ± 1 %	0.36 ± 10 %	1.27 ± 4 %	27
	LiF	0.94 ± 1 %	1.20 ± 6 %	2.14 ± 4 %	45
	Binder	0.87 ± 1 %	0.49 ± 7 %	1.36 ± 3 %	28
Scint25	ZnS	0.93 ± 1 %	0.40 ± 5 %	1.33 ± 2 %	28
	LiF	0.89 ± 1 %	0.91 ± 3 %	1.80 ± 2 %	38
	Binder	0.91 ± 1 %	0.74 ± 2 %	1.65 ± 1 %	34
Scint27	ZnS	0.92 ± 1 %	0.33 ± 9 %	1.25 ± 3 %	26
	LiF	0.91 ± 1 %	1.04 ± 2 %	1.95 ± 1 %	41
	Binder	0.90 ± 1 %	0.68 ± 4 %	1.58 ± 2 %	33
Scint210	ZnS	0.90 ± 1 %	0.28 ± 16 %	1.17 ± 5 %	25
	LiF	0.92 ± 1 %	1.01 ± 3 %	1.93 ± 2 %	40
	Binder	0.91 ± 1 %	0.76 ± 3 %	1.67 ± 2 %	35

Table 2.6: Average Energy Transferred in Scintacor Study for Increasing LiF Grain-Size

		Average Energy Deposited (MeV)			
Screen	Material	^{3}H	α	Total	% Total
Scint15	ZnS	0.93 ± 1 %	0.48 ± 8 %	1.41 ± 3 %	30
	LiF	0.88 ± 1 %	0.83 ± 3 %	1.71 ± 2 %	36
	Binder	0.91 ± 1 %	0.74 ± 2 %	1.65 ± 1 %	34
Scint25	ZnS	0.93 ± 1 %	0.40 ± 5 %	1.33 ± 2 %	28
	LiF	0.89 ± 1 %	0.91 ± 3 %	1.80 ± 2 %	38
	Binder	0.91 ± 1 %	0.74 ± 2 %	1.65 ± 1 %	34
Scint35	ZnS	0.89 ± 2 %	0.26 ± 15 %	1.15 ± 5 %	24
	LiF	0.95 ± 2 %	1.23 ± 5 %	2.19 ± 3 %	46
	Binder	0.88 ± 1 %	0.56 ± 5 %	1.44 ± 2 %	30
Scint55	ZnS	0.91 ± 1 %	0.32 ± 12 %	1.23 ± 4 %	26
	LiF	0.96 ± 1 %	1.26 ± 4 %	2.21 ± 3 %	46
	Binder	0.86 ± 1 %	0.47 ± 9 %	1.33 ± 4 %	28

The variation in energy deposited in ZnS by the α is related to its much shorter track length (~6 μm in ZnS and LiF based on SRIM simulations—see Table 2.12). Because the α track length is on the order of the length of the grains, changes in grain size cause a significant difference in how much ZnS is encountered along the path of the α. This dependence is most evident in variations of the LiF grain size. For every micron of increase in LiF grain size, the energy deposited in ZnS by the α decreases by about 55 keV, as shown in Figure 2.18a. The dependence of energy deposition in ZnS on LiF grain size is likely attributed specifically to the LiF grain where the α originated. The size of this particular grain dominates the proportion of track that occurs in LiF in total. As shown in Figure 2.18a, the energy deposition in the LiF itself (the green line) appears to approach asymptotic limits at both extremes of LiF grain size. At smaller grain sizes, energy deposition in LiF asymptotically approaches zero and at larger grain sizes it asymptotically approaches some value (likely to be proportional to the surface

area to volume ratio).

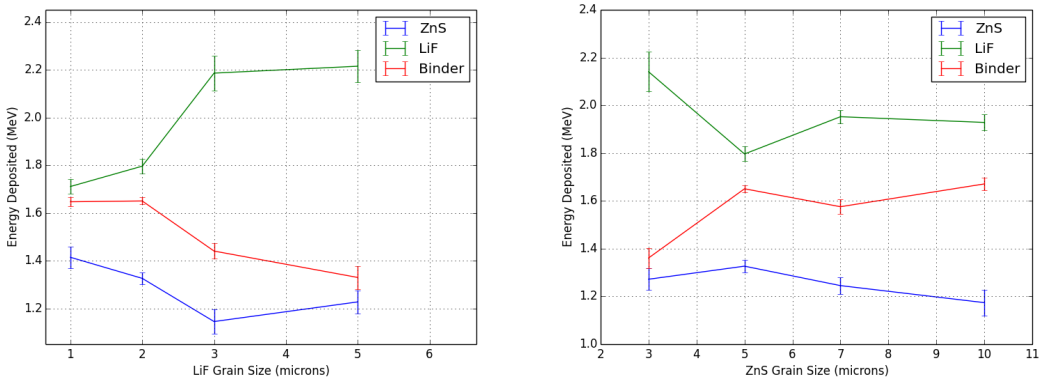

(a) Varying LiF grain size with a fixed ZnS grain size of 5 μm.

(b) Varying ZnS grain sizes with a fixed LiF grain size of 2 μm.

Figure 2.18: Simulated average energy deposition in the various materials in Scintacor screens for varying grain sizes of (a) LiF and (b) ZnS.

Figure 2.18b shows a similar, although less significant, decrease in energy deposition with increasing ZnS grain size. For every micron increase in the ZnS grain, the energy deposited in ZnS decreases by about 17 keV—about a third the rate of the LiF dependence. The slight maximum seen at a ZnS grain size of 5 μm may be correlated to the average range of the α particle in ZnS of about 6 μm (see Table 2.12). If 5 μm were a true optimal grain size, then it does not agree with the 10 μm optimal ZnS grain size presented by Spowart (however, Spowart's conclusion is based on results of experiments with only two ZnS grain sizes—7 and 20 μm [12]).

An interpolation of results of additional combinations of grain sizes is presented in Figure 2.19 to illustrate the general trends of combined changes to both ZnS and LiF grain sizes. These results suggest optimal combinations of grain sizes occur in the regions of 1 μm sized LiF and 5 μm sized ZnS, and 3 μm sized LiF and 3 μm sized ZnS.

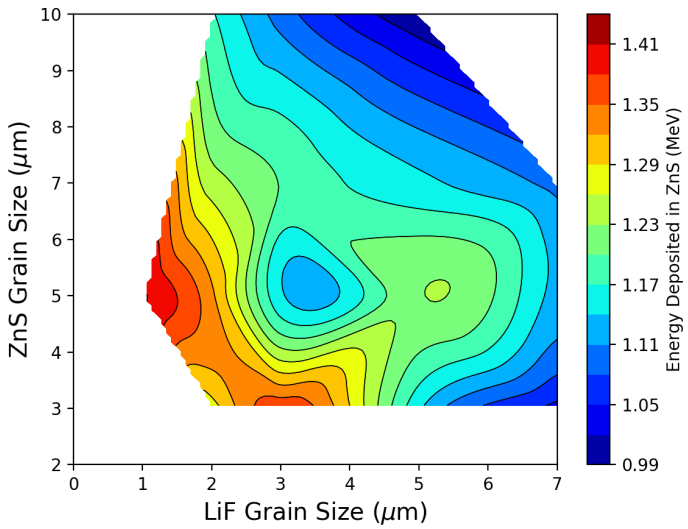

Figure 2.19: Simulated average energy deposition in ZnS for varying grain sizes of LiF and ZnS.

Because the grain sizes in the screen are unknown, the scenario with highest energy deposition in ZnS is used for comparison with the ceramics. This would predict energy deposition in ZnS on the order of 1.41(5) MeV. This value is about 17% higher than Herzkamp's estimates for a modern 1:2 ratio screen [55]. This difference could be attributed to differences in binder and binder density used in the simulations, as discussed in the next section.

Effects of Binder

The 1.41 MeV value is based on a binder density of 0.93 g cm^{-3} using a binder resembling polydimethylsiloxane (C_2H_6OSi), whereas the binder used in the Herzkamp simulations was polyethylene (C_2H_4) and likely used a density of 1 g cm^{-3} (the density could have been as high 1.98 g cm^{-3} in these simulations) [55]. The impact of binder and binder density on energy deposition was indirectly explored using SRIM simula-

tions to estimate particle track length. Figure 2.20 shows the impact different binders and densities have on the range of the triton and α.

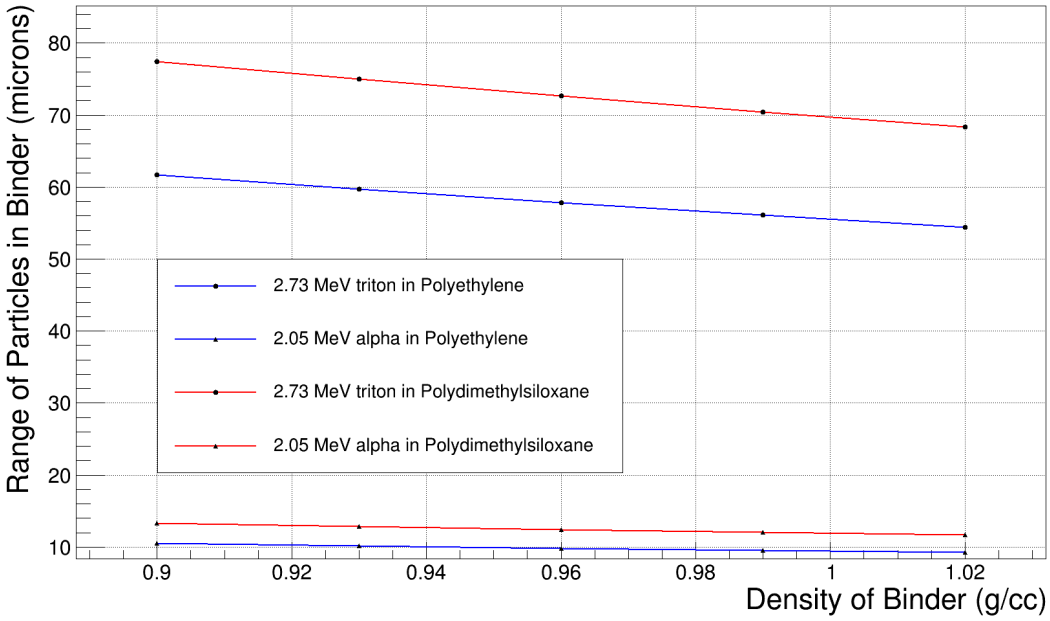

Figure 2.20: Ranges of particles traveling through common binders as a function of binder density.

The figure shows clear differences in track length between the two types of binders and decreasing track length for increasing density. There is about a 33% difference in the range of the α when traveling through polyethylene and polydimethylsiloxane and about a 7% decrease in the α range when increasing the density from 0.9 to 1.02 g cm^{-3}. The triton experiences about 23% difference in track length between polyethylene and polydimethylsiloxane and the 7% decrease in track length with increasing density. Based on these results, it is apparent the combination of different binders and higher densities in the Herzkamp simulations is the likely source of the difference in the energy deposition estimates.

Clearly the polydimethylsiloxane binder with minimal density represents the best-

case scenario for energy transfer in the phosphor screens. The energy deposition simulations assumed a binder density of 0.93 g cm^{-3}. A potentially more accurate density of polydimethylsiloxane is 0.965 g cm^{-3} rather than 0.93 g cm^{-3}. Using this density would decrease the range of both the triton and α by about 3% and would result in a correlated decrease in energy deposited in ZnS. Therefore, the binder and binder density used in the energy deposition simulations represent the best-case scenario for energy transfer to ZnS.

This best-case 1.41 MeV value is 39% below the 2.31 MeV of energy released in neutron capture on ^{10}B. Therefore, a boron and ZnS based material that achieves greater than 60% energy deposition in ZnS should produce a similar light yield to the Scintacor screen.

2.3.2 Estimation of Neutron Detection Efficiency

With the microscopic interactions accounted for, the next step is to estimate the macroscopic neutron detection efficiency. The probability of neutron capture was estimated using both the MCNP6 simulations and the mathematical model (equation (1.6)). The probability of detection given a neutron capture occurred was estimated using the energy deposition distribution for the Scint15 (1:2 LiF:ZnS mass ratio, 1 μm LiF grain and 5 μm ZnS grain) scenario, the mathematical model for conical light attenuation, and threshold for detection. As described above, these two probabilities combine to give neutron detection efficiency.

Neutron capture was based on the following assumptions:

- a neutron flux of 1.5×10^{7} n cm^{-2},
- a screen area of 2.5×2.5 cm^{2},

- a screen thickness of 250 μm, and
- a thermal neutron source to one side of the screen.

The estimated number of neutrons captured by the Scintacor screen is presented in Table 2.7.

Table 2.7: Results of Neutron Capture Estimates for Scintacor Screen

Screen	Mass Ratio ^{6}LiF:ZnS:Binder	Estimated ^{6}Li Density (Eqn (1.6))	% of Neutrons Captured (Eqn (1.6))	% of Neutrons Captured (MCNP6)	Neutrons Captured
Scintacor	1 : 2 : 0.83	1.30×10^{22}	26.3	27.0(5)	$2.53(5)\times10^{8}$

For each neutron captured, an energy deposition was sampled from the distribution shown in Figure 2.21 and a depth of capture was sampled from the exponential distribution described by the attenuation law. The depth of the event was used to estimate the attenuation coefficient. Using this method, the light yield measured at one side of the screen was measured event by event. If the light yield exceeded the arbitrary threshold of 7883 photons (as discussed in Section 2.1.6), the event was counted as detected. These calculations resulted in a neutron detection efficiency of 24% with an average light yield of 5.73×10^{4} photons per neutron detected.

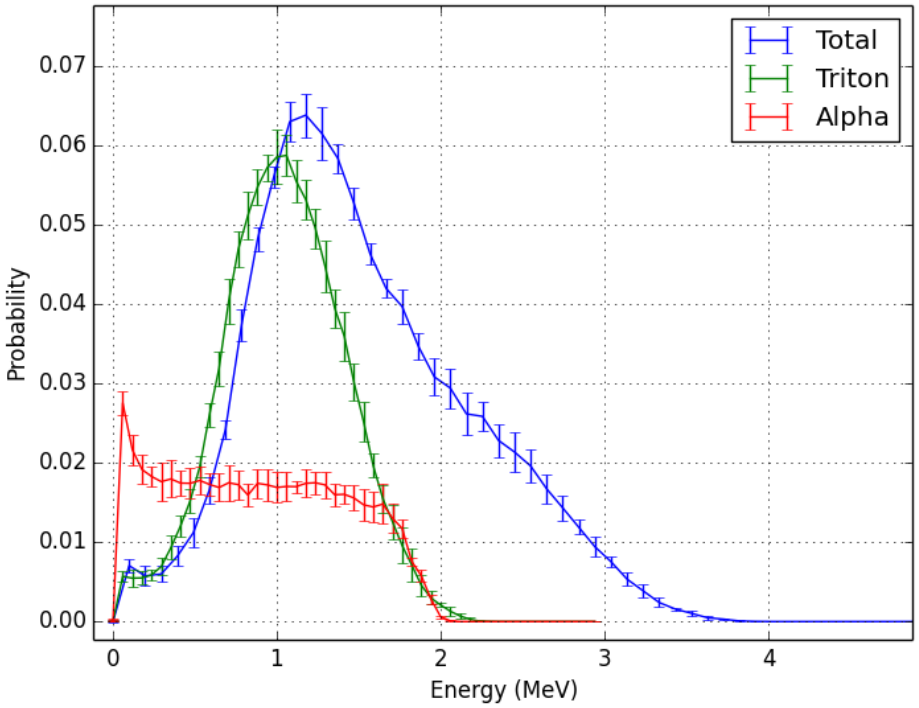

Figure 2.21: Simulated probability distribution for energy deposited in ZnS for the Scint15 scenario.

2.4 Ceramics Study

With a baseline of neutron detection efficiency established for the Scintacor screen, the next step in the effort is to estimate ceramic designs that have detection efficiency exceeding the baseline. Instead of accurately trying to estimate the neutron detection efficiency of a known material (as was the case in the Scintacor screen study), this study estimated detection efficiency of hypothetical ceramics using parameters that could feasibly be used to fabricate a real ceramic. These parameters include mass ratios, grain sizes, enrichment, and various boron compounds. The grain size was limited to micron-

sized particles as this represents commercially-available grain sizes. The density of each compound was based on manufacturer specifications for commercially-available powders. Enrichment has no effect on the energy deposition simulations, but does benefit neutron capture and was included in the estimates of neutron capture and neutron detection efficiency. The primary compound used for comparison is boron nitride (BN) as it showed favorable sintering properties with ZnS. Additional simulations with other boron compounds (boron, boron carbide, and boron oxide) were conducted to explore differences between the particles.

2.4.1 Energy Deposition Simulations

Results of energy deposition simulations provide insight into the combinations of mass ratios and grain sizes that provide comparable energy transfer to the Scintacor screen. Additional simulations explored the impact of exchanging the boron nitride for a different compound.

Mass Ratios

The mass ratio of BN to ZnS was controlled by increasing the dimensions of the outer box. In every scenario, the BN cube had dimensions of $1 \times 1 \times 0.5$ μm. In all but three simulations, the number of BN cubes was 12. For the simulations with mass ratios of 1:2, 1:3, and 1:6, the number of cubes was reduced to 8 to satisfy packing factors. Because the energy transfer results from those three scenarios with 8 cubes appear to overestimate the energy deposition, additional simulations were conducted for a 1:20 mass ratio to explore how the number of cubes affect the results. Table 2.8 provides the parameters used in the MCNP6 simulations for this series of scenarios.

Table 2.8: Parameters of MCNP6 Simulations for Ceramic Scenarios of Variable Mass Ratios

Scenario	Mass Ratio Boron:ZnS	Cube Area (μm^2)	Cube Width (μm)	Number of Cubes	Cube Density (g cm^{-3})	Cell Length (μm)
BN12	1 : 2	1	0.5	8	2.29	2.04
BN13	1 : 3	1	0.5	8	2.29	2.20
BN16	1 : 6	1	0.5	8	2.29	2.59
BN110	1 : 10	1	0.5	12	2.29	3.41
BN115	1 : 15	1	0.5	12	2.29	3.83
BN120	1 : 20	1	0.5	12	2.29	4.18
BN130	1 : 30	1	0.5	12	2.29	4.74
BN150	1 : 50	1	0.5	12	2.29	5.58
BN180	1 : 80	1	0.5	12	2.29	6.50

The results of these simulations (see Figure 2.22), indicate ceramics with mass ratios of 1:6 or higher exceed the 1.41 MeV average energy deposition of the Scintacor screen. As the ZnS content increases, the energy deposition approaches an asymptotic limit like the trends seen in the Spowart study. Ratios above 1:30 appear to offer minimal improvement in energy transfer and therefore might be considered an upper limit.

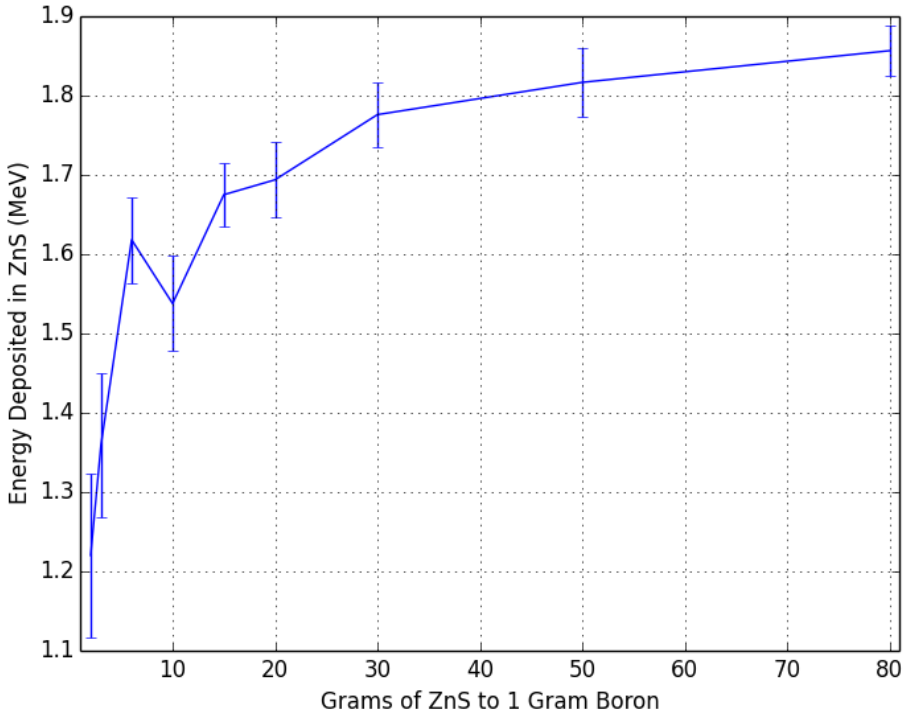

Figure 2.22: Simulated average energy deposition in ZnS for varying ratios of BN:ZnS. The size of the BN grain is 1 μm.

There is a small break in the otherwise smooth data seen between the 1:6 and 1:10 mass ratios presented in Figure 2.22. While this break could be of no significance, there was concern it was an artifact associated with changing the number of cubes in the model from 8 to 12 (see Table 2.8). To confirm the number of cubes has no impact on the results, additional simulations with different number of cubes were conducted for the 1:20 ratio scenario. The results of these simulations are presented in Figure 2.23 and show no underlying dependence on the number of cubes.

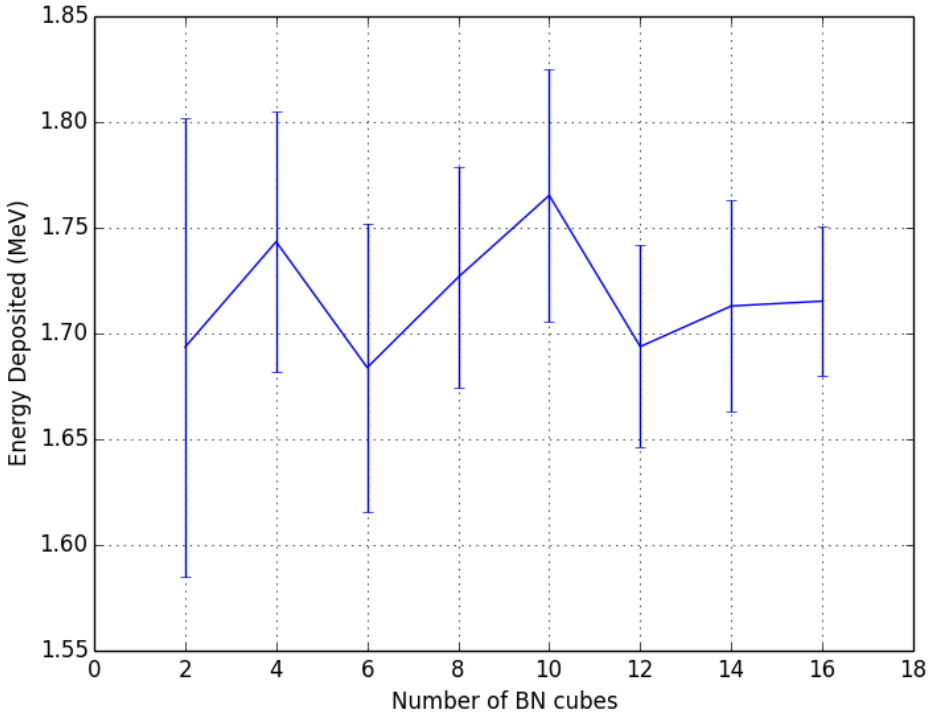

Figure 2.23: Simulated average energy deposition for BN120 scenarios using varied numbers of cubes.

Energy deposition distributions for individual particles with changing mass ratios are presented in Figure 2.24. One of the main results when considering the approach of a composite ceramic is that each particle deposits a significant portion of its energy in ZnS due to the absence of the binder in contrast to ~30% of energy lost to the binder in the phosphor screens. At high ratios, energy deposition approaches the maximum limit for each particle. A small probability exists that energy deposition in ZnS exceeds the nominal 2.31 MeV released in the charged particles from ^{10}B capture. This is due to the absence of the gamma in 6% of events resulting in 2.79 MeV of energy released via the charged particles (see equation (1.8)).

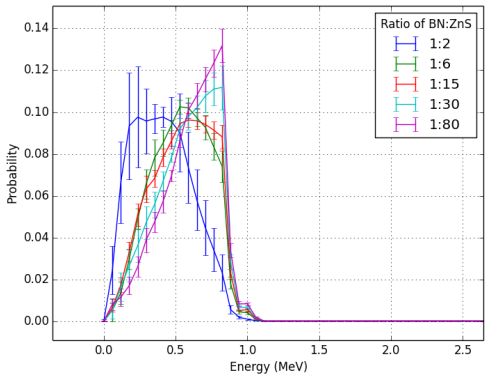

(a) Simulated probability distributions for energy deposited in ZnS from ^{7}Li particles produced from capture on ^{10}B.

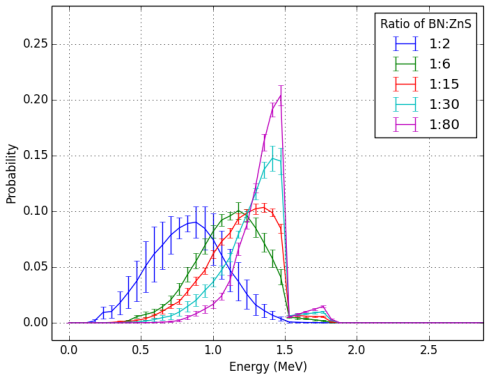

(b) Simulated probability distributions for energy deposited in ZnS from α particles produced from capture on ^{10}B.

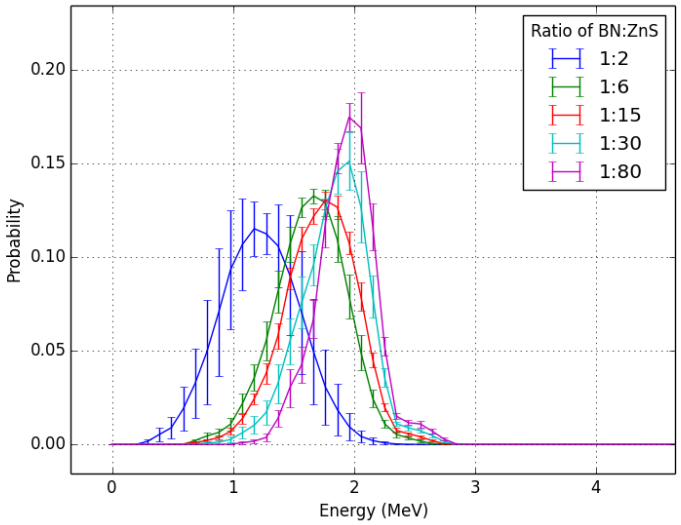

(c) Combined energy deposition in ZnS from the products of neutron capture on ^{10}B for ceramics with varying ratios of BN:ZnS.

Figure 2.24: Simulated probability distributions for energy deposited in ZnS from (a) ^{7}Li and (b) α as a result of neutron capture in BN:ZnS(Ag) ceramic with varied mass ratios.

Grain Size

The second series of simulations explored changing the length of the BN cubes while maintaining the width at 500 nm. The lengths explored include 500 nm, 1, 2, 4 and 6 μm for a constant mass ratio of 1:20 BN to ZnS. The simulations for a 4 and 6 μm BN cube required reducing the number of cubes from 12 to 8. The expected overestimate of energy deposition in ZnS in these scenarios is not as apparent as previously seen with the scenarios with low mass ratios. The parameters used in the MCNP6 simulations for this series of scenarios is provided in Table 2.9 and the results are provided in Figure 2.25. These results demonstrate the same trend of increased energy deposition in ZnS with decreased grain size.

Table 2.9: Parameters of MCNP6 Simulations for Ceramic Scenarios of Variable Grain Size, Assuming a BN Density of 2.29 g cm^{-3}

Scenario	Mass Ratio Boron:ZnS	Cube Area (μm^2)	Cube Width (μm)	Number of Cubes	Cell Length (μm)
BN120A	1 : 20	0.25	0.5	12	2.64
BN120	1 : 20	1	0.5	12	4.18
BN120B	1 : 20	4	0.5	12	6.64
BN120C	1 : 20	16	0.5	8	9.21
BN120D	1 : 20	64	0.5	8	12.07

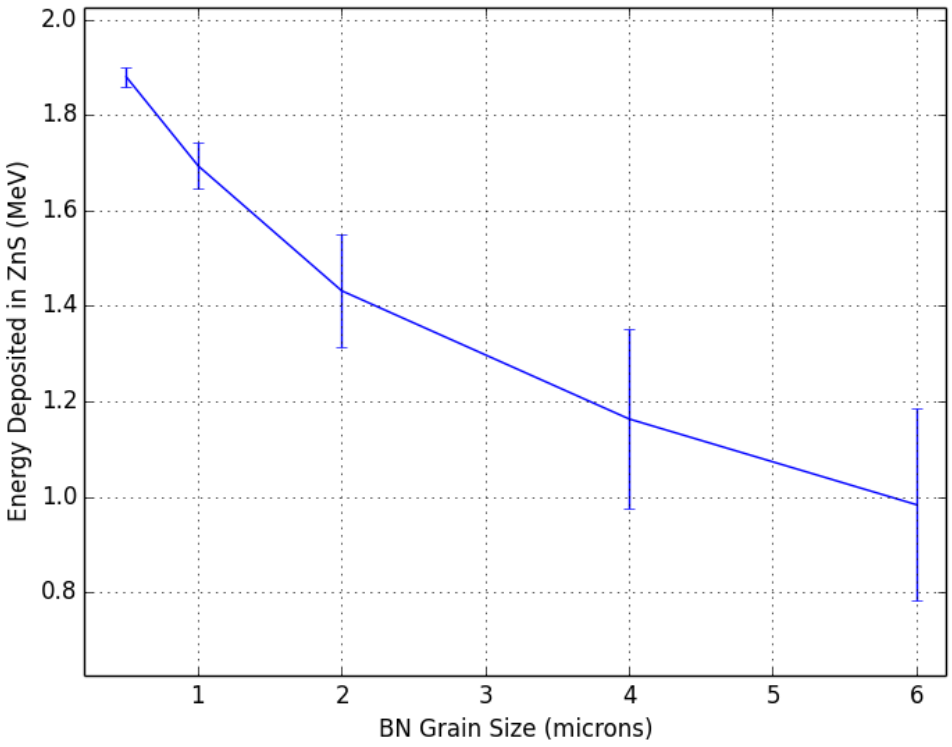

Figure 2.25: Simulated average energy deposition in ZnS for varying grain sizes of BN. The ratio of BN:ZnS is held at 1:20.

Boron Compound

The last series of simulations substituted the boron nitride for boron, boron carbide, and boron oxide at a mass ratio of 1:20. In these simulations, cubes of $1 \times 1 \times 1$ μm dimensions were used for these compounds as the shape is expected to be more cubic than graphite-like. Table 2.10 provides the parameters used in the MCNP6 simulations for this series of scenarios.

Table 2.10: Parameters of MCNP6 Simulations for Ceramic Scenarios of Variable Boron Compound

Scenario	Mass Ratio Boron:ZnS	Cube Area (μm^2)	Cube Width (μm)	Number of Cubes	Cube Density (g cm^{-3})	Cell Length (μm)
BN120	1 : 20	1	0.5	12	2.29	4.18
B120	1 : 20	1	1	12	2.35	5.31
BC120	1 : 20	1	1	12	2.51	5.42
BO120	1 : 20	1	1	12	2.46	5.39

The results presented in Table 2.11 show only slight differences in energy transferred from compound to compound. The differences shown in the results of the energy deposition simulations might be explained by looking at the range of particles due to different specific energy loss. SRIM simulations for the α and ^{7}Li through the various compounds, as shown in Table 2.12, show comparable ranges indicating the specific energy loss is less of a factor. Simulations of ranges of tritons and α through materials in the screen are also included for comparison.

Table 2.11: Average Energy Transferred for Varying Boron Compound Ceramics

		Average Energy Deposited (MeV)			
Scenario	Material	^{7}Li	α	Total	% Total
B120	ZnS	0.45	1.16	1.61	69
	BN	0.4	0.32	0.72	31
BN120	ZnS	0.51	1.19	1.69	73
	BN	0.34	0.3	0.64	27
BC120	ZnS	0.44	1.16	1.6	69
	BN	0.4	0.32	0.73	31
BO120	ZnS	0.48	1.19	1.67	72
	BN	0.36	0.29	0.66	28

Statistical error is within 5% of the values presented

Table 2.12: Summary of Particle Ranges in Relevant Materials from SRIM Simulations

		^{3}H	α			^{7}Li	
	Energy (MeV):	2.73	1.47	1.78	2.05	0.84	1.01
Material	Density ($\frac{g}{cm^3}$)	Ranges (μm)					
ZnS	4.09	31.78	4.27	5.16	5.95	2.36	2.54
Binder	0.93	72.24	8.76	10.67	12.39	4.62	4.96
LiF	2.635	33.49			6.05		
B	2.35		3.61	4.38		1.91	2.06
BN	2.29		3.97	4.77		2.24	2.41
B_4C	2.51		3.43	4.14		1.78	1.91
B_2O_3	2.46		4.06	4.84		2.30	2.46
$B(OH)_3$	1.435		6.29	7.50		3.64	3.90

2.4.2 Neutron Detection Efficiency

From the results in the previous section, it is apparent that the maximum energy transfer occurs at mass ratios with high ZnS content. Using such high mass ratios, however, will reduce the neutron capture of the ceramic. To optimize neutron detection efficiency between these two competing factors, neutron capture was simulated for ceramics of varying mass ratios and various compounds to illustrate how these compounds and ratios affect neutron detection efficiency. Results of select scenarios that indicate greater neutron capture than the Scintacor screens were used in combination with the corresponding energy deposition distribution to calculate neutron detection efficiency. The probability of capture for 250 μm ceramics with enriched boron compounds of varying mass ratios is shown in Figure 2.26. The difference shown between the various boron compounds is due to the neutron attenuation length from the different isotopic densities resulting from molar ratios and molecular density.

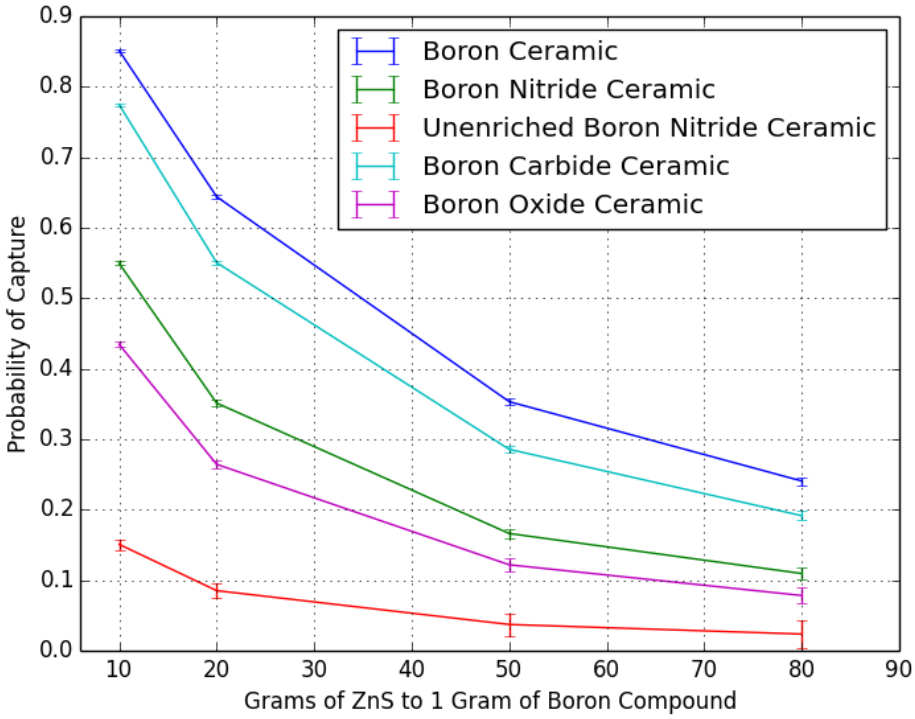

Figure 2.26: Probability of capture for a 250 μm thick ceramic with varying amounts of ZnS.

Table 2.13: Results of Neutron Capture Estimates for Various Ceramics

Compound	Mass Ratio Compound:ZnS	Estimated ^{10}B Density (Model)	% of Neutrons Captured (Eqn (1.6))	Estimated ^{10}B Density (MCNP6)	% of Neutrons Captured (MCNP6)	Neutrons Captured
^{10}BN	1 : 10	8.25×10^{21}	54.7	8.25×10^{21}	55.0(3)	$5.16(2)\times10^{8}$
^{10}BN	1 : 20	4.46×10^{21}	34.8	4.46×10^{21}	35.1(4)	$3.29(4)\times10^{8}$
^{10}BN	1 : 80	1.19×10^{21}	10.8	1.19×10^{21}	11.0(9)	$1.03(9)\times10^{8}$
BN	1 : 20	9.39×10^{20}	8.6	9.11×10^{20}	9(1)	$8(1)\times10^{7}$
BN	1 : 80	2.50×10^{20}	2.4	2.43×10^{20}	2(2)	$2(2)\times10^{7}$
^{10}B	1 : 20	1.07×10^{22}	64.2	1.07×10^{22}	64.4(2)	$6.04(2)\times10^{8}$

Table 2.13 show the neutron capture for select scenarios. The respective energy distributions associated with these scenarios are combined with the results of the neutron capture estimates to calculate neutron detection efficiency.

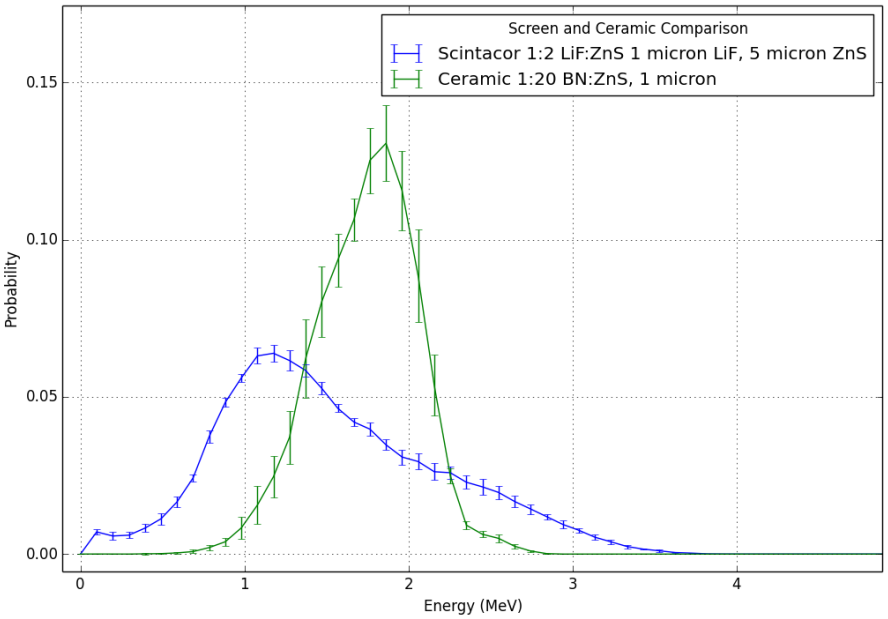

Figure 2.27: Simulated probability distribution for energy deposited in ZnS for the Scint15 scenario and the BN120 scenario.

There is a stark contrast when comparing the energy distributions for the Scint15 scenario and the BN120 scenarios (see Figure 2.27) which are likely to influence the resultant light yield. Based on these distributions, the Scintacor samples are expected to have events with higher maximum light yield than the ceramics, however, the ceramics are expected to have a higher most probable light yield. Furthermore, there is expected to be less variation in the ceramic light yield.

The results of neutron detection efficiency calculations using the energy distribution functions for select ceramics and the Scintacor screen are presented in Table 2.14. From these results, there is a distinct advantage of using a ceramic with a ratio between 1:10 and 1:20 over the Scintacor screens. These ceramics offer increased neutron capture and comparable photon yield per neutron detected. Although the threshold is arbitrary, this

example illustrates the effects of the energy distribution on identification efficiency as the Scintacor scenario loses 2% of the neutrons to low light yield. Because the distributions for the ceramics are more uniform, the effect of the threshold is less pronounced. The advantage of using pure boron over boron nitride is also clear.

Table 2.14: Neutron Detection Efficiency Comparison

Scenario	Neutrons Captured (% Dose)	Photons Escaped	$\frac{\text{Photons}}{\text{Neutron Captured}}$	Neutron Detected (% Dose)	$\frac{\text{Photons}}{\text{Neutrons Detected}}$
Scint15	2.46×10^{7} (26%)	1.30×10^{12}	5.29×10^{4}	2.27×10^{7} (24%)	5.73×10^{4}
^{10}BN110	5.13×10^{7} (55%)	2.88×10^{12}	5.61×10^{4}	5.12×10^{7} (55%)	5.62×10^{4}
^{10}BN120	3.27×10^{7} (35%)	2.04×10^{12}	6.26×10^{4}	3.26×10^{7} (35%)	6.27×10^{4}
^{10}BN180	1.01×10^{7} (11%)	8.54×10^{11}	8.44×10^{4}	1.00×10^{7} (11%)	8.50×10^{4}
BN120	8.08×10^{6} (9%)	6.59×10^{11}	8.15×10^{4}	8.07×10^{6} (9%)	8.16×10^{4}
BN180	2.23×10^{6} (2%)	2.44×10^{11}	1.10×10^{5}	2.21×10^{6} (2%)	1.10×10^{5}
^{10}B120	6.02×10^{7} (64%)	3.45×10^{12}	5.74×10^{4}	6.01×10^{7} (64%)	5.74×10^{4}

Ceramics of unenriched BN were also included in these calculations. As expected, the neutron detection efficiency is significantly lower from the corresponding ceramics with enriched BN. The unexpected increase in light yield per neutron detected in the unenriched scenarios is presumably due to the capture depth distribution. Neutrons are captured closer to the edge of enriched ceramics whereas neutron capture in unenriched ceramics occurs at more evenly dispersed depths. Light emitted from neutron capture events at the far side in the enriched ceramics consequently experiences greater average attenuation.

2.5 Summary

Based on these simulations, a ceramic made of a boron compound and ZnS is a promising alternative to current ^{6}LiF:ZnS phosphor screens. Although ^{6}Li releases 4.78 MeV of energy per neutron captured, it is estimated that on average only 1.41 MeV is transferred to ZnS producing scintillated light. This value would be improved by reducing the grain size of LiF, reducing the density of the binder, changing the binder, or reducing the amount of binder. Combining powders through sintering altogether alleviates the need for a binder allowing for more efficient energy transfer. Using ^{10}B, rather than ^{6}Li, with ZnS in such a ceramic has potential for higher neutron detection efficiency due to its higher cross-section and higher energy transfer efficiency to ZnS. This claim is predicated on the assumption that the optical attenuation length of the ceramic is similar to or greater than the phosphor screens and the sintering process does not affect the scintillation efficiency of ZnS. Under these assumptions, a ceramic fabricated of enriched BN and ZnS with mass ratios between 1:10 and 1:20 is estimated to detect between 11 to 31% more neutrons with an average light yield that is within 2% of the Scintacor screen. If the ceramic were fabricated using pure boron (or boron carbide), the neutron detection efficiency would increase from 24% to 64% with comparable light yield—closer to the target efficiency required by SoLid.

Chapter 3

Fabrication and Characterization of Composite Ceramics

Because of its luminescent properties, ZnS has been incorporated with neutron-sensitive materials to form neutron detectors. An alternate method to fabricate these neutron-detecting materials is to sinter the ZnS and neutron sensitive material to form a luminescent ceramic. This method is a cost-effective means of producing a neutron-detecting material and is easily scalable to commercial manufacturing.

3.1 ZnS Ceramics

Ceramics are inorganic solids arranged in a polycrystalline structure. One method of forming ceramics is to apply heat and pressure to solid materials. This process is known as sintering and results in densification as voids migrate out of the material with the potential growth of grains to fill the vacancy left by the voids. There is a rich history of research focused on sintering ZnS with a variety of techniques.

3.1.1 Sintering of ZnS

ZnS has been sintered through a variety of techniques. In the 1970's ZnS was sintered through hot-isostatic pressing (HIP) of ZnS grown from chemical vapor deposition (CVD). Densification occurs in HIP by applying pressure and heat to the green-body through the surrounding gas. Typically, these gases are inert and heated through convection. This process was applied to ZnS in the 1970s to develop IR windows for military applications [73] and are now available commercially (see Cleartran^{TM}). Not only are these ceramics highly transparent, they've also demonstrated luminescence [60, 74].

Another form of sintering applies uniaxial pressure to powders loaded in a die. These powders can range from large solids to micron-sized commercial powders or to laboratory-synthesized nanoparticles. Heating of these powders in a uniaxial press can either occur through convection (hot uniaxial pressing—HUP) or joule heating (spark plasma sintering—SPS; or field assisted sintering technique—FAST). These processes offer a simpler and cheaper way to fabricate luminescent ceramics than CVD/HIP [56,59,75]; however, no uniaxial pressed ceramic in the literature reviewed had near the transparency of the CVD/HIP ceramics.

Ceramic neutron detectors must combine neutron-sensitive material with ZnS, maintain the luminescence of ZnS, and provide adequate transparency to allow for light to escape the material. Of the techniques described above, uniaxial press provides the cheapest and simplest means of incorporating neutron-sensitive material into the process. Ceramics of LiF and ZnS have been formed through this process; although these ceramics performed poorly in detection efficiency measurements [76]. It is unknown whether any boron products have been sintered with ZnS via uniaxial press, although many efforts have combined boron compounds with ZnS whether in glasses or as phos-

phor screens [13, 47, 77–79]. Luminescent ceramics have been produced via all processes; however, the greatest transparency is achieved through the CVD/HIP method. Unfortunately, CVD is a time-consuming process and would require development of new deposition chemistry to incorporate boron (or dope the boron in after the fact). This effort focuses on demonstrating the concept feasibility through sintering ZnS with hexagonal boron nitride (BN) via FAST. Hexagonal BN was selected as it is cheap and is will not undergo any transitions under 1600°C and pressures less than a few GPa [80]—making it a favorable candidate for sintering with ZnS.

3.1.2 Field Assisted Sintering Technique

FAST was selected as the sintering method largely due to machine accessibility and the prospect that this technique provides faster densification than conventional HUP. FAST manufacturers also claim the joule heating used in FAST removes voids with less grain growth and in less time than conventional heating methods [81]. This claim is founded in the theory of heat transfer through joule heating.

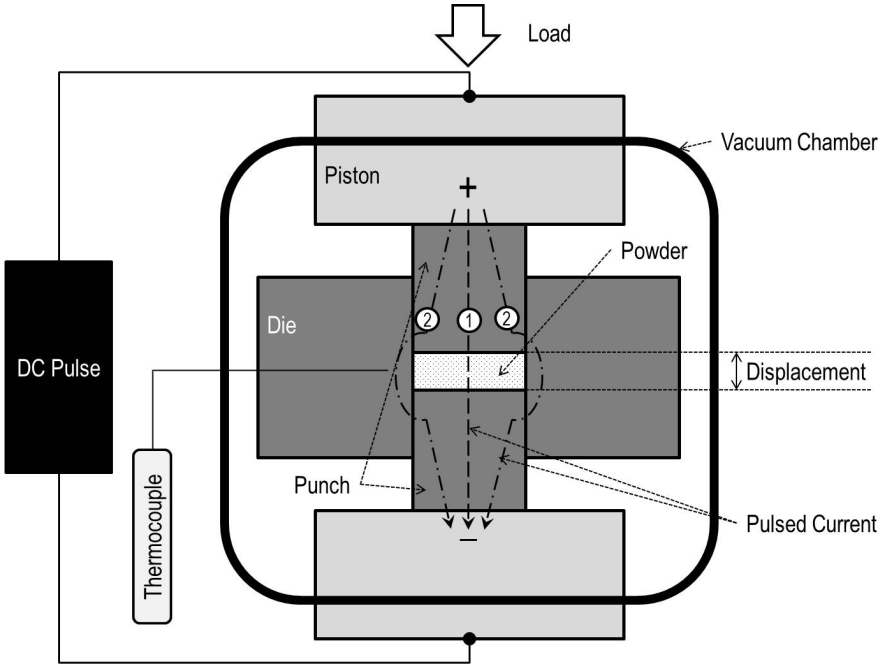

Figure 3.1: Schematic of Field Assisted Sintering Technique. Pulsed current flows from the anode pad to the cathode pad. If the powder is conductive, the current will flow through the powder as shown in path 1 and joule heating occurs. If the powder is not conductive, the current will flow through the die (as shown in path 2) and the powder will be heated via conductive heating from the die.

In FAST, a mechanical load is applied to a punch that transfers pressure to the green body within the die. Low-voltage (up to 10V) DC pulses are applied to the piston plates in contact with the graphite punches. Current flows through the punches and will either flow through the die or through the green body based on differences in resistance, as shown in Figure 3.1. Current passing through the powder (as high as 1 to 10 kA) is theorized to pass along grain boundaries creating localized heat. The high heating rates (up to 1000°C min^{-1}) and high percentage of energy focused along the boundaries provides energy to overcome potential barriers resulting in void migration with minimal grain growth as illustrated in Figure 3.2 [82]. This contrasts with HUP where heat is passed from the environment to the die and then from the die to the powders via ther-

mal conduction (collisions). Energy from these collisions is stored in lattice vibrations within the grains. With more internal energy, the grains are more likely to combine into larger, more energetically-favorable grains. Therefore, the expectation is FAST sintered ceramics will result in smaller grains and achieve densification faster than HUP sintered ceramics.

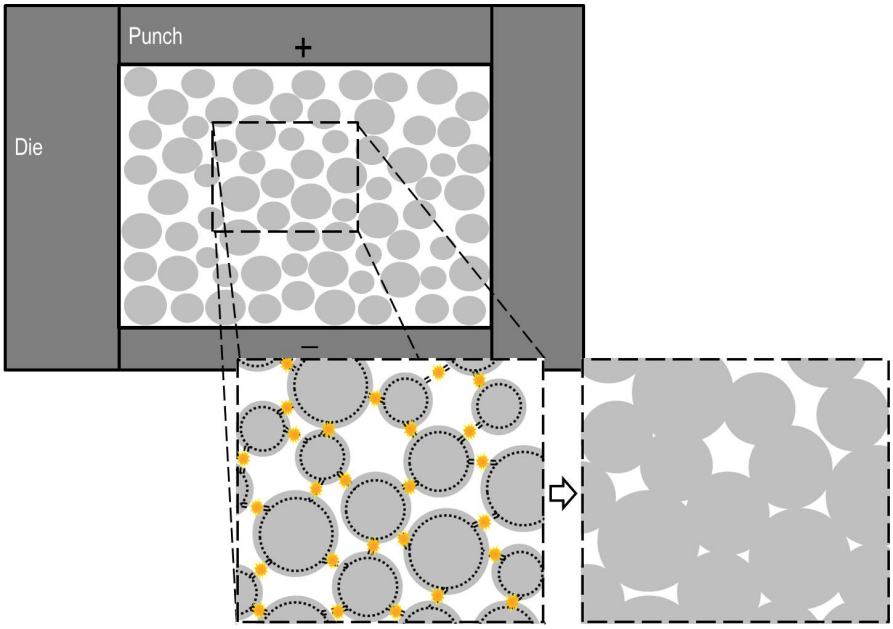

Figure 3.2: Schematic of the results of joule heating from FAST sintering. Current flows around the boundary of the grain and transfers to neighboring grains. This results in less grain growth and more efficient migration of voids.

3.1.3 ZnS Phase Changes

The process of applying heat and pressure results in densification of ZnS, but can also result in undesired phase changes that can degrade transparency and alter the luminescent properties. At about 1020°C, ZnS transitions from its typical sphalerite structure to a wurtzite structure [83] and at 1185°C ZnS melts. Phase transitions have been known to occur at lower temperatures when sintering smaller sized particles [59, 84].

The transition from sphalerite to wurtzite occurs as the orientation of the tetragonal molecular bonds are rotated. At low temperatures, the energetically favored structure is sphalerite (or zinc-blende) which is a cubic closed-packed structure (or face-centered cubic—FCC) of the anions. At higher temperatures, the tetragonal bond rotates resulting in the anions forming a hexagonal closed-pack (HCP) lattice which is the wurtzite structure (see Figure 3.3).

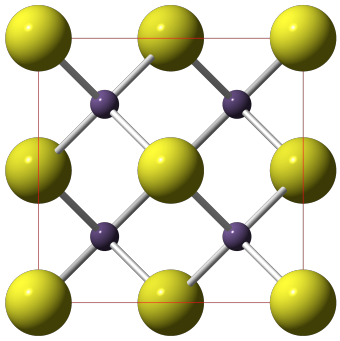

(a) FCC zinc-blende lattice

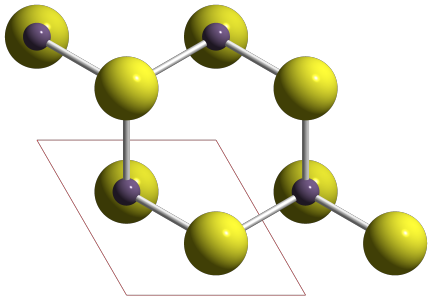

(b) HCP wurtzite lattice

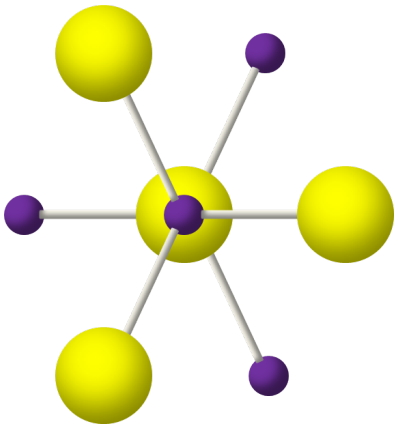

(c) ZnS tetragonal bond in zinc-blende structures

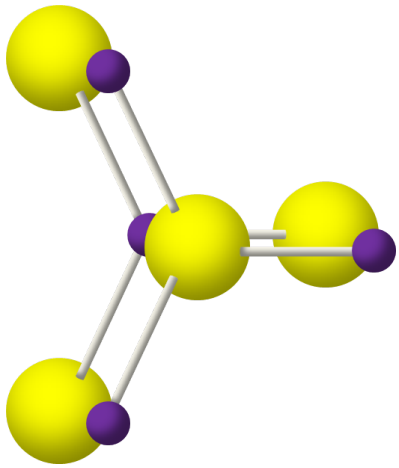

(d) ZnS tetragonal bond in wurtzite structures

Figure 3.3: ZnS lattice structures for (a) zinc-blende and (b) wurtzite. The lattices show the sulfur anions in yellow and the zinc cations in purple. The tetragonal bond of the (c) zinc-blende undergoes a rotation under high temperatures resulting in the (d) wurtzite bond. Figures produced using [85].

3.1.4 Transparency

The transparency of the ceramic will be effected by several factors including the phase transitions, grain sizes, voids, and defects. Transparency is a result of controlling the scattering centers within the material and the absorption of the various electronic structures within the material. Scattering or absorption can be caused by properties such as defects, grain boundaries, or voids. Sintering generally removes voids and defects improving transparency, but can also cause grain growth that can be detrimental to transparency. Scattering also occurs when there is heterogeneity in the crystalline phase. Phase heterogeneity results in alternating indices of refraction (2.3691 and 3.72 (at 589 nm) for zincblende and wurtzite, respectively [86]) which causes greater attenuation [83]. As such, the sintering profile (i.e. the heating rate, dwell temperature, dwell time, and pressure) and starting powders will have a large impact on transparency [56, 57, 83, 84, 87].

3.1.5 Luminescence of Zinc Sulfide

In addition to phase changes, sintering can also impact luminescence by changing dopant and defect concentrations. Luminescence in ZnS, like many inorganic semiconductors, occurs due to the band structure created from long-ordered crystalline bonds—resulting in a valence and conduction band. For cubic ZnS, the band-gap energy separating these bands is 3.54 eV [70], whereas bulk wurtzite ZnS has a band-gap energy of 3.91 eV. Heterogeneity of the crystal causes perturbation in the band-structure resulting in splitting of the energy states (see Figure 3.4) [88]. These changes to the electronic structure result in changes to the wavelength of emission.

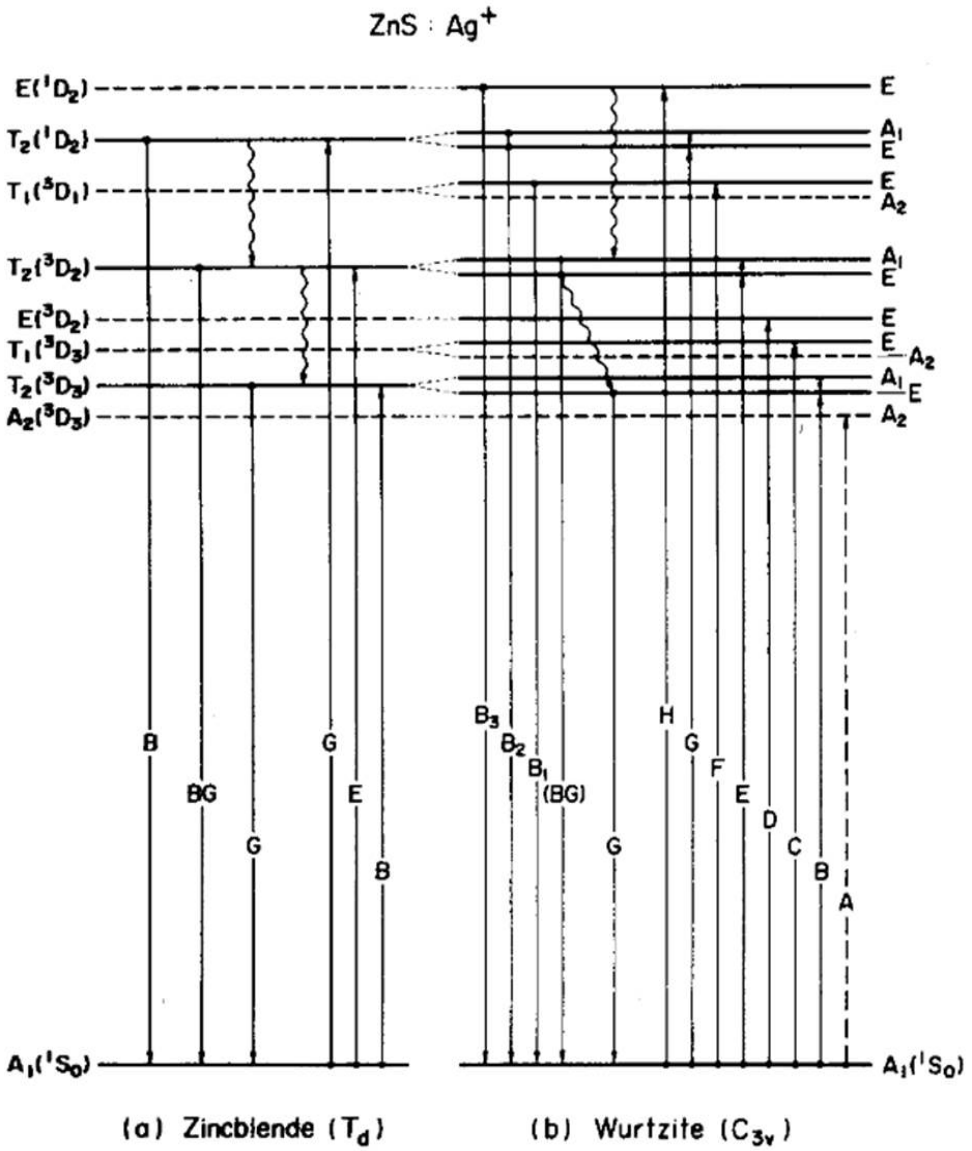

Figure 3.4: Band model, as proposed by Uehara for ZnS:Ag in zincblende (a) and wurtzite (b) structure. The wavy downward arrows represent radiation-less transitions. The dashed horizontal lines represent forbidden states with varying concentrations of oxygen (1 mol % (*a*) and 0.1 mol % (*b*) at 80K). Figure reproduced with permission from [88].

Dopants and defects also have a major impact on the emission of light. The presence of these impurities in the crystal cause perturbations in the band structure creating

intermediary states within the forbidden band-gap of the crystal. Figure 3.5 provides a simplistic diagram showing the resultant band structure created by natural defects in ZnS nanoparticles (also applicable to bulk ZnS).

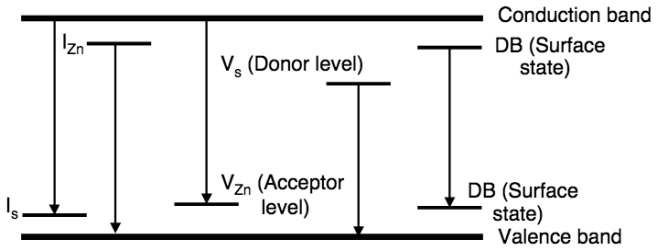

Figure 3.5: Schematic energy level diagram for the point defects and surface states of colloidal ZnS nanoparticles. Figure reproduced with permission from [89].

Recombination across these intermediary states is often more favorable than recombination across the band-gap. Additionally, these impurities tend to create localization of charge that attract charge carriers due to slight differences in electro-negativity. For these reasons, impurity sites are often referred to as luminescent centers.

In un-doped ZnS, luminescent centers are typically the result of zinc interstitials ($Zn_i^{\bullet\bullet}$) and sulfur vacancies ($V_S^{\bullet\bullet}$) due to a zinc-rich stoichiometry during crystal growth. If the crystal is grown in a sulfur-rich stoichiometry, the defects are predominately sulfur interstitials (S_i'') and zinc vacancies (V_{Zn}'') [90, 91]. Silver (Ag^+) and copper (Cu^+ or Cu^{++}) are common dopants in ZnS and commonly occupy interstitial sites (i.e. $Ag_i^{\bullet}$) or zinc vacancies (i.e. Ag_{Zn}'). These defects also create localization of charge that attracts free carriers consequently facilitating the luminescent process.

Emission from luminescent centers within ZnS (especially ZnS(Ag)) is commonly seen between 420 and 470 nm. Some theories attribute this emission to transitions from the conduction band to a deep acceptor level created by V_{Zn}' [90–94]. Another common emission occurs at ~520 nm and is attributed to transitions from deep donor

states created by either sulfur vacancies or interstitial dopants to the valence band [92, 95].

The integral role these dopants and defects play in the luminescent process can be effecting by sintering. The sintering process can have an annealing effect on the crystal thereby removing defects or cause dopants to migrate out or additional impurities to migrate into the ceramic. Uniaxial press techniques often use sacrificial graphite to separate the powders from the punches and die. This graphite presents a source of carbon that is likely to contaminate the ceramic during sintering. This contamination is readily seen using the FAST technique due to the high currents that facilitate carbon migration. High carbon content can degrade both luminescence and the transparency of the ceramic.

3.2 Fabrication

The fabrication process was developed to determine whether luminescent ceramics could be fabricated from commercial powders of ZnS(Ag) and BN using FAST. An iterative approach was taken to refine the process from lessons learned and alter the process to explore various aspects as questions arose. The generalized process is presented in Figure 3.6 which includes pre-processing to combine powders and prep them for sintering, the sintering process, and post-processing to polish the samples in preparation of analysis.

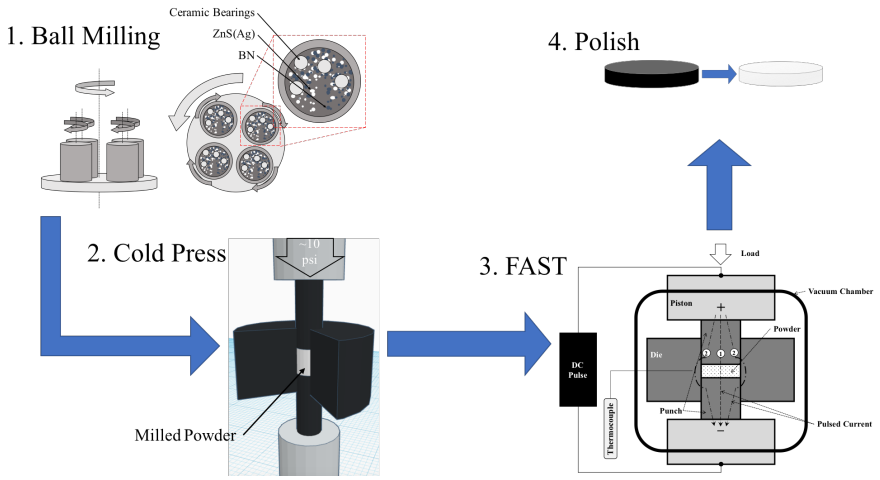

Figure 3.6: Fabrication Process. Powders are first mixed through ball-milling. The ball-milled powders are then loaded in the graphite die and pressed with a hand press. The powders are then hot-pressed in the FAST machine. Finally, the ceramic is polished.

The first iterations focused on sintering pure ZnS(Ag) to establish a baseline and then applied to ZnS(Ag) and BN. The ZnS(Ag) used in each ceramic was produced by Phosphor Technology. Early samples were fabricated from the GL-47/N-C1 product which has a reported median grain size of 8 μm. These ceramics confirmed the process could successfully densify the powders, maintain luminescence, and showed improved translucency. Subsequent trials included BN with the GL-47/N-C1 in a 1:87 mass ratio by lightly mixing the powders by mortar and pestle. The BN was unenriched and acquired from Sigma Aldrich with a reported grain size of about 1 μm. These BN:ZnS ceramics demonstrated similar densification and luminescence, although the mixing was inhomogeneous and the ceramic was not as translucent as the ZnS ceramic.

The next iteration of ceramics sought to improve the transparency by using smaller-grained ZnS powders and altering the mixing procedure. Many reports indicate ZnS ceramics sintered via uniaxial press from nanoparticles have achieved varying levels of transparency [56, 59, 84, 96, 97]. Ceramics sintered with 1 μm-sized ZnS powders have

also demonstrated some degree of transparency [87]. These reports prompted attempts to sinter ceramics from Phosphor Technology's GL-47/F-S1 product that has a median grain size of 4 μm. Subsequent ceramics sintered with BN in 1:87 and 1:22 mass ratios were ball-mixed at 9 Hz for 1 hour with the goal of reducing the heterogeneity of the mixture and increasing the reproducibility of the process. An additional ceramic of pure BN was sintered to observe the effects of sintering strictly on the BN.

In all trials, powders were loaded into a 2 cm diameter die with 2 layers of graphite paper lining the interior walls. The mass of the powder ranged from 1.3 to 5.2 g. In general, the better-quality ceramics were produced from trials using 5.2 g. Two layers of graphite also separated the powders from the punches. The punches were then cold-pressed by hand prior to loading in the FAST machine. Carbon felt was placed around and top of the die to provide insulation, except for two early trials. The felt insulation did not seem to make a difference in early trials, but later trials exploring the impact of the insulation suggest ceramics sintered without insulation experienced a large temperature gradient from the center of the ceramic to the edges based on changes in luminescence. Carbon fiber plates and graphite were also used between the punches and the piston plates to act as insulation and protect the pistons.

The temperature of the die was measured using a thermocouple. The thermocouple was fitted in a hole drilled in the side of the die that extended from the outer diameter to within a few millimeters of the inner diameter. This way the end of the thermocouple measures the temperature as close as possible to where the powders are being sintered. In cases where the temperature was greater than 1200°C, the temperature was measured using a pyrometer that measured the temperature from an exposed surface of the die. The thermocouple provides feedback to the machine which adjusts the applied voltage to correct the temperature in accordance with the desired temperature. The proportional,

integral, and differential (PID) settings for this feedback algorithm were set using a calibration runs under the same experimental parameters; namely, the diameter of the die, the powders being sintered, the initial mass of the dies, with/without insulation, and the applied pressure. Acquiring appropriate PID settings has a significant impact on the resultant ceramic and minor changes in the press configuration can result in applied voltages that either overshoot or undershoot the desired temperature.

After the die was mounted in the machine, the pressure on the punches was set to 30 bar using a 9.6 cm^2 piston. The chamber was then evacuated to about 0.3 mbar. Under an evacuated atmosphere, the temperature was increased to 300 degrees at which point 164 bar (50 MPa—the maximum pressure sustainable by the punches) of pressure was applied. The temperature was increased to the desired temperature and allowed to dwell at that temperature for the desired amount of time. The heating rate was approximately 50°C min^{-1}. The temperatures explored in this effort ranged from 750 to 1300°C and the dwell times ranged from 5 to 180 min (a summary of the explored phase space is provided in Figures 3.8 and 3.9). After the dwell time expired, the voltage was turned off and the die and punches were allowed to cool. Once the temperature had reached 300°C, the pressure was decreased to 30 bar and the die was allowed to continue cooling to 50°C at which point the vacuum was released.

An example of a typical sinter profile is provided in Figure 3.7. The piston height in Figure 3.7 provides a means of measuring densification. As the pressure increases, the piston pushes the top punch down on the powder resulting in the removal of voids and densification. Heat also aides in densification, but also causes the punches to expand which is the cause of the decrease in piston height during the cooling cycle.

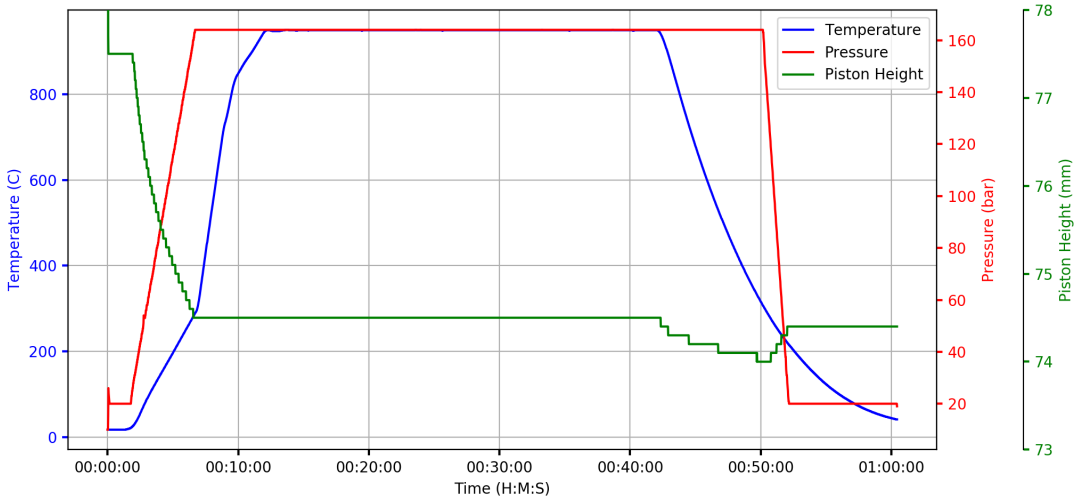

Figure 3.7: Typical sinter profile.

Figure 3.8 provides a summary of the phase space of temperature and dwell time explored with the N-C1 and F-S1 powders. Figure 3.9 provides a summary of the phase space of temperature and dwell time explored with composite ceramics the N-C1 and F-S1 powders.

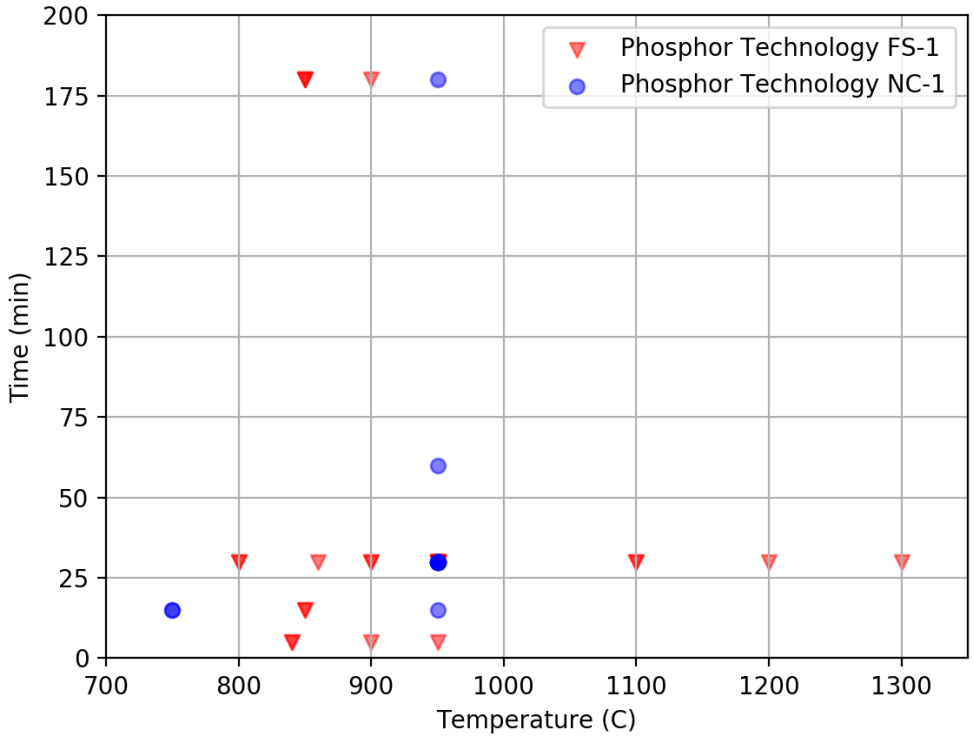

Figure 3.8: ZnS ceramic sinter profile phase space summary.

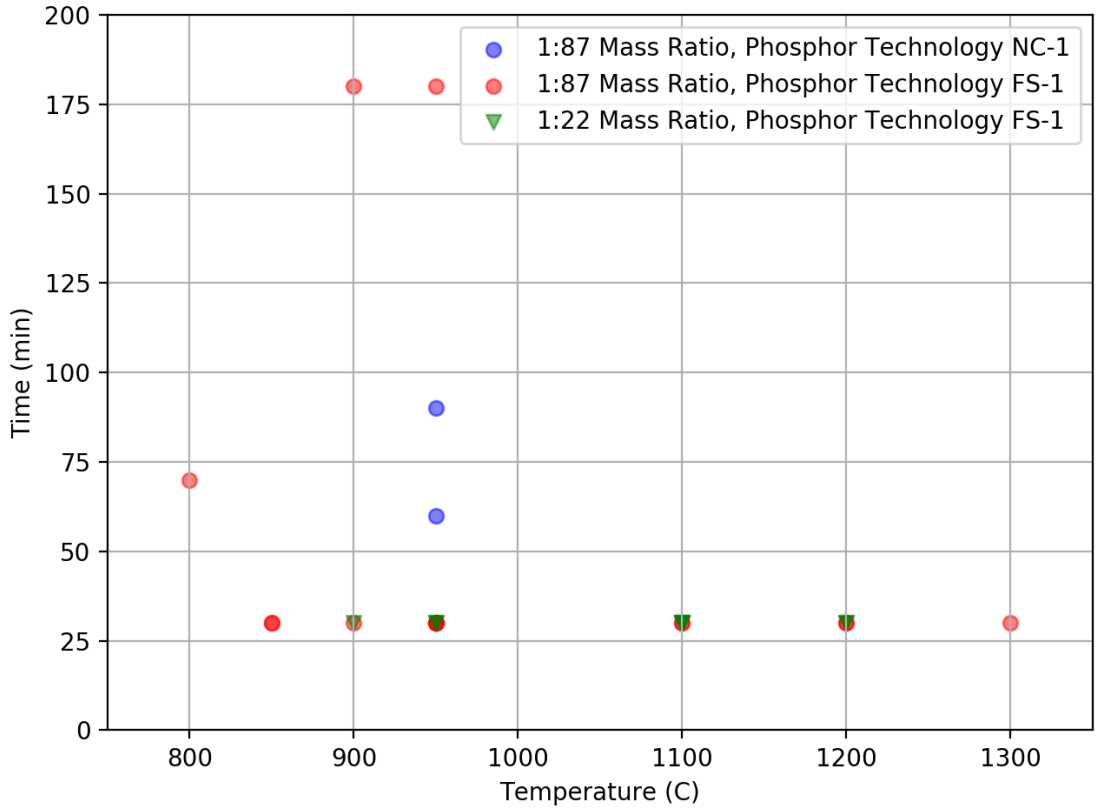

Figure 3.9: BN:ZnS ceramic sinter profile phase space summary.

The post-sintering process included removal of the ceramic and polishing. Due to the softness of the ceramic, polishing was accomplished by hand. Initial polishing was done with silicon carbide paper up to grade 2500. This removed excess graphite paper and provided some degree of polish to the exposed ceramic. In some instances, the ceramics were cut in two to form thin discs and then polished in diamond slurries (up to 1 μm suspensions).

3.3 Characterization Techniques

A summary of the variety of techniques used to assess the ceramics is provided in Figure 3.10. Characterization of the ceramics began with visual inspection with a 395 nm UV light to qualitatively assess the luminescence intensity, contamination, densification/sintering, and transmittance. The favorable qualities or unexpected results of select ceramics were further explored using x-ray diffraction to assess the phase composition of the ceramic, scanning electron microscopy to view densification at the surface of the ceramic, cathodoluminescence to view the distribution of luminescent particles, microscopy under UV illumination, and photoluminescence to quantify the emission spectrum.

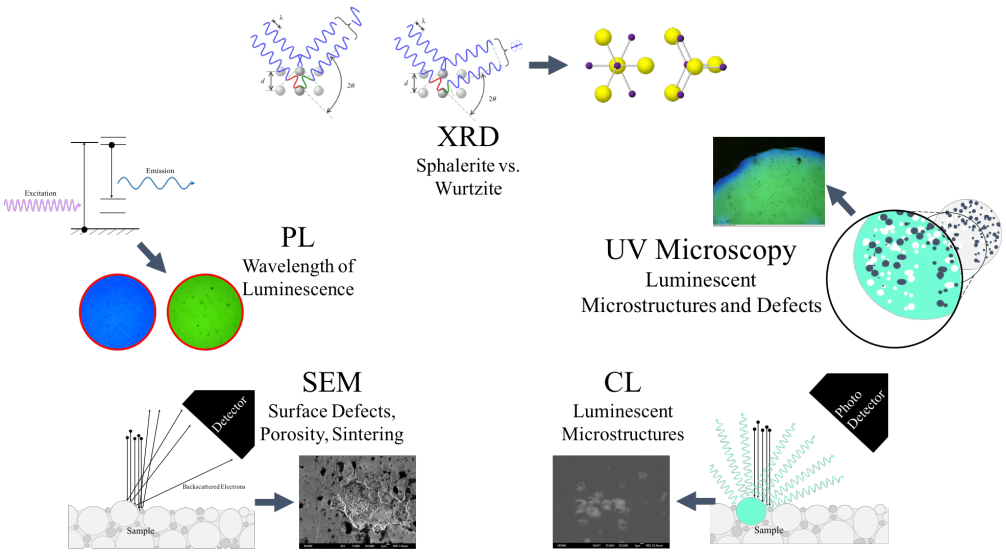

Figure 3.10: Characterization techniques used on ceramics.

3.3.1 X-ray Diffraction

As described above, the crystalline phase of the ceramic is important as it relates to luminescence. Sintering profiles that tend to produce wurtzite were determined through

x-ray diffraction (XRD).

XRD is a technique that exploits the phenomenon of diffraction produced from x-rays scattering from the crystalline lattice. Diffraction is the pattern created from constructive and destructive interference of photons scattered from an object, an array of objects, or slits. It is particularly prominent when the dimensions of the object or slit are comparable to the wavelength of the incident photons. X-rays produce a diffraction pattern when incident on crystals because the wavelength (~ 0.15 nm) is on the order of the interatomic spacing of atoms in the crystalline lattice. These incident x-rays accelerate atomic electrons causing them to oscillate and re-radiate a spherical electromagnetic wave at the same wavelength of the x-ray—thus scattering the x-ray. The spherical waves emanating from the array of atoms in the crystalline lattice destructively interfere with one another except at angles related to the interatomic spacing where the waves constructively interfere or are coherent. This relationship is described by Bragg's law,

$$2d \sin\theta = n\lambda_{\text{x-ray}}. \tag{3.1}$$

where, d, is the interatomic spacing, θ is the angle of incidence of the x-rays with respect to the crystallographic plane, n is an integer related to the number of wavelengths the coherent wavelengths are shifted, and $\lambda_{\text{x-ray}}$ is the wavelength of the x-ray.

In XRD measurements, the sample is rotated so that x-rays interact with the various crystal planes over a broad range of angles. At each sample position, a detector measures the x-ray intensity over a range of angles with respect to the axis of the source beam. The maxima are measured at 2θ from the incident beam axis. Using these results and the known wavelength of the x-ray the interatomic spacing, d, can be calculated. Multiple maxima will be measured at various angles due to the multiple plane orientations that

result in different spacing between atoms. The lattice spacing is related to the Miller indices of the planes by,

$$d_{\mathrm{hkl}} = \frac{a}{\sqrt{\mathrm{h}^2 + \mathrm{k}^2 + \mathrm{l}^2}}, \tag{3.2}$$

where a is the lattice constant of the crystal. From these multiple maxima, the plane orientation and lattice constant of the material are determined.

Comparing the XRD pattern to reference patterns confirms the phase content of the samples. Reference patterns for sphalerite ZnS, wurtzite ZnS, and hexagonal BN are shown in Figure 3.11.

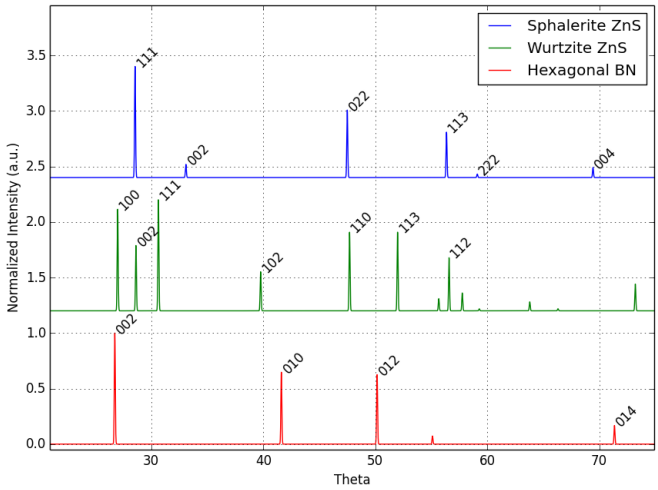

Figure 3.11: XRD pattern of sphalerite and wurtzite ZnS and hexagonal BN [98].

XRD crystalline phase analysis of powders and ceramics was accomplished using a Rigaku MiniFlex XRD with a 0.152 nm Cu_{α} x-ray source.

3.3.2 SEM/Cathodoluminescence

Scanning electron microscopy (SEM) is a technique that uses a beam of focused, high-energy electrons to generate byproducts from the scattering with the target material. The byproducts are based on the energy of the incident electron and characteristics of the target material—thus the byproducts carry information unique to the sample and the location where the interaction occurred.

The byproducts produced are related to the energy transferred with each scattering event through the sample—either elastic or inelastic. Elastic scattering events occur as the electrons interact with the material without transferring energy. In these events the electron is scattered by the Coulomb attraction of the nucleus,

$$F = \frac{q_{\text{electron}} Q_{\text{nucleus}}}{4\pi\epsilon_0 r^2}. \tag{3.3}$$

The force increases with greater charge from the nucleus (higher Z nuclei) and/or smaller separation (r) resulting in greater deflection of the electron. For very thin samples (less than 100 nm), the electrons will pass through the sample after scattering off the nuclei in the material. This is the basis for transmission electron microscopy (TEM). In some instances, the force is significant enough to reflect the electron. The occurrence of these backscattered electrons is proportional to the Coulombic force and therefore reveal the atomic number of the target material.

Inelastic scattering occurs as energy is transferred to the material either through excitation/ionization of atomic electrons, production of photons from Bremsstrahlung, production of phonons, or the production of plasmons. Incident electrons can transfer energy to atomic electrons if the energy transferred exceeds the threshold for interaction (i.e. the work function or binding energy). Ionized electrons—or secondary electrons—

that occur near the surface of the specimen reveal topographic information and is the basis for SEM.

Vacancies in the electronic shells created by the excited or ionized electrons leave the atom in an energetic state. As the atom relaxes back to the ground state, photons can be created or additional electrons can be released. Luminescence occurs as electrons from higher states recombine with holes in lower states resulting in the emission of a photon. If the hole is located on an inner electronic shell, the process of luminescence emits a photon with energy in the x-ray region (characteristic x-rays). Holes located in valence states or the valence band may recombine with electrons in the conduction band or the outermost valence states resulting in photons in the UV to IR region (cathodoluminescence). The wavelength of the photons is characteristic of the atom and reveals atomic composition and information regarding the electronic states. It is also possible for electrons to be produced during the process of relaxation. When a hole on an inner shell recombines with an electron in a higher electronic shell, the energy released can couple to other atomic electrons rather than producing an x-ray. These emitted electrons are called Auger electrons and have energies that are also characteristic of the atom.

Other inelastic processes include Bremsstrahlung, phonons, and plasmons. The Coulombic force between the electron and the target nucleus causes an acceleration (change in the velocity vector) that results in the scattering. During an inelastic process, this acceleration results in a decrease in the magnitude of the electron's velocity and transfer of this energy in the production of an x-ray in a continuous spectrum related to the energy transferred—a process known as Bremsstrahlung, or "braking" radiation. Electrons can also transfer energy to the material through production of phonons. These lattice vibrations occur at lower energies and are the primary source of heat. Excessive phonon production can result in damage to the material. Lastly, electron energy can also

be transferred to weakly bound or free electrons in the form of plasmons. When the electron beam passes through a cloud of free or weakly bound electrons (most commonly in the conduction band of a metal), it can couple to this cloud producing a collective oscillation associated with the transfer of energy.

These products are produced from varying depths within the material, but only those products that escape provide information about the specimen. The depth and volume that the electron beam penetrates the material are dependent on the beam energy, atomic density, and atomic number of the material constituents, as derived by the Kanaya-Okayama formula [99],

$$R = \frac{5.025 \times 10^{-12} A E_0^{\frac{5}{3}}}{\rho \lambda_s Z^{\frac{8}{9}}}, \tag{3.4}$$

where R is the penetration depth, A is the atomic weight (g mol^{-1}), E_0 is the beam energy (eV), ρ is the density (g cm^{-3}), and Z is the atomic number. Kanaya, *et. al.*, found good agreement with this formula for beam energies from 10 to 1000 keV using a λ_s of 0.182 [99]. The type of interactions that occur at each depth is a function of the threshold for reaction and energy-dependent cross-section. The energy needed to create characteristic x-rays, Auger electrons, and Bremsstrahlung x-rays ranges from 100's to 1000's of eV; whereas, secondary electrons can be created with less than 10 eV and cathodoluminescence occurs in the range of a few eV. The energy of the incident electrons decreases with each successive scattering event as it passes through the material. This energy as a function of depth, x, can be estimated by [99],

$$E = \left(1 - \frac{x}{R}\right)^{\frac{3}{5}} E_0. \tag{3.5}$$

If the energy exceeds the threshold, one of the many scattering reactions can occur

at that depth; however, not all byproducts escape the material. The many electrons and x-rays have enough energy to produce tertiary electrons and visible photons from cathodoluminescence can be absorbed depending on the optical properties of the material. Because of these additional scatterings, the energy threshold for reaction, and the relation between electron energy and depth; byproducts detected escaping the material are often depth-limited.

Select samples were imaged with SEM using a JEOL 6500F scanning electron microscope. Some of these samples were also characterized using an Oxford Instruments CL attachment to the JEOL 6500F. Regarding ceramics, SEM is an informative tool as it provides qualitative information to surface morphology related to grain growth and densification. Because ZnS scintillates, cathodoluminescence also provides understanding of the size and distribution of ZnS particles. Cathodoluminescence also is a means of confirming the luminescent properties and measuring the band structure of the luminescent centers.

3.3.3 Photoluminescence and UV Microscopy

As discussed above, fabricating a luminescent ceramic is a major goal of this effort. To ascertain how the luminescent properties (also described above) change with sintering, the ceramics were characterized with photoluminescence (PL) and UV microscopy. Both techniques use UV light to excite electrons from the valence band to the conduction band. The visible light emitted by the ceramics is collected and analyzed. In the case of PL, the light is transmitted to a spectrometer where the intensity of light is measured over a range of wavelengths of interest. UV microscopy provides an imaging tool to visualize different luminescent features.

Excitation was accomplished via a ThorLabs M365FP1 365 nm LED. The source was fiber-coupled to a probe that excited the surface of the ceramic at a 45° angle. A second probe collected light normal to the surface and transmitted the light via fiber to a OceanOptics USB 2000 spectrophotometer. The spectrophotometer was set to a 300-microsecond integration time and averaged over 2 scans. The spectrum was corrected for background and electronic dark noise. Due to differences in surface polish, these measurements can only provide the relative intensity of peaks for each sample and cannot be used to measure the light yield from sample to sample.

Normalized PL measurements of the Phosphor Technology ZnS(Ag) and the Sigma Aldrich BN powders are provided in Figure 3.12 for reference when comparing the luminescence of the ceramics. There is no noticeable difference between the spectra of the two ZnS(Ag) powders. Both powders exhibit the well-documented 450 nm peak and another peak around 470 nm. Per the model proposed by Morozova, the 450 nm peak is likely related to the Ag(I) state. Morozova's model, however, does not identify a transition associated with the emission at about 470 nm.

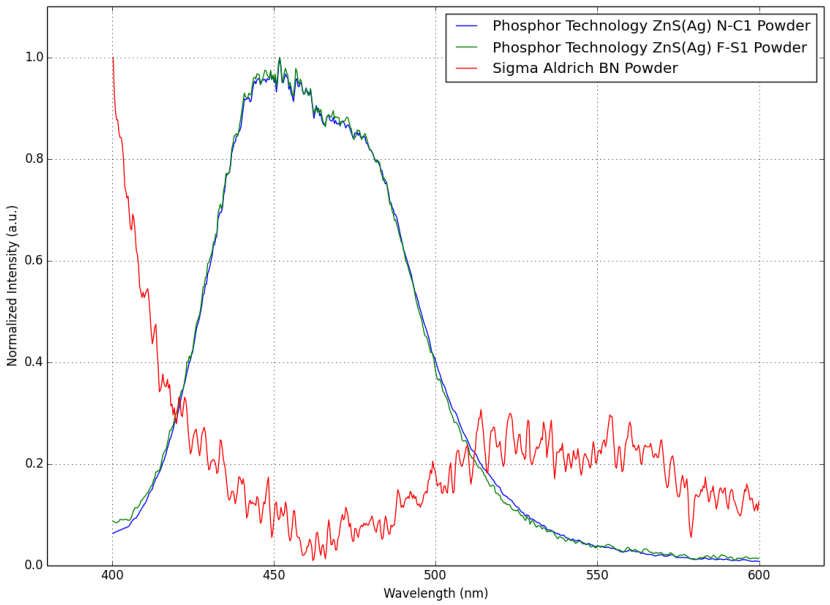

Figure 3.12: Photoluminescence of ZnS(Ag) and BN powders excited by 365 nm source.

UV microscopy was accomplished using a Dino-Lite 4115 USB microscope with a 375 nm LED for sample illumination. Various magnifications were used to explore luminescent and non-luminescent features.

3.4 Results and Discussion

3.4.1 ZnS(Ag) Ceramics

Figures 3.13 and 3.14 shows selected ceramics from sintering the N-C1 and F-S1 ZnS(Ag) powders, respectively. Inlaid on each image of the ceramics is an image taken of the ceramic using UV microscopy.

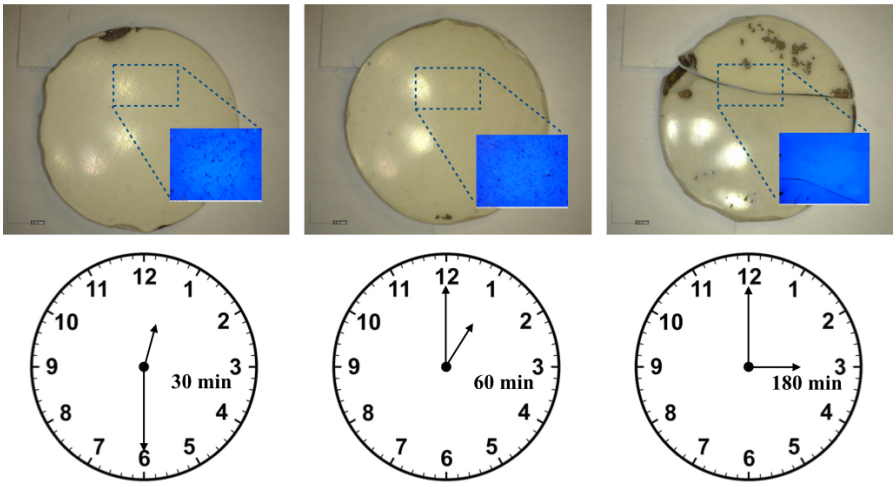

Figure 3.13: Images of ceramics sintered from N-C1 powders at 950°C for varied times. Insets on each image show an image taken using UV microscopy.

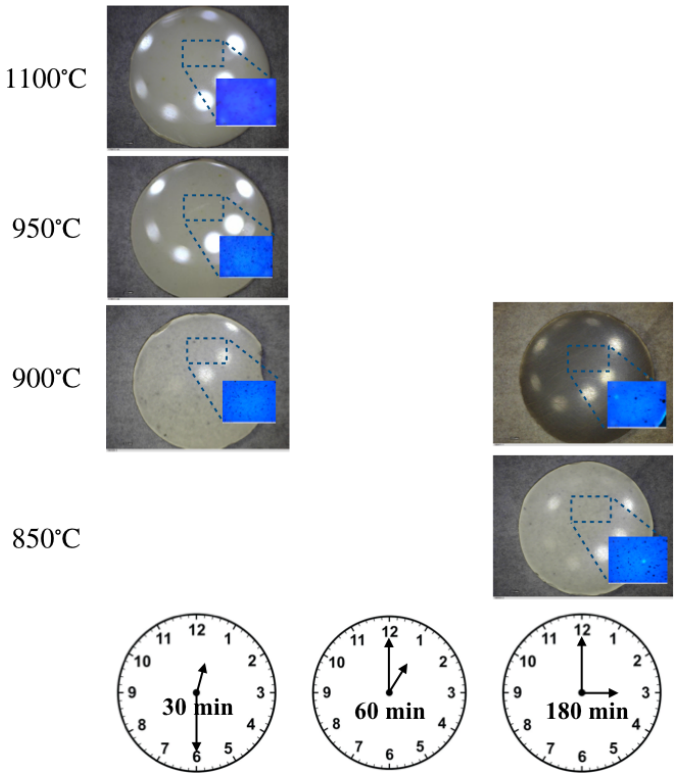

Figure 3.14: Images of ceramics sintered from F-S1 powders at varied temperatures for varied times. Insets on each image show an image taken using UV microscopy.

The darkening and discoloration of the ceramics is apparent from these images. Generally, more darkening was found in ceramics sintered at higher temperatures or ceramics sintered for longer dwell times. Asymmetric darkening is often observed when comparing one side of the ceramic to the other. Visual observation of the ceramics shows micron-sized centers of discoloration rather than a homogeneous dispersion. The size of the discoloration centers also tend to grow with sintering time.

The graying is thought to be due to migration of carbon into the ceramic from the graphite paper that surrounds the powder [100]. If carbon migration is the source of this contamination, it may be due to thermionic emission of carbon ions related to the high temperatures or due to field emission due to the high voltages. Field emission of carbon ions may explain the asymmetric discoloration phenomenon as one might expect a higher concentration of carbon near the cathode. The darkening centers may also be explained by the field emission theory as the current may create preferential paths through the powder resulting in the heterogeneous dispersion.

The images also show reflections of the light source. This reflection serves as a qualitative indicator of the quality of surface polish which is dependent on the polishing process and the residual porosity of the ceramic. The ceramics show a general trend of greater reflection with increased temperature and/or time. This trend is likely due to improved densification. Due to the soft nature of the ceramic, polishing by hand allowed for quick assessments of densification. Ceramics of high densification required minimal polishing to achieve a high gloss, while ceramics with high residual porosity remained dull even after additional polishing at finer grains.

Densification at higher temperatures and dwell times is consistent with expectations. Powders sintered at 750°C (not shown in the images) experienced the least densification and resembled chalk rather than a ceramic. Densification improved for ceramics

sintered at 800°C for times greater than 60 min and ceramics sintered at 850°C for 30 min. However, with increased time and/or temperatures also came increased wurtzite ratios and/or higher carbon migration from the graphite and at temperatures greater than 1100°C, the ZnS powders tended to melt. Figure 3.15 demonstrates the transition from cubic to wurtzite with increased sintering temperature.

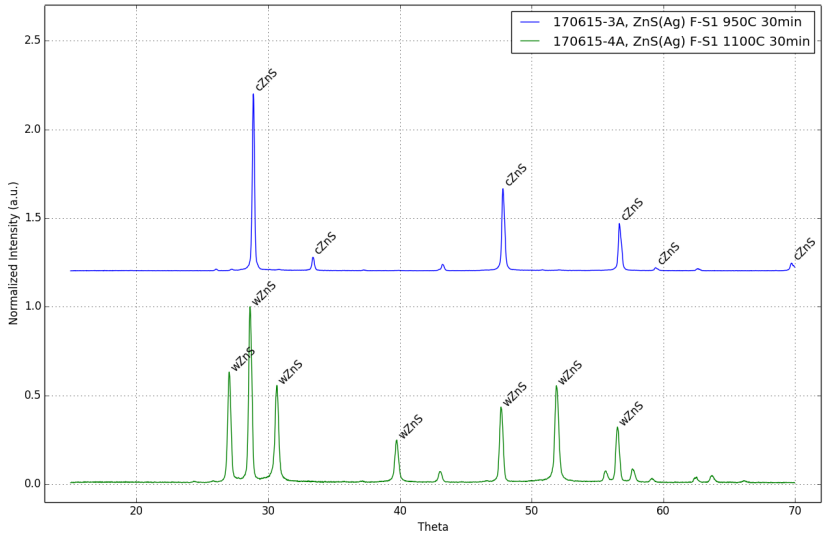

Figure 3.15: XRD of ceramics sintered with ZnS(Ag) F-S1 powders at 950 and 1100°C. Cubic ZnS peaks are labeled "cZnS" and wurtzite ZnS peaks are labeled "wZnS".

The impact of this phase change is apparent in the PL measurements. The normalized PL measurements for the 170615-3A sample sintered at 950°C in Figure 3.16 shows little difference compared to the PL of the Phosphor Technology powders shown in Figure 3.12. The 170615-4A ceramic sintered at 1100°C, however, shows a decrease in relative intensity at approximately 470 nm and a shift in the 450 nm emission towards 440 nm. This is consistent with Uehara's observations and indicative of the perturbation of the conduction band caused by the crystalline transition [88]. This change to a darker

blue is almost imperceptible in the UV microscopy images inlaid in Figure 3.16.

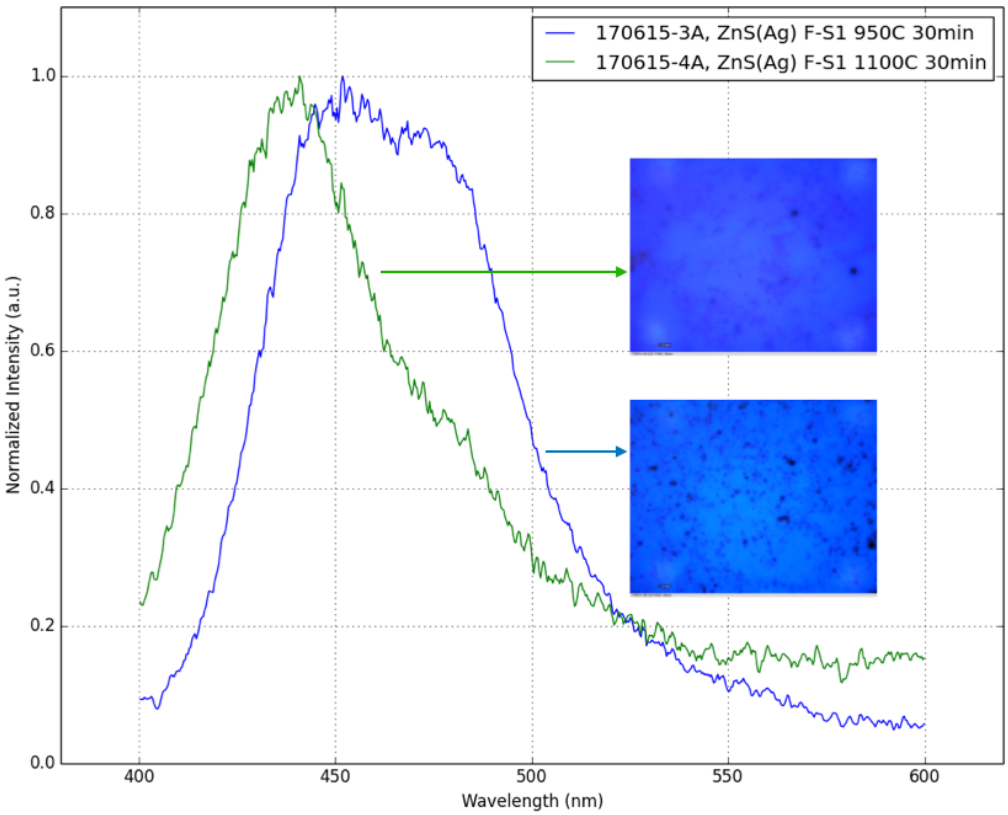

Figure 3.16: Photoluminescence of ceramics sintered with ZnS(Ag) F-S1 powders at 950 and 1100°C excited by 365 nm source. Inlaid in the plot are images of the ceramics using UV microscopy using a 365 nm source.

Qualitative comparisons of the ceramics sintered from N-C1 and F-S1 powders at 950°C for 30 min suggest the N-C1 ceramics have less contamination and better translucence. This difference is assumed to be attributable to the grain size. Smaller grain sizes are known to densify at lower temperatures and may result in additional grain growth [82]. This difference may have accelerated the migration of carbon and created larger grains that contributed to greater attenuation. The kinematics of the sintering process as it relates to starting grain size is an obvious area for further study.

3.4.2 BN:ZnS(Ag) Ceramics

Trends of improved densification with temperature and/or time seen in the pure ZnS ceramics with the best results appearing to be in the region of 950°C and 30 minutes. This sintering temperature and dwell time served as the basis for much of the sintering exploration done with the composite BN:ZnS ceramics. The first ceramics sintered with the composite powders showed unexpected differences in crystalline phase changes. The addition of BN appeared to prevent transitions from cubic ZnS to wurtzite, even when the ceramic was sintered for longer dwell times. This phenomenon was first observed in the PL measurements of the 160808-4 ceramic (ZnS(Ag) N-C1 powder sintered at 950°C for 30 min) and the 160816-4 ceramic (BN:ZnS(Ag) (N-C1) in a 1:87 mass ratio sintered at 950°C for 90 min), shown in Figure 3.17. The pure ZnS(Ag) ceramic shows the luminescence consistent with the phase transition to wurtzite, as described above, whereas the BN:ZnS ceramic shows no such transition even after tripling the dwell time. These initial experiments with adding BN to the sintering process demonstrated the feasibility of fabricating a composite ceramic without detriment to the PL.

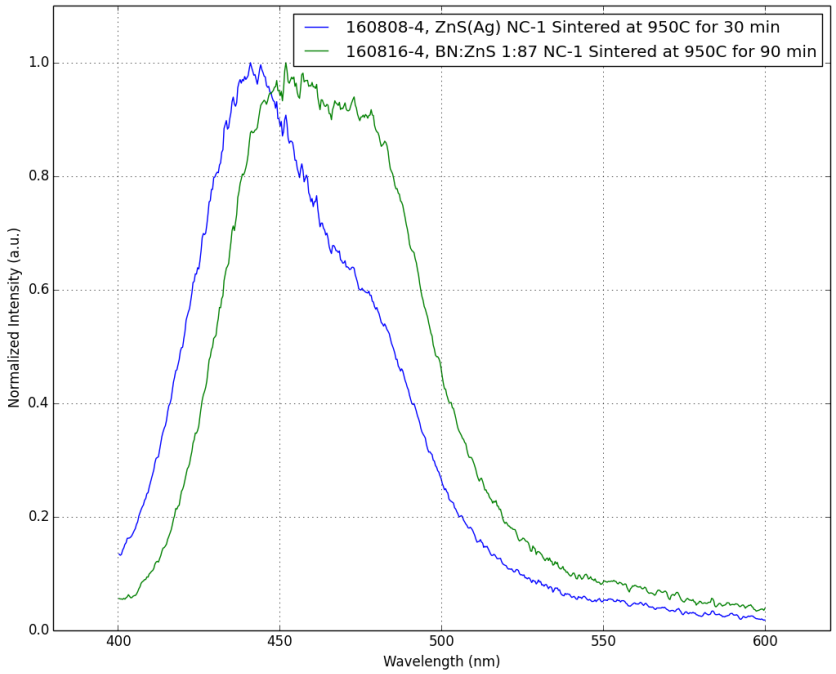

Figure 3.17: Photoluminescence of ceramics sintered with ZnS(Ag) N-C1 and BN powders excited by 365 nm source.

The suppressed phase transition observed in the PL is supported by XRD measurements of the ceramics, shown in Figure 3.18. The XRD pattern of the ZnS ceramic shows peaks consistent with a partial transition to wurtzite. The diffraction pattern of the BN:ZnS shows no signs of transition to wurtzite. Nor does the pattern show any confirmation of hexagonal BN. The peaks where BN should register a signal are included in the figure to show this technique is not sensitive enough to register those grains in such low concentrations. The diffraction pattern and the luminescence spectrum suggest the addition of BN suppressed the transition to wurtzite even at longer sintering times.

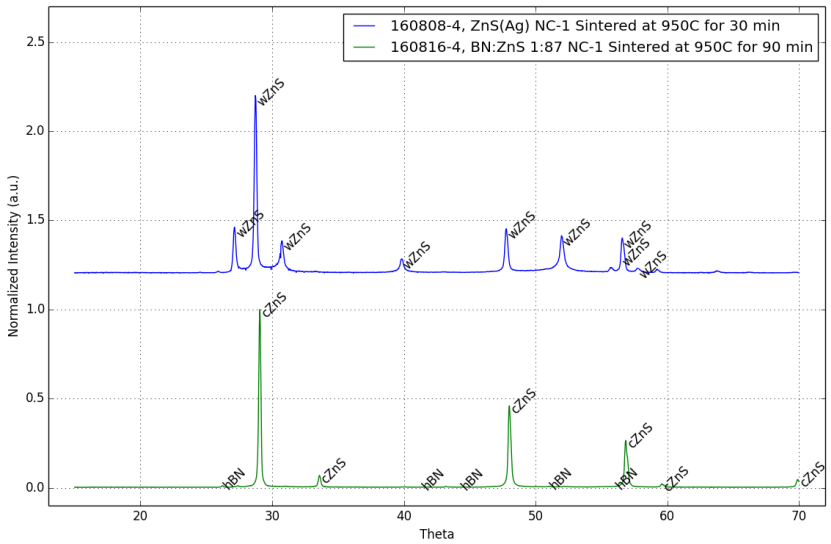

Figure 3.18: XRD of ceramics sintered with ZnS(Ag) N-C1 and BN powders. Cubic ZnS peaks are labeled "cZnS", wurtzite ZnS peaks are labeled "wZnS", and the location of expected hexagonal BN peaks are labeled "hBN".

The effects of adding BN to the ceramic in these early trials prompted further exploration of the effects at higher temperatures in hopes of improving densification. These trials were conducted with F-S1 powders under the assumption that the smaller grains might additionally improve transparency. Figure 3.19 shows the results of these trials for different mass ratios and different temperatures. Inlaid on the images of each ceramic are images of the ceramics using a UV microscope to highlight the transition of the luminescent properties. The BN:ZnS ceramic sintered at 950°C (170616-6A), like the 160816-4 ceramic, shows no detriment to luminescence. At higher temperatures, however, the BN:ZnS ceramics demonstrate dramatic changes in the luminescence. Rather than shifting to deeper blues consistent with a transition to wurtzite, the luminescence shifts to green.

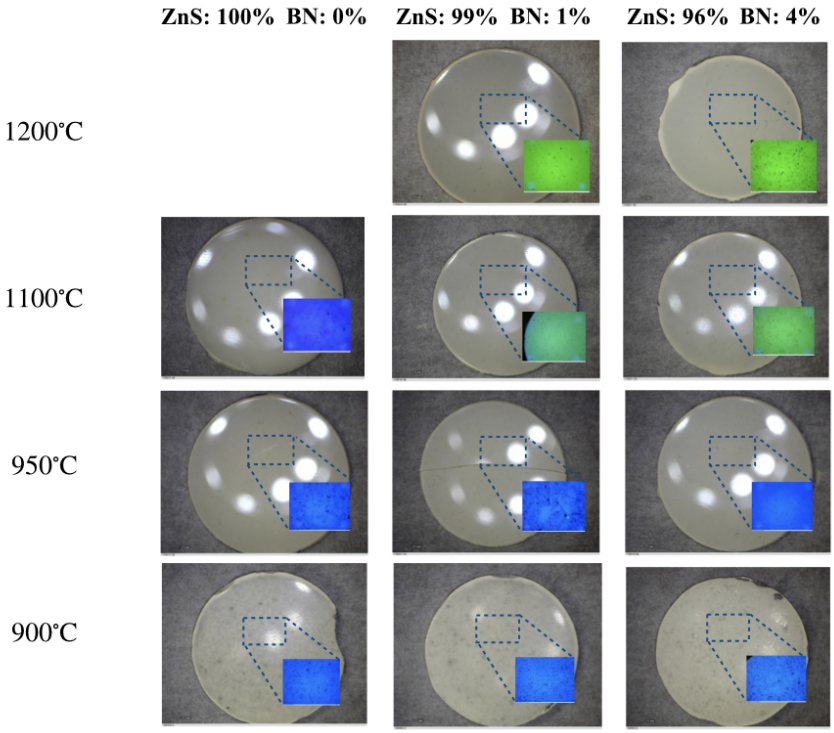

Figure 3.19: Images of F-S1 ceramics sintered for 30 min ordered according to sintering temperature and composition. Images from UV-microscopy are inlaid in the images to show the effect of mass ratio and sintering temperature on the luminescence.

The changes in luminescence with increased sintering temperature can be seen in the PL of the ceramics. At higher sintering temperatures, the 450 nm peak shifts towards 440 nm as expected for a wurtzite transition, however, the relative intensity significantly decreases. Instead a new, broad peak at 530 nm dominates the spectrum. This new peak could be attributed to deep donor states created by sulfur vacancies that are facilitated by the presence of the BN. At even higher temperatures, the 440 nm emission is completely replaced by the emission at 530 nm. This trend is seen in ceramics fabricated with both 1:87 and 1:22 mass ratios shown in Figure 3.20.

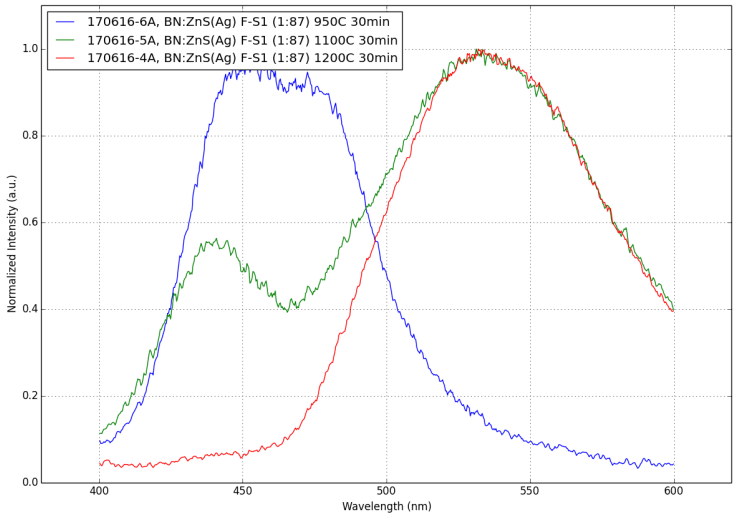

(a) PL of composite ceramics: 1:87 mass ratio

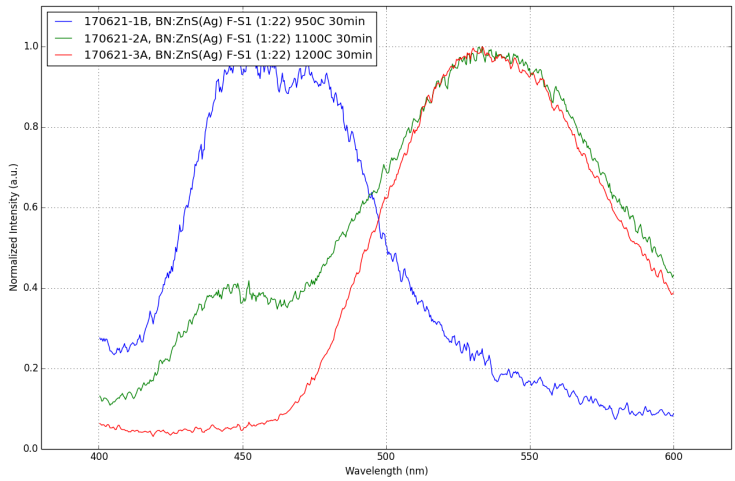

(b) PL of composite ceramics: 1:22 mass ratio

Figure 3.20: Normalized photoluminescence using a 365 nm source for ceramics sintered at 950, 1100, and 1200°C with ZnS(Ag) F-S1 and BN powders in mass ratios of (a) 1:87 and (b) 1:22.

XRD measurements of the ceramics, shown in Figure 3.21, confirm a transition to wurtzite of the 1706 samples with higher sintering temperatures. These results discount

the notion that the BN somehow suppresses the transition as initially thought.

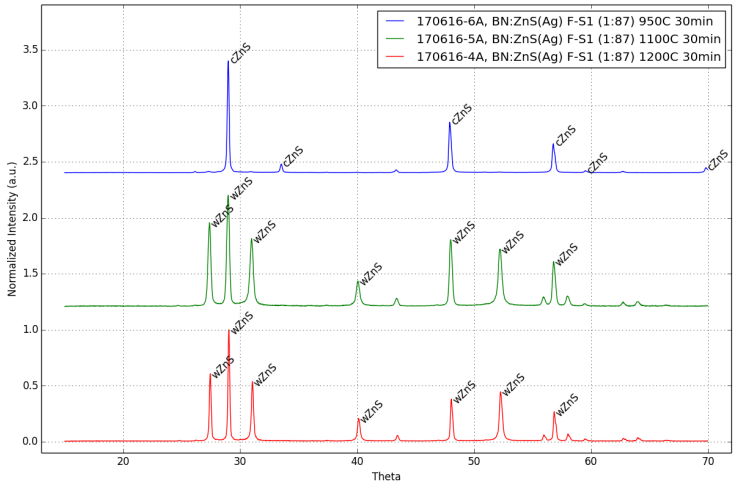

(a) XRD of composite ceramics: 1:87 mass ratio

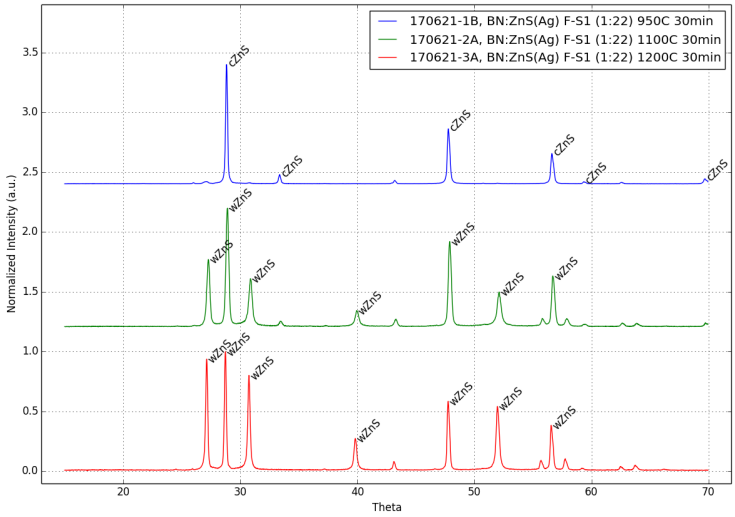

(b) XRD of ceramics: 1:22 mass ratio

Figure 3.21: X-ray diffraction for ceramics sintered at 950, 1100, and 1200°C with ZnS(Ag) F-S1 and BN powders in mass ratios of (a) 1:87 and (b) 1:22.

As the case with the early N-C1 composite ceramics, there is no indication of hexag-

onal boron nitride in the XRD patterns for either the 170616 or 170621 ceramics. The presence of BN in the ceramics is confirmed using SEM, shown in Figure 3.22. The BN can be seen as flakes lining the wall of an inclusion at the ceramic's surface. The inclusion may be the result of a large grain of ZnS being removed during the polishing process. The observation of the BN lining the wall of the inclusion suggest the BN may have prevented the grain of ZnS from sintering or adhering to the bulk ceramic. In this manner, the addition of BN may increase surface porosity of the ceramics.

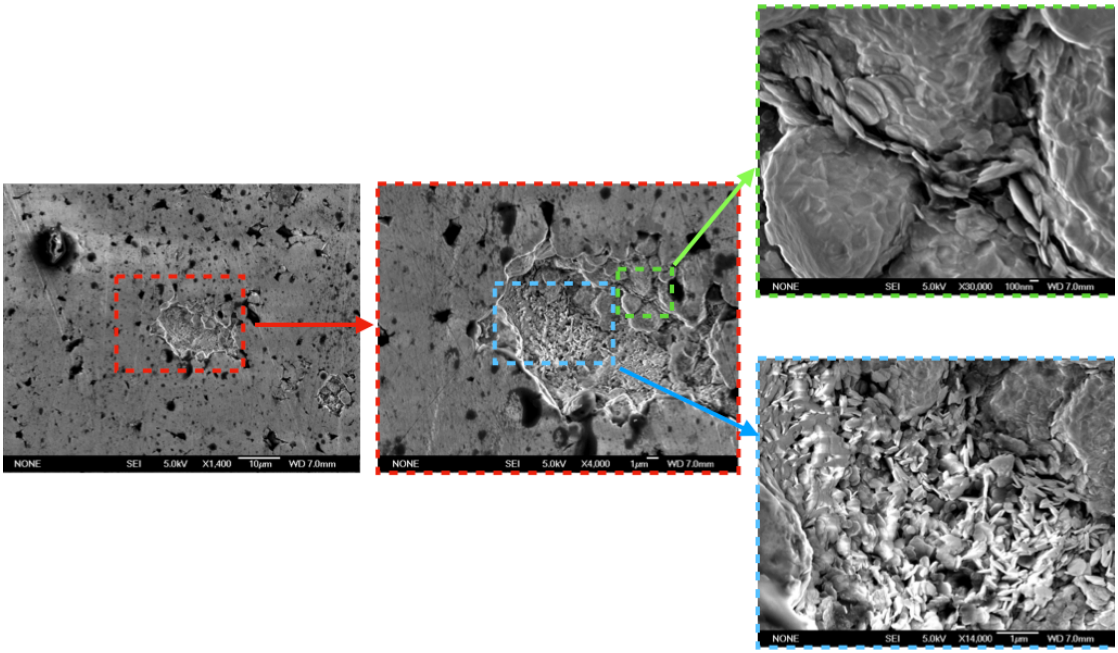

Figure 3.22: SEM images of the 160816-3 BN:ZnS(Ag). The highest magnification image of an inclusion of the ceramic shows small grains of BN.

Additional SEM images using cathodoluminescence of the ceramics and the Scintacor screens provide interesting comparisons of the difference in fabrication approaches. The CL images of the Scintacor screen, shown in Figure 3.23, confirm the ZnS grain size is on the order of a few microns and demonstrates the high volume ratio of binder.

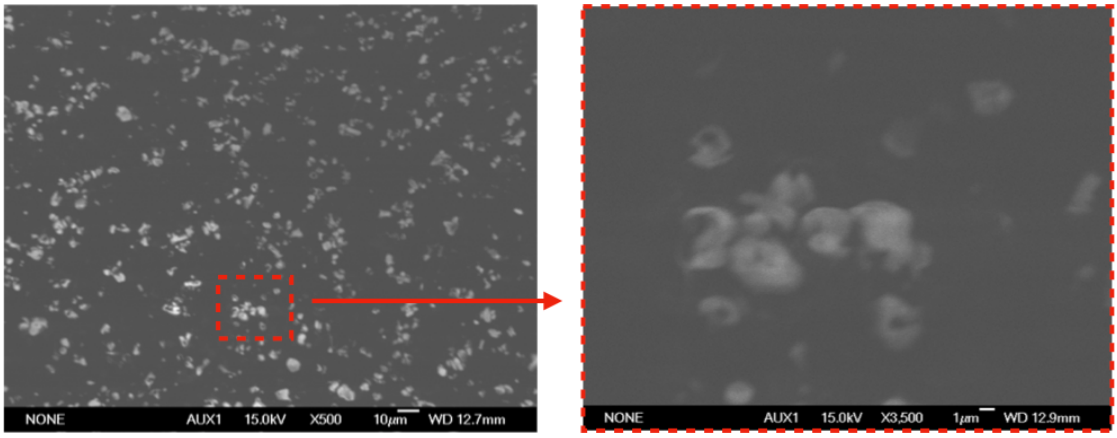

Figure 3.23: 425 nm emission from ZnS grains in a Scintacor screen with 1:2 ^{6}LiF:ZnS(Ag) ratio under excitation from electrons.

The CL images of the 160816-3 ceramic, shown in Figure 3.24, show the differences in luminescence between the ceramic and phosphor screens. The emission from the luminescent grains in the ceramics shows how much more diffuse the ZnS is in the ceramic compared to the phosphor screen. Of note in the CL images is the intensity of light emitting from the inclusion compared to the surface of the ceramic—a phenomenon possibly related to the surface reflections trapping light in the ceramic.

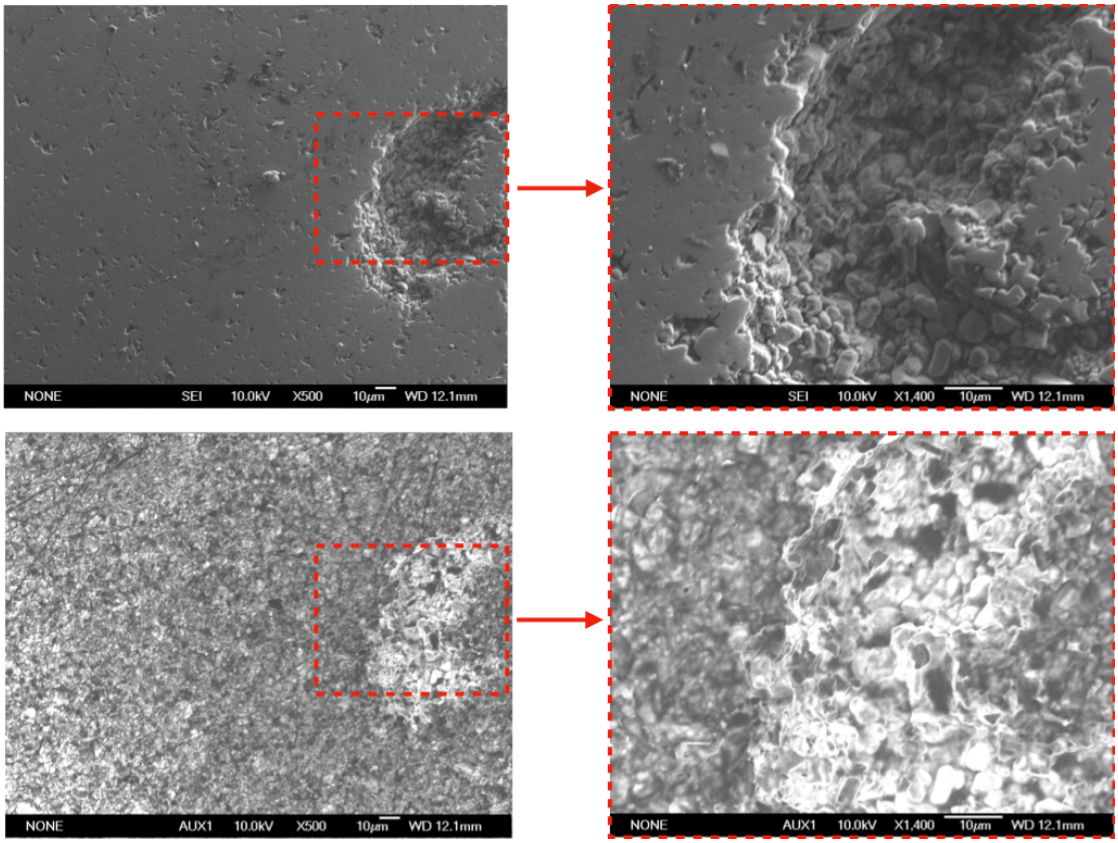

Figure 3.24: (Top) SEM images showing the surface and an inclusion in the 160816-3 BN:ZnS(Ag) ceramic. (Bottom) CL images of 435 nm emission from the 160816-3 BN:ZnS(Ag) ceramic. CL of the ceramic samples demonstrate the abundance of ZnS in comparison to the phosphor screens shown in Figure 3.23. Brighter luminescence from the inclusion region of the ceramic may be indicative of internal reflection due to the surface polish preventing light from escaping.

3.5 Conclusions and Recommendations

Successful composite ceramics of BN:ZnS(Ag) were fabricated by sintering commercial powders using FAST. The ceramics maintained luminescence and demonstrate the feasibility of using this technique to make materials for neutron detection. The major concern of this technique is translucency and contamination. While some of the

ceramics sintered with the N-C1 powders show improved translucency to the Scintacor screens; the process is difficult to repeat and challenging when incorporating BN. Refinement and development of the process may achieve the improved translucency.

The interrelated dependencies of temperature, dwell time, heating rate, and particle grain size need to be explored further. It is apparent the starting grain size is of great importance as shown by the difference in the ceramics sintered with N-C1 powders compared to the F-S1 powders. It was anticipated that the F-S1 powders would produce better transparency, but the most translucent samples were unexpectedly fabricated from N-C1 powders. Adjusting the dwell time or dwell temp with the smaller-grained powders may improve the sintering. Additionally, controlling the heating rate, as claimed by Chen, *et. al.*, may improve transparency.

The darkening in the ceramics poses a foreseeable drawback to using these ceramics as materials for neutron detection. The contamination affects transparency, is likely to change the expected energy transferred to ZnS, and could introduce new interactions with neutrons (such as scattering) that may need to be considered in the neutron signal. Contaminant concentration showed correlation to sintering temperature and dwell time and therefore could potentially be controlled through further optimization of the sintering profile. Other mitigation methods, such as changing the graphite products, creating a nonreactive barrier (i.e. coating the graphite with BN), or using molybdenum rather than graphite may decrease the contamination.

The FAST process unexpectedly proved temperamental and challenging to reproduce. Late in the fabrication process small changes in the test setup seemed to create large variability in the product. Fabrication with HUP may prove to be a more stable process.

The process also needs to develop better methods for mixing BN with the ZnS as

this impacts the quality of the ceramic. The powders were initially mixed by hand using mortar and pestle to lightly grind the powders together. This resulted in ceramics with noticeable heterogeneity. Subsequent trials mixed the powders via ball-milling. The process was specifically designed to provide light mixing so as not to introduce contaminants from the milling process and not to significantly reduce the grain sizes of the powders. The ball-milled powders improved the homogeneity of the ceramic, but not to the desired level. One method to improve homogeneity further might be mixing the powders as a slurry in deionized water rather than as dry powders. Boron could also be incorporated into the ceramic via other species of boron compounds. Pure boron offers many advantages over boron nitride, but trial ceramics of boron powder and ZnS resulted in very dark opaque ceramics even at low mass ratios. The elevated temperatures may cause the boron powder to form cubic crystals or react with the carbon to form boron carbide. Sintering with ultra-fine grains of boron may reduce the crystal growth resulting in a more transparent ceramic. Additional methods for combining ZnS and boron are discussed in Chapter 5.

The characterization of the ceramics discussed in this chapter provides insight into the sintering process and the results of the characterization was the basis for further development and investigation. Further characterization in Chapter 4 is based on the ceramic response to neutrons. The results of those experiments provide additional recommendations for future efforts.

Chapter 4

Neutron Experiments with Composite Ceramics and Phosphor Screens

The ceramics fabricated through the processes described in Chapter 3 were exposed to neutrons and gammas in a series of experiments to quantify the performance using a custom-designed apparatus to measure light from both sides of the ceramic. Similar experiments were conducted for the Scintacor screens to provide a baseline for comparison. Initial analysis of these measurements was focused on quantifying neutron count rate and light yield per neutron detected. The ratio of light collected from either side of the sample facilitated further analysis of components of light yield based on the mathematical models described in Chapter 2. Attempts to quantify these various components enabled a comparison of energy deposition to the MCNP6 models developed in Chapter 2.

4.1 Experimental Setup

The goal of the neutron experiments was to provide consistent light collection and neutron flux through the samples to facilitate comparison of event rates and light collected per event. This was accomplished by designing a custom test apparatus consisting of a sample testing box and a radiation enclosure. The sample testing box allowed for samples to be mounted in the same position relative to photosensors on either side of the sample thereby reducing systematic differences in light collection (described in greater detail in Section 4.1.3). The box was then placed in a uniform position relative to an AmBe neutron source within a radiation enclosure to recreate a constant neutron flux through the sample, as described in Section 4.1.2. By controlling the light collection and the environment relative to neutron transport around the sample, the differences in neutron detection between samples should be solely dependent on the cross-section of the capture isotopes, the isotopic content of the sample, and the light yield (defined as the number of photons escaping the sample for every neutron captured).

Another key component of the experimental setup was the data acquisition methodology (discussed in Section 4.1.4). This experiment used the same DAQ electronics from the SoLid experiment to leverage its neutron trigger. This trigger was specifically designed to record the unique neutron waveforms produced from the phosphor screen. By using this DAQ, it was assumed the composite ceramics would produce similar waveforms with adequate PSD to trigger event recording.

4.1.1 Source

The neutron experiments used a sealed $^{241}Am^{9}Be$ neutron source. Neutrons are the product of multiple interactions. First, the ^{241}Am decays to produce α particles. These

α particles then interact with the ^{9}Be causing it to decay. The 432 year half-life of Am-241 means the difference in activity is negligible and won't create any noticeable difference in neutron flux between measurements.

The energy of the neutron produced from this source is dependent on the energy of the α and the kinematics of the decay reactions. Americium-241 decays via equation (4.1), emitting an α with typical energies of 5.486 (85%), 5.443 (13%), or 5.388 (2%) MeV (the full spectrum is provided in Figure 4.1).

$$^{241}_{95}\text{Am} \rightarrow ^{237}_{93}\text{Np} + ^{4}_{2}\text{He} + \gamma + 5.64\ \text{MeV} \tag{4.1}$$

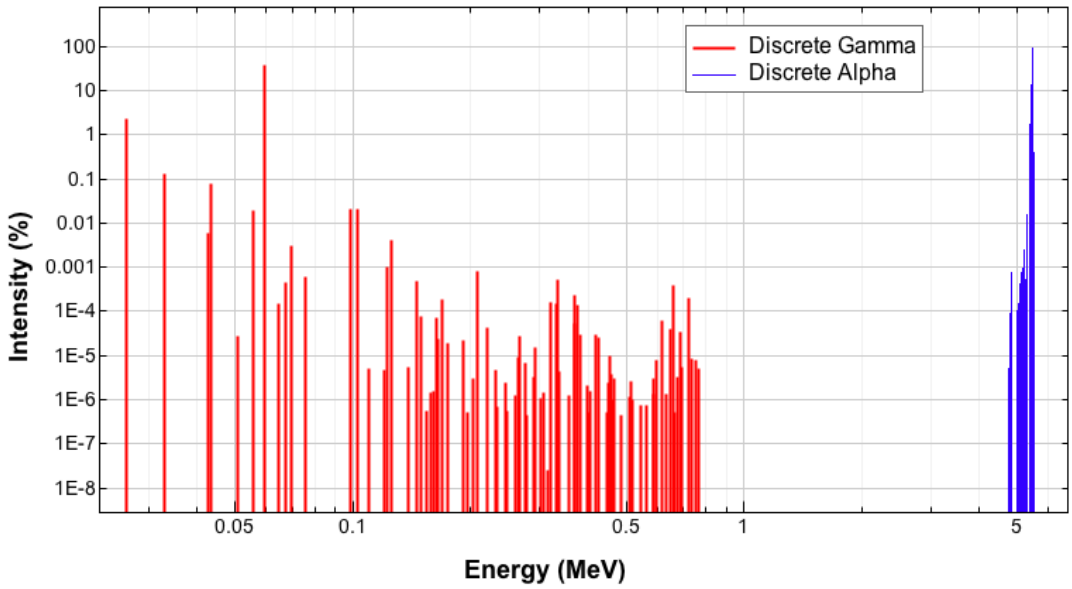

Figure 4.1: Gamma and alpha energy spectrum from Am-241. Figure produced from [43].

Because the source is comprised of small grains of americium oxide and a beryllium compound compressed together, not all the α energy is transferred to the ^{9}Be—similar to the problem of energy transfer discussed in Chapter 2. Thus, energy deposited in the ^{9}Be

has a continuous spectrum with maximums near the aforementioned energies [101,102].

Alpha particles with residual energy greater than 2.62 MeV overcome the Coulomb barrier and interact with the ^{9}Be nucleus. Interactions that lead to capture form a ^{13}C nucleus in an energetic state (based on the excess energy of the reaction), as shown in,

$$ {}^{9}_{4}\mathrm{Be} + {}^{4}_{2}\mathrm{He} \rightarrow {}^{13*}_{6}\mathrm{C}. \tag{4.2} $$

This excited ^{13}C then decays through emission of a neutron:

$$ \begin{aligned} {}^{13*}_{6}\mathrm{C} \rightarrow {}^{12}_{6}\mathrm{C} + {}^{1}_{0}n + \gamma\ (4.43\ \mathrm{MeV}) + 1.2\ \mathrm{MeV}\ 60\% \\ {}^{13*}_{6}\mathrm{C} \rightarrow {}^{12}_{6}\mathrm{C} + {}^{1}_{0}n + 5.6\ \mathrm{MeV}\ 40\%. \end{aligned} \tag{4.3} $$

The energy of the neutron emitted from these reactions is a combination of the Q value and the energy of the α from (4.1). This results in a neutron energy spectrum with an average between 4 and 5 MeV and a maximum up to 11 MeV.

In addition to neutrons, the Am-241 also produces gammas (see the gamma spectrum in Figure 4.1) as does the C-13 decay. These gammas can potentially cause scintillation from the samples or produce charge on the photosensors. To explore the possibility of gammas mimicking a neutron signal, additional experiments were conducted in the same test apparatus with a Co-60 gamma source. The Co-60 source produces gammas at energies of 1.17 and 1.33 MeV, which is greater than the spectrum of gammas produced from Am-241 decay, but less than the 4.43 MeV gamma produced from the C-13 decay.

$$
\begin{aligned}
{}^{60}_{27}\mathrm{Co} \rightarrow \beta^{-}\ (0.31\ \mathrm{MeV}) + {}^{60*}_{28}\mathrm{Ni} \rightarrow {}^{60}_{28}\mathrm{Ni} + \gamma\ (1.17\ \mathrm{MeV}) + \gamma\ (1.33\ \mathrm{MeV})\ 99.88\% \\
{}^{60}_{27}\mathrm{Co} \rightarrow \beta^{-}\ (1.48\ \mathrm{MeV}) + {}^{60*}_{28}\mathrm{Ni} \rightarrow {}^{60}_{28}\mathrm{Ni} + \gamma\ (1.33\ \mathrm{MeV})\ 0.12\%.
\end{aligned}
\tag{4.4}
$$

4.1.2 Radiation Enclosure

To try and recreate a uniform radiation field, the source and the sample testing box were placed in the same relative position within a radiation enclosure which reflected, moderated, and captured neutrons (see Figure 4.2). The shielding was made of 5 cm thick borated plastic and formed an 80 cm deep × 50 cm wide × 63 cm box resting atop a 10 cm thick optical table. The AmBe source remained in a 35 cm diameter and 15 cm tall cylindrical radiation enclosure of similar borated plastic with a removable plug on top to allow access. For neutron measurements, the light tight box rested atop the neutron housing positioned in the center of the radiation enclosure. With the plug removed, the source was placed on a platform to raise it 5 cm higher within the housing. An additional 5 cm of non-borated plastic was placed atop the light tight box to reflect neutrons back toward the sample.

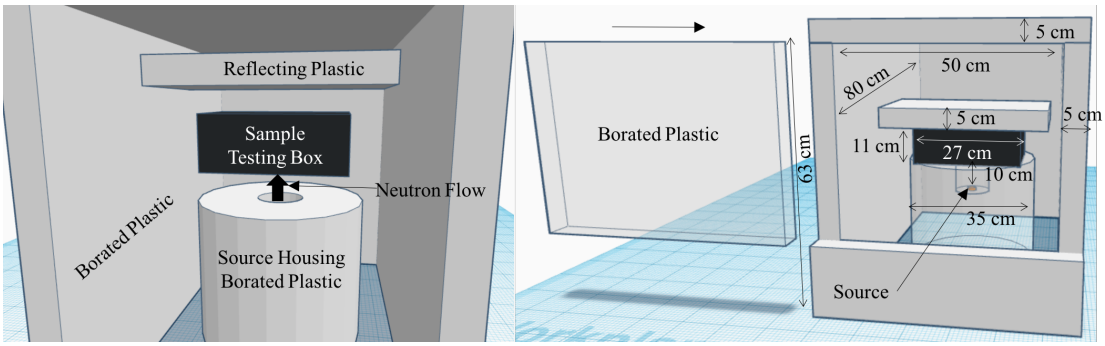

Figure 4.2: Radiation enclosure.

4.1.3 Sample Testing Box

The sample testing box was designed to provide a uniform mean of collecting light from both sides of a material. Samples were mounted in a 3-D printed sample holder in the center of a 29 × 16 × 11 cm light tight box made of 2 cm thick carbon fiber plates, as shown in Figure 4.3. The sample holder had 2 cm diameter ports on either side to allow light from the sample to escape in two directions. Light escaping from the sample was reflected within a 3-D printed hemisphere lined with Tyvek. At the end of each hemisphere was a SiPM to convert the light to an electronic signal (see Figure 4.4).

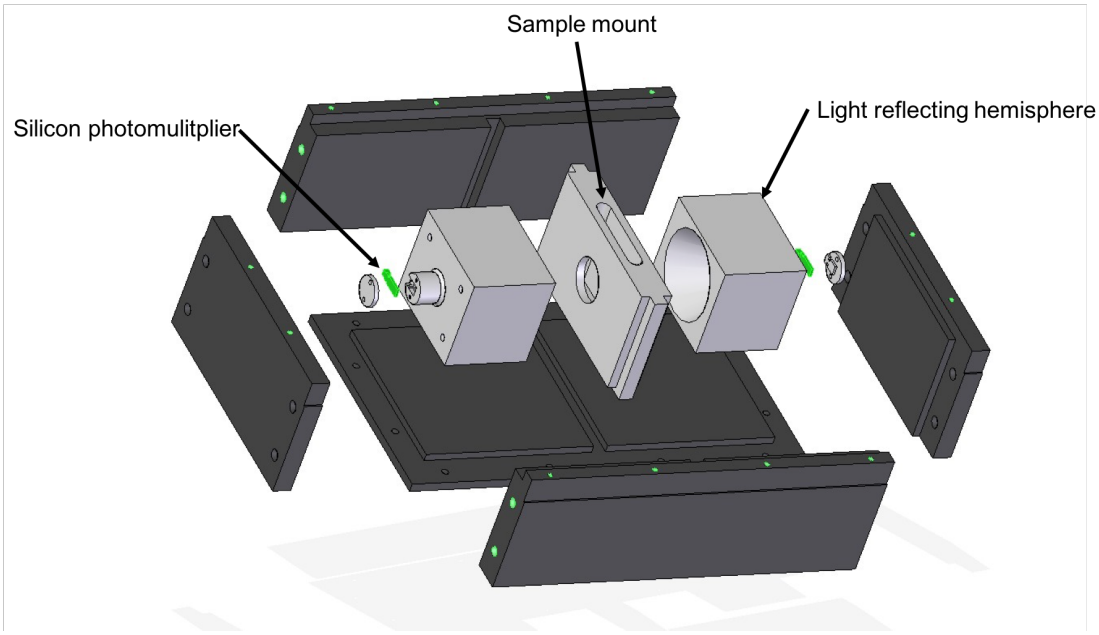

Figure 4.3: Light tight enclosure that mounts samples between two SiPMs.

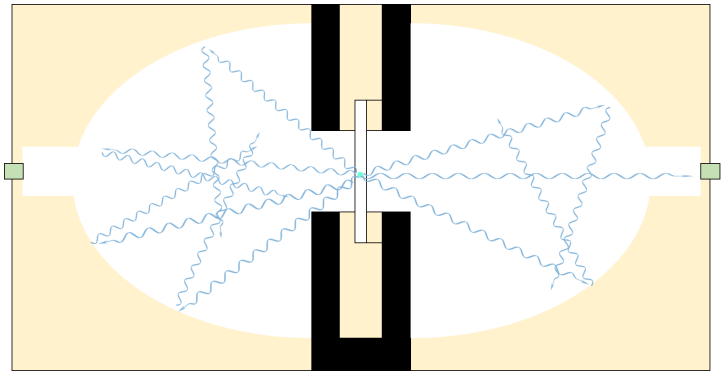

Figure 4.4: Light collection of samples mounted between two diffuse reflecting hemispheres that direct light to SiPMs.

The SiPMs operated at 50 V overvoltage resulting in a gain of $\sim 1.5 \times 10^6$ at 20°C. Any changes in gain related to fluctuating temperature was accounted for by measuring the temperature with sensors mounted on the DAQ board. Room Temperature was controlled using an air conditioning unit. The SiPMs have a peak conversion efficiency of $\sim 30\%$ at 450 nm making them well-suited for converting scintillated light from ZnS.

4.1.4 Data Acquisition

The data acquisition (DAQ) electronics used to collect the measurements was designed for the SoLid antineutrino experiment which enabled collection of signals on multiple channels from a single trigger event using a trigger designed to identify the neutron waveforms produced by the phosphor screens [42]. Signals were transferred from the SiPMs to this custom DAQ via micro-coax cables. In addition to receiving the signal from the SiPM, the DAQ also supplied the power to the SiPMs, monitored and adjusted the overvoltage based on the temperature, converted the signal from analog to digital, buffered signals, assessed the signals as to whether they meet the trigger requirements, and finally read the signals out to a computer (a detailed schematic of the buffer and

trigger functions of the DAQ can be found in [42]). A schematic of the setup is shown in Figure 4.5.

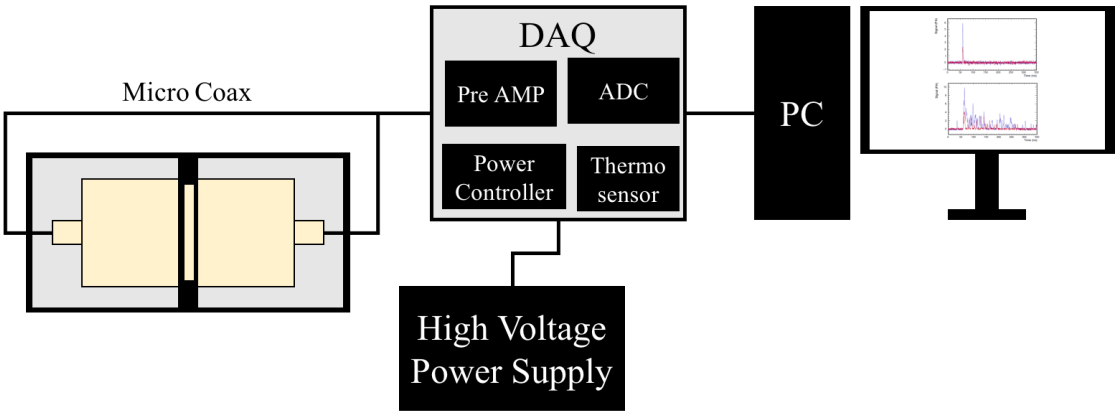

Figure 4.5: Schematic of DAQ.

The trigger designed for the SoLid experiment uses a running count of peaks (a local maximum above a prescribed threshold) within a time window based on common features seen in the neutron signals produced by the Scintacor screens. The trigger parameters for this experiment were 5 peaks (above 1.5 photon avalanches) within 6.4 μs (256 samples using a digital sampling rate of 40 MHz). This is a modification from the nominal values used by SoLid to account for the differences in light collection of the sample testing box that uses air coupling rather than the WSF used in SoLid. Figure 4.6 provides an illustration of the trigger using a sample waveform from the data. These parameters directly affect the data rate and data-set purity. The rate can be increased by decreasing the peak threshold, shortening the window, and/or decreasing the number of peaks at the expense of data-purity. The settings selected for these measurements represent a cursory attempt to balance the data rates with the data purity.

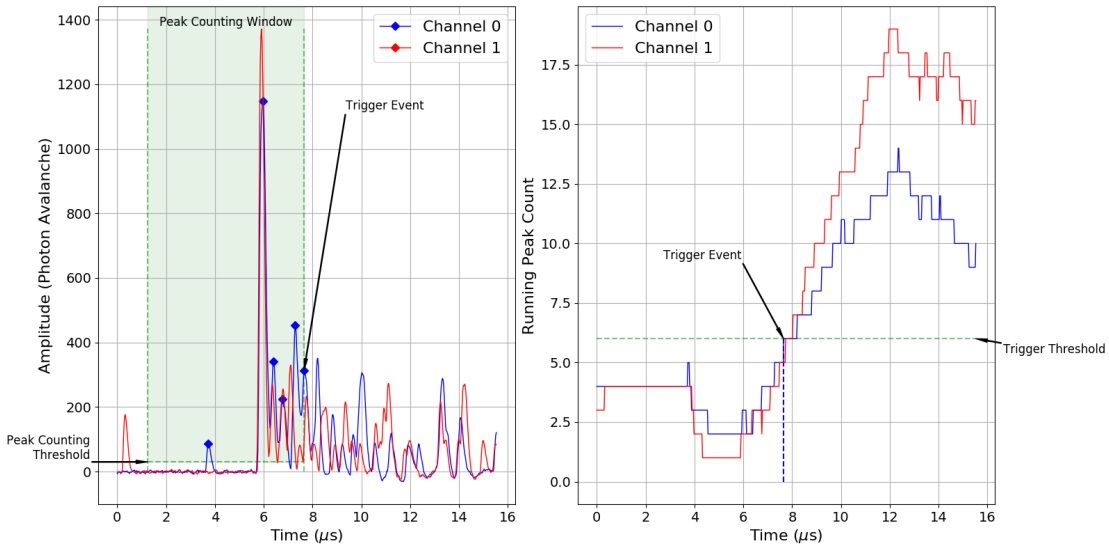

Figure 4.6: On the left is a sample waveform illustrating the trigger algorithm. Peaks are counted in both waveforms until the number of peaks on one channel exceeds the prescribed number of peaks (6 in this case) within 6.4 μs. A peak is counted if the signal exceeds a threshold and is a local maximum. On the right is the trigger variable which is a running tally of the peaks within the previous 6.4 μs. When the trigger variable exceeds 6, the signal is recorded.

4.1.5 Experimental Details

Selected ceramics were exposed to a neutron source to confirm whether composite ceramics could detect neutrons and to determine if parameters such as boron content, thickness, or ZnS batch affected the response. The results of these measurements were compared to measurements of the Scintacor screen which provides a thoroughly studied reference material. Additional experiments were conducted with a gamma source to confirm events classified as neutrons are not the product of gammas interacting with the samples.

Measurements were taken of samples without a source, with an AmBe source, and with a Co-60 source. Table 4.1 provides a summary of those samples tested.

Table 4.1: Summary of Tested Samples

Sample Designation	Content	Mass Ratio	Sinter Temperature (°C)	Sinter Dwell Time (min)	Thickness (μm)
Scintacor	^{6}LiF:ZnS(Ag)	1:2	N/A	N/A	290
160808-2	ZnS(Ag) (N-C1)	N/A	950	30	1994
160816-3	BN:ZnS(Ag) (N-C1)	1:87	950	60	1895
160816-4	BN:ZnS(Ag) (N-C1)	1:87	950	90	640
170615-3A	ZnS(Ag) (F-S1)	N/A	950	30	540
170616-6A	BN:ZnS(Ag) (F-S1)	1:87	950	30	590
170621-1B	BN:ZnS(Ag) (F-S1)	1:22	950	30	1070

Details of the measurements are presented in Table 4.2. Attempts were made to take as much data in each test configuration, but the availability of the source constrained the duration of some of the experiments. The trigger settings were adjusted to find the conditions that provided sufficient statistics and kept the background rate from saturating the DAQ. The nominal trigger was based on 5 peaks, but it was found that the Scintacor screens produced so many events that the trigger was increased to 6 to lower the total rate. This improved the purity of the signal, but also complicated the comparison with measurements taken with a 5-peak trigger. Presumably data taken with the 6-peak trigger will omit low-amplitude events that would have been captured with a 5-peak trigger which effects the rate of events. However, it is not certain these low-amplitude events are even discernible from the background. To better understand the differences in the selected triggers, a few experiments were conducted to explore differences in event

population with different triggers.

Table 4.2: Duration of Neutron Experiments

Sample	Peaks	Duration of Experiment (min)		
		No Source	AmBe	Co-60
None	5	10		
	6	10		
	7	10		
Scintacor	5	10	10	10
	6	960	180,10	10
	7	10		10
160808-2	5	1020,10	60,60	10
	6		10	
160816-3	5	330	150	
160816-4	5	900	120	
170615-3A	5	840	100	
170616-6A	5	900	150	
170621-1B	5	1020	180,10	
	6		10	10

Experiments with the Co-60 source were aimed at determining if the gammas produced from the AmBe source create an appreciable number of false-positive events that are counted as neutrons. As such, only a few experiments were conducted with selected samples to explore the influence of the gammas on the rate of neutron signals. Also of note is the high rate of phosphorescence that can contribute to false-positives. To reduce the rate of false-positives from phosphorescence, the samples were stored in light-tight storage containers and data recording was delayed as much as 30 minutes after the sample was sealed in the sample testing box.

4.2 Results and Analysis

After measurements were taken, analysis of the data was conducted to assess the neutron count rate, the light yield distribution, and the waveform characteristics associated with PSD. Additional analysis used the ratios of light emitted from either side of the sample to try and quantify factors related to light yield; specifically, the attenuation, the depth, and the energy deposition for each event.

4.2.1 Neutron Count Rate

The neutron count rate was estimated by counting events with characteristics consistent with a neutron event. As described in Chapter 1, neutron events are expected to produce waveforms with an intense peak and a long decay, as shown in Figure 4.7. The SoLid DAQ is effective at triggering on these neutron events and eliminating events that are characteristic of gammas (i.e. single intense peaks). The remaining background events are characterized by many low amplitude peaks without a noticeable pulse or decaying intensity.

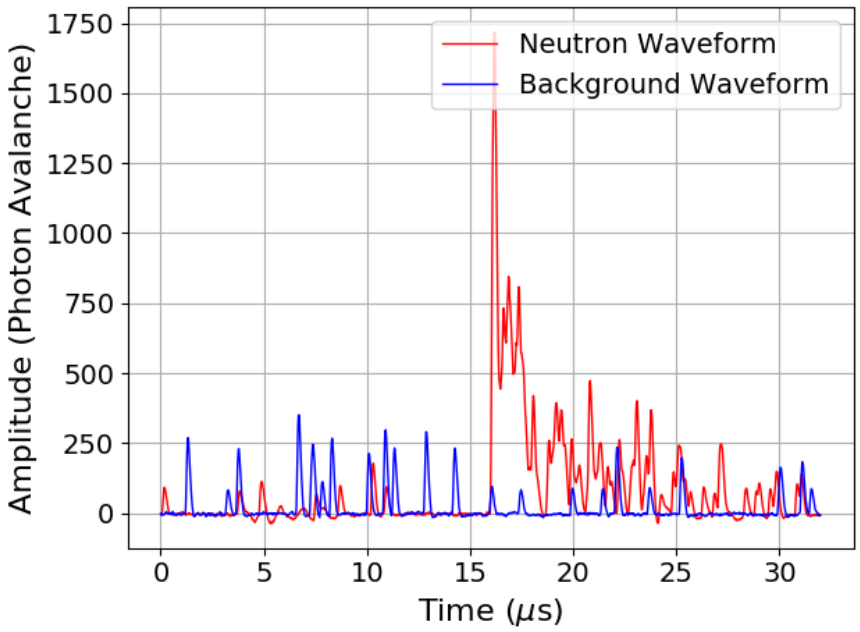

Figure 4.7: Sample waveforms illustrating the difference between a neutron event and background.

One method of distinguishing the neutron events from this background is to compare the summed signal (or integral) and the maximum amplitude. Figures 4.8 - 4.11 show the correlated summed signals for both channels and reveal an increase in events with high signal sums in the presence of the AmBe source (presumably neutrons). The maximum amplitude distributions show a similar trend (not shown).

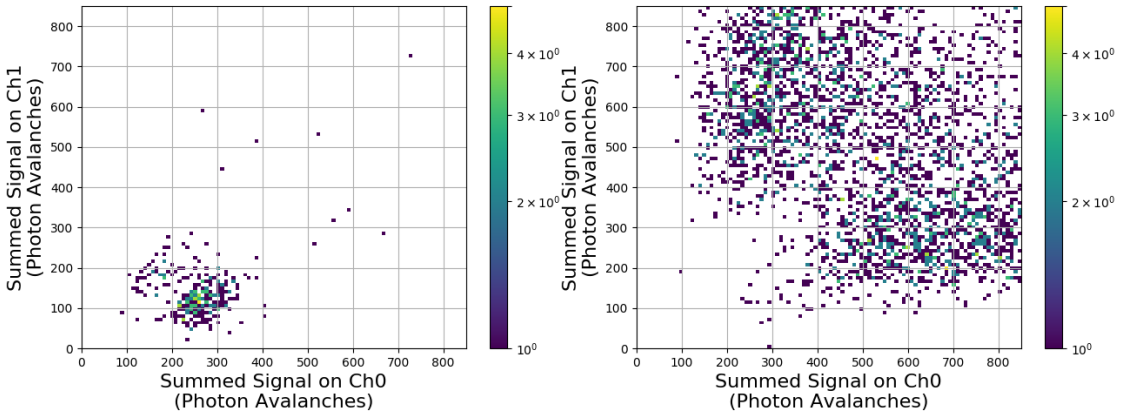

(a) No Source (b) With AmBe Source

Figure 4.8: Summed signal from each SiPM channel for neutron measurements with the Scintacor screen (a) without the source and (b) with the AmBe source.

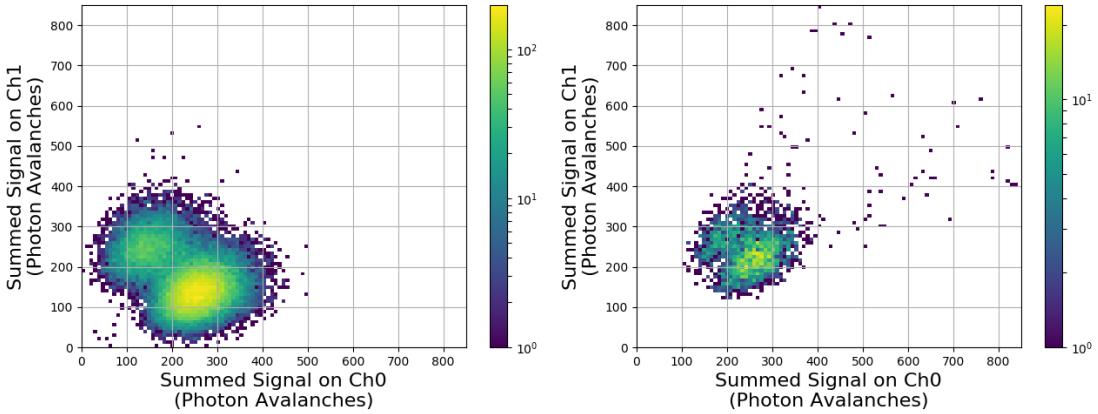

(a) No Source (b) With AmBe Source

Figure 4.9: Summed signal from each SiPM channel for neutron measurements with the 160808-2 ZnS(Ag) ceramic (a) without the source and (b) with the AmBe source.

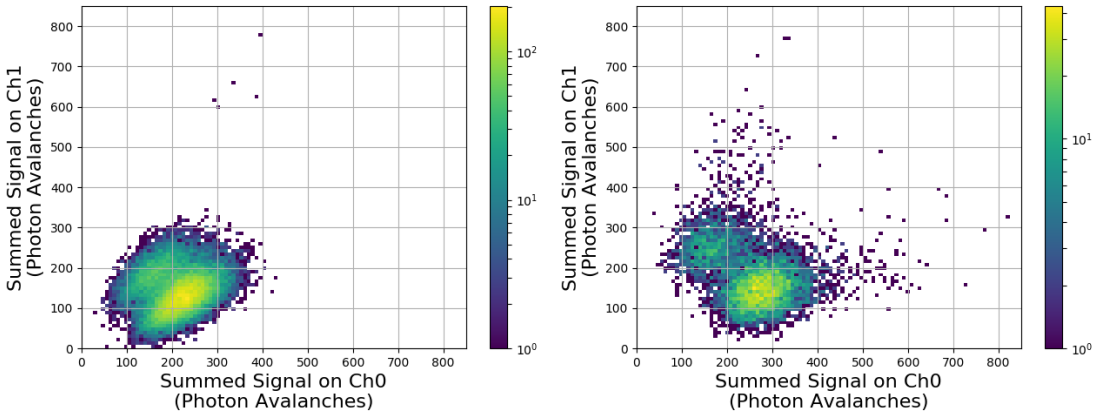

(a) No Source (b) With AmBe Source

Figure 4.10: Summed signal from each SiPM channel for neutron measurements with the 160816-4 BN:ZnS(Ag) ceramic (a) without the source and (b) with the AmBe source.

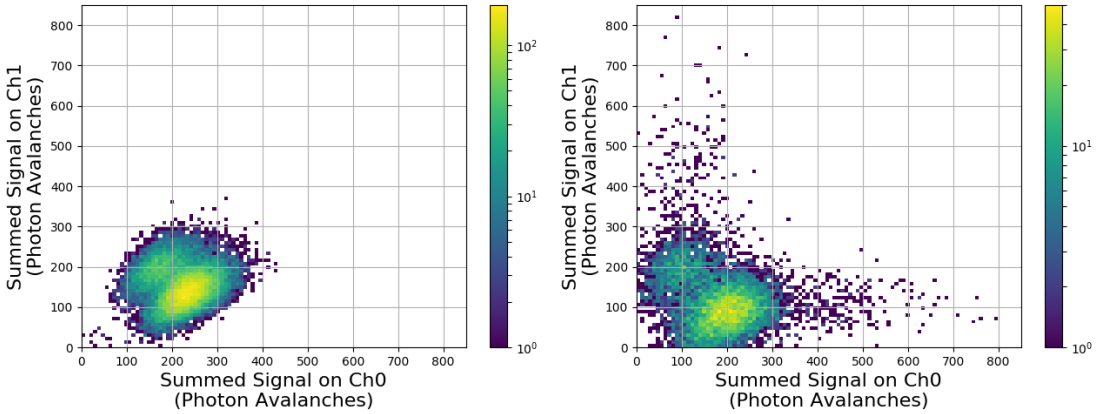

(a) No Source (b) With AmBe Source

Figure 4.11: Summed signal from each SiPM channel for neutron measurements with the 170616-6A BN:ZnS(Ag) ceramic (a) without the source and (b) with the AmBe source.

Using these distributions, an event was classified as a neutron if it exceeded a summed signal of 400 PA or a maximum amplitude of 10 PA on either channel. Additionally, events were classified as a neutron if the summed signal or maximum amplitude exceeded a simple sloped threshold. Figure 4.12 shows these thresholds overlaid on the

summed signal distribution.

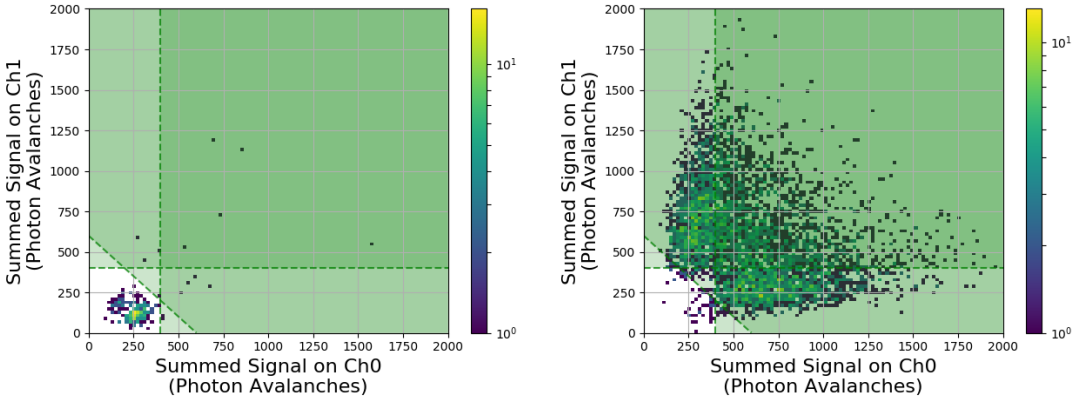

(a) Without Source (b) With AmBe Source

Figure 4.12: Illustration of neutron cuts on summed signal distributions of events generated from the Scintacor screen. Three cuts were made on each distribution. An event is counted as a neutron if it exceeds any of the cuts.

The neutron count rate based on these cuts is provided in Table 4.3. Comparison of these rates show a significant increase in events with high integrals or maximum amplitudes in the presence of the AmBe source. The Scintacor screen showed the most significant increase. Unexpectedly, the ceramic without any BN (160808-2) had the next highest rate. Although this ceramic had relatively few high-integral events, the duration of the experiments was one of the shortest. As discussed above, this unexpectedly high rate could be due to a higher rate of gamma interaction due to the thickness or the neutron causing carbon to recoil.

The composite ceramics were expected to have rates related to their thickness, mass ratio, and potentially the batch of ZnS. Comparing event rates for ceramics 160816-3 and 160816-4 should show a higher neutron event rate in the thicker 160816-3 ceramic. There is about a 20% increase in the rate of events for the 160816-3 ceramic. Comparing event rates for ceramics 170616-6A and 170621-1B should show a higher neutron

event rate in the thicker and higher-boron-content 170621-1B ceramic. This ceramic, however, had a $\sim$ 30% lower event rate than the 170616-6A ceramic. The unexpectedly lower rate could be a result of a lower light yield resulting in the preponderance of neutron events falling below the neutron cuts.

Table 4.3: Neutron Count Rates

Sample	Thickness (μm)	Source	Rate of Neutron Events (Hz)
Scintacor (Reference)	290	AmBe	0.441(6)
		No Source	0.0003(1)
160808-2 ZnS(Ag) NC-1	1994	AmBe	0.072(5)
		No Source	0.0055(3)
160816-3 BN:ZnS(Ag) NC-1 1:87	1895	AmBe	0.067(3)
		No Source	0.0024(3)
160816-4 BN:ZnS(Ag) NC-1 1:87	640	AmBe	0.053(3)
		No Source	0.0009(1)
170615-3A ZnS(Ag) FS-1	540	AmBe	0.0040(8)
		No Source	0.0008(1)
170616-6A BN:ZnS(Ag) FS-1 1:87	590	AmBe	0.029(2)
		No Source	0.0009(1)
170621-1B BN:ZnS(Ag) FS-1 1:22	1070	AmBe	0.021(1)
		No Source	0.0013(1)

Figure 4.13 shows the neutron count rates as they relate to the sample thickness and the neutron attenuation length. In theory, the neutron count rate should increase with ^{10}B (or ^{6}Li) content that is controlled by the thickness and mass ratio (ignoring the effects of signal amplitude). Figure 4.13a shows a modestly increasing count rate (ignoring the point on the far left associated with the Scintacor sample) with increasing thickness of the ceramics, however, this trend cannot be related to an increase in ^{10}B content as the mass ratios in some cases decrease the ^{10}B content (one of the thickest samples has no ^{10}B content). A similar trend can be seen in the measurements without

the AmBe source. This suggests the increasing count rate associated with increasing thickness may be related to either phosphorescence or an increased reaction rate with gammas (the response of the samples to gammas is briefly discussed at the end of this section).

Figure 4.13b shows the neutron count rate as it relates to the neutron attenuation length (determined by the cross section and estimated isotopic density) and is independent of thickness. The expected trend of increasing count rate is not apparent, unless the unexpectedly high rate of 160808-2 ZnS(Ag) ceramic and the unexpectedly low rate of the of the 170621-1B BN:ZnS(Ag) (1:22 mass ratio) ceramic are discounted.

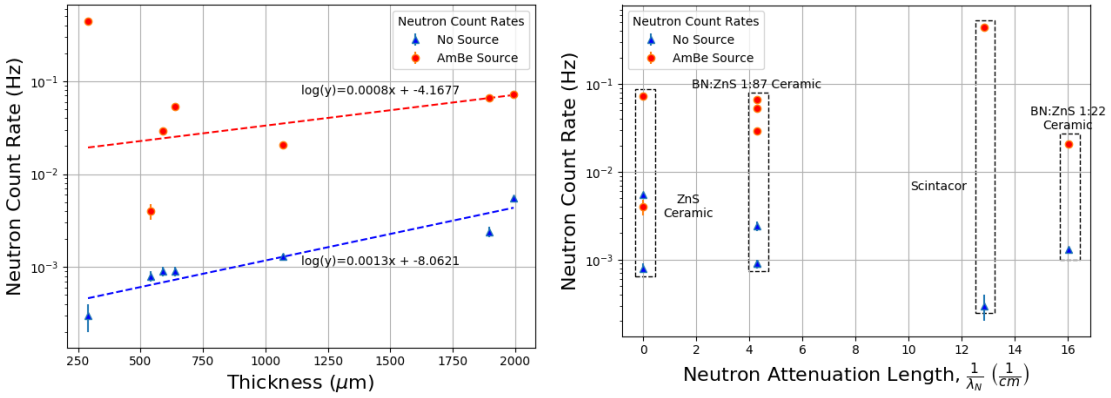

(a) Relative to sample thickness (b) Relative to the neutron attenuation length

Figure 4.13: Relation of neutron count rate to (a) sample thickness and (b) neutron attenuation length. The neutron attenuation length was calculated based on estimates of the enrichment, mass ratios, and neutron cross-sections for each sample.

It is unclear what caused the greater-than-expected increase in high PA events in the pure ZnS ceramic. It may have been due to residual phosphorescence, but additional tests that kept the ceramic in the dark for great periods of time (>1 hour) confirm these results. Alternatively, these signals may be due to the carbon deposited in the ceramic from the sintering process. It might be possible that these carbon recoil from interac-

tions with neutrons thereby producing the scintillation in ZnS. Another explanation may be related to the thickness. This ceramic is nearly 2 mm thick and may be more susceptible to gamma-induced scintillation. Experiments to quantify the gamma response of the samples were conducted to explore this possibility. Figure 4.14 shows the results of measurements comparing the AmBe source measurements for the 160808-2 ZnS ceramic with the Co-60 measurements. The Co-60 measurements show a modest increase in high PA events but not as significant as the events observed when exposed to the AmBe source. These measurements suggest there is no significant response to gammas of 1.17 and 1.33 MeV energies. These measurements provide some evidence that gammas are not the source of the false-positives, but this hypothesis cannot be conclusively rejected based on these measurements. The AmBe source produces gammas with different energies (gammas less than 1 MeV and another at 4.43 MeV) that might have different reaction rates or deposit energy in a manner that produces the false-positives. The <1 MeV gammas could have a higher interaction rate than the Co-60 gammas or the false-positives could be due to the 4.43 MeV gammas that deposit more energy than the Co-60 gammas.

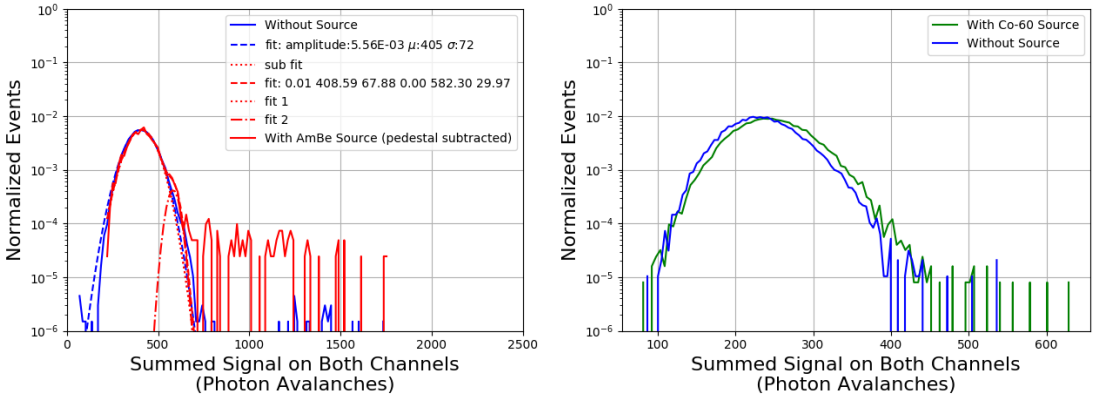

(a) AmBe Source

(b) Co-60 Source

Figure 4.14: Comparison of summed signal distributions for the 160808-2 ZnS ceramic when exposed to the (a) AmBe and (b) Co-60 sources.

The measurements of the signals produced in the presence of the AmBe source suggest the composite ceramics scintillate in the presence of neutrons. The next two sections explore the properties of that signal as it relates to characteristics of neutron detection.

4.2.2 Waveform Analysis and PSD

A significant aspect of neutron detection using the phosphor screens is the PSD that allows for discrimination of the signal from background. For the ceramics to be viable for neutron detection, the waveforms produced from neutron interactions must retain the PSD properties comparable to that of the phosphor screens. Two methods were used to quantify and compare the PSD. First, the time decay constant of the average waveforms was compared to show the difference between the waveforms and the background. Second, the separation of the summed signal distributions for the neutron and background events was quantified as a figure of merit (FOM).

Figure 4.15 shows random waveforms sampled from the background measurements and the source measurements. Each waveform classified as a neutron was realigned such that the initial pulse aligned with one another. The average waveform was calculated from these realigned waveforms. This process was then repeated for waveforms classified as background.

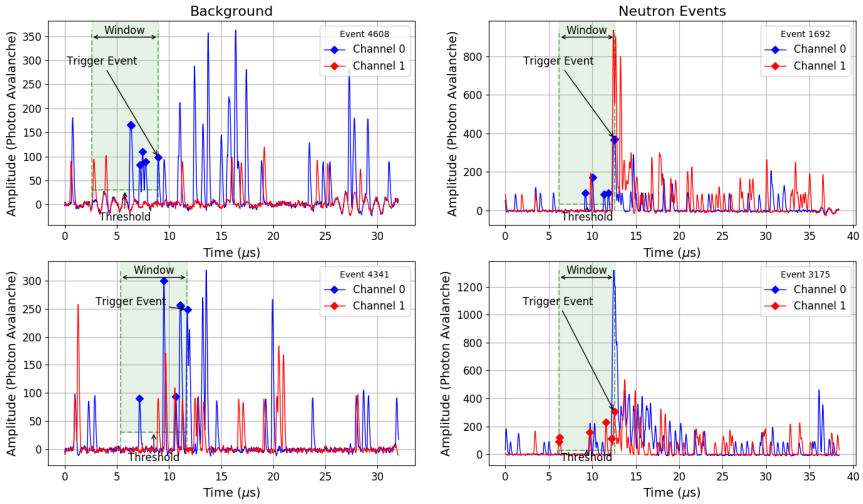

(a) Waveforms from the Scintacor phosphor screen.

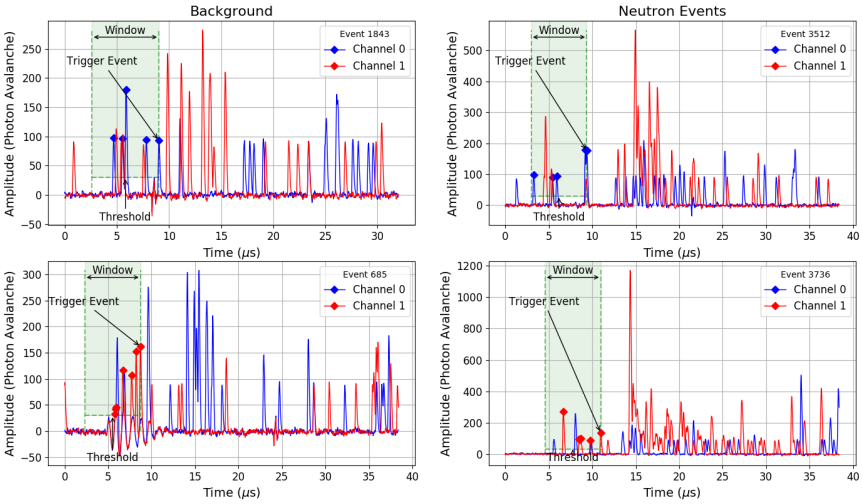

(b) Waveforms from the 160816-4 ceramic.

Figure 4.15: Random waveforms from the (a) Scintacor phosphor screen and (b) the 160816-4 ceramic with and without the AmBe source.

The average waveforms of events classified as neutrons and background are presented in Figure 4.16 for selected samples. The shaded region of each waveform is ± one standard deviation from the average. These distributions provide a representation of the similarity or dissimilarity between neutron and background events. A double exponential decay based on [50] was used to fit the average waveforms,

$$I = I_0 e^{\frac{-t}{\lambda_0}} + I_1 e^{\frac{-t}{\lambda_1}} + C. \tag{4.5}$$

These fits illustrate two decay mechanisms for the neutron waveforms and only one decay mechanism for the background. Each neutron waveform has a time constant of ~120 ns similar to the time constant of the background waveform. This fast decay constant is likely a measurement of the response of the electronics and not the true decay constant of the scintillation process. The second, longer decay (about 2 μs) seen in the fits of the neutron events is not limited by the sampling rate of the electronics and provides an estimate of the longer decay process. This delayed emission is likely due to the delayed release of charge carriers from trap states or greater migration of charged carriers caused by the high ionization density described in Chapter 1.

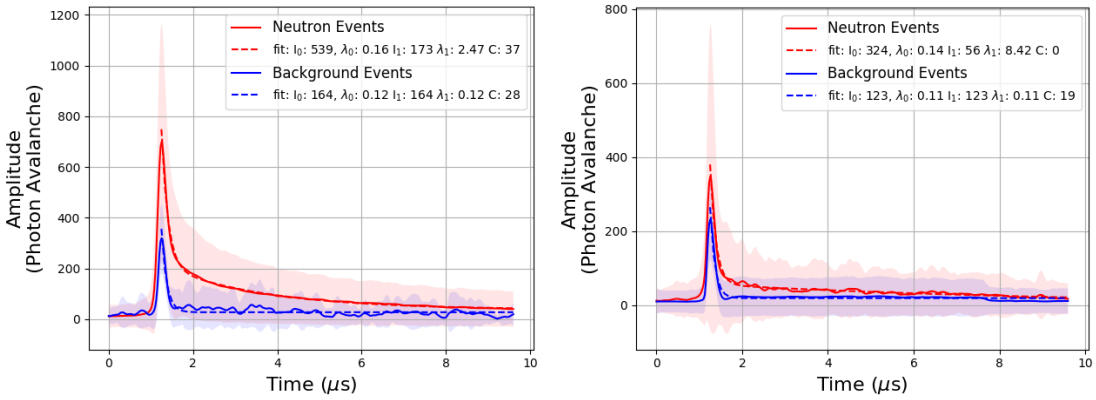

(a) Scintacor

(b) 160816-4

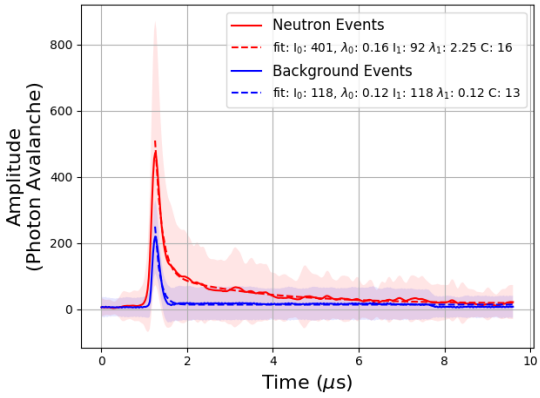

(c) 170616-6A

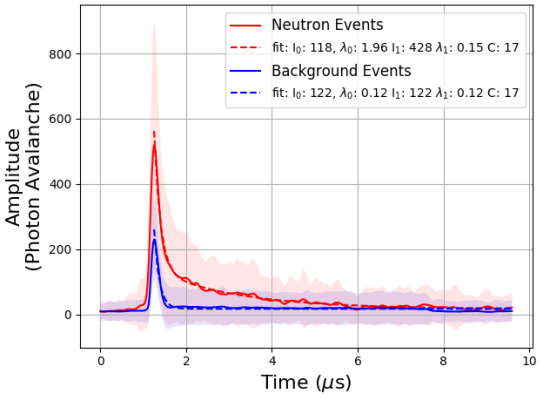

(d) 170621-1B

Figure 4.16: Average waveforms of events identified as neutrons and background for (a) the Scintacor screen, (b) the 160816-4 BN:ZnS(Ag) ceramic with NC-1 powder, (c) the 170616-6A BN:ZnS(Ag) ceramic with FS-1 powder, and (d) the 170621-1B BN:ZnS(Ag) ceramic with FS-1 powder in a 1:22 ratio. These waveforms are averaged from only one SiPM channel where the event exceeded the trigger requirements during exposure to the AmBe source. A double exponential decay was used to fit each waveform. The units of the fit parameters are photon avalanches for intensity (I_0 and I_1) and μs for the time constants (λ_0 and λ_1).

The relative intensities of the two exponentials used to fit the waveform provide some figure-of-merit (FOM) of the PSD, as shown in Table 4.4. Based on these relative intensities, the ceramics demonstrate similar discrimination as the Scintacor screens.

Table 4.4: Relative Intensity of Exponential Fits $\left(\frac{I_{\text{long}}}{I_{\text{short}}}\right)$

Sample	$\left(\frac{I_{\text{long}}}{I_{\text{short}}}\right)$
Scintacor (Reference)	0.32
160816-4 BN:ZnS(Ag) NC-1 1:87	0.17
170616-6A BN:ZnS(Ag) FS-1 1:87	0.23
170621-1B BN:ZnS(Ag) FS-1 1:22	0.28

A more traditional means of assessing PSD is using a FOM based on waveform characteristics such as the summed signal. The FOM is a measure of how well separated the background distribution is from the neutron distribution. As shown in Figures 4.17-4.19, the FOM of merit was calculated by dividing the separation (the difference between the mean values) by the sum of the FWHM [103]. To isolate the neutron distribution from the background, the background distributions were subtracted from the AmBe distribution leaving some statistical distribution representing the neutron events. A Gaussian fit was used to quantify the variation and mean in each distribution, although the neutron distribution most likely follows some other distribution. A discussion of noticeable features in each distribution is followed by Table 4.5 which summarizes the FOM analysis.

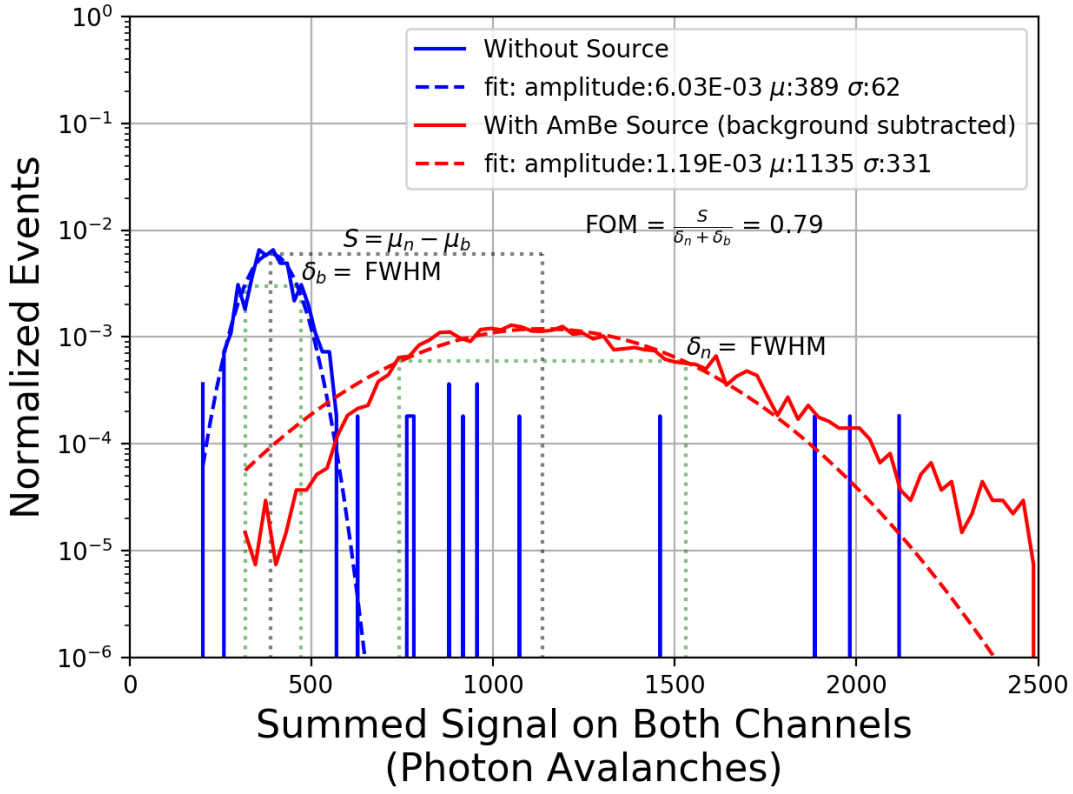

Figure 4.17: Summed signal from both channels for neutron measurements taken with the Scintacor screen. It is apparent from these measurements that there is a substantial difference in the amount of light collected from the Scintacor screen in the presence of the AmBe source.

An increase in higher sum events in the presence of the source is apparent, especially for the Scintacor sample (Figure 4.17). The ceramics did not produce the same prevalent response to the AmBe source; however, a change in the distribution resulting from the AmBe source is still discernible. Figure 4.18 shows the response of the ceramics made with the NC-1 powders. Each ceramic shows a modest increase in high integral events and a slight overall shift in the distribution to higher integrals. As discussed in a previous section, this increase is expected for the ceramics made with BN but not for the pure ZnS ceramic.

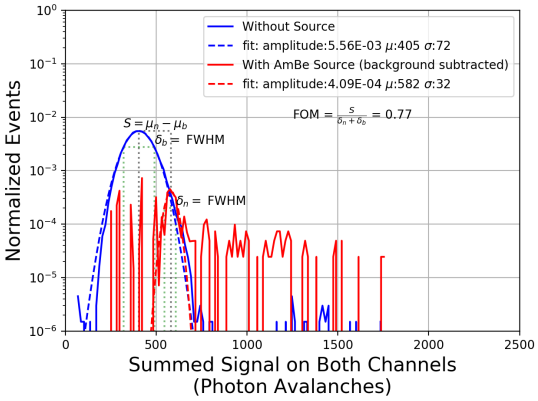

(a) 160808-2 ZnS(Ag) ceramic

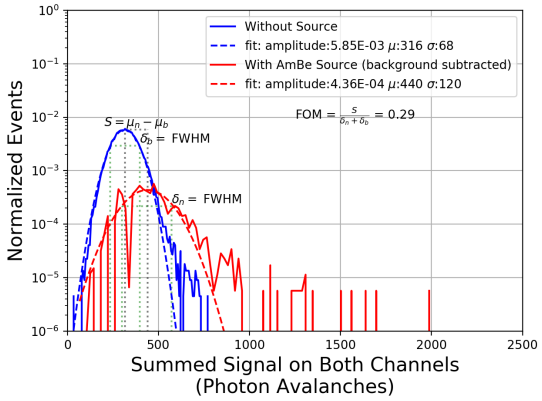

(b) 160816-3 BN:ZnS(Ag) ceramic, 1:87 Thick

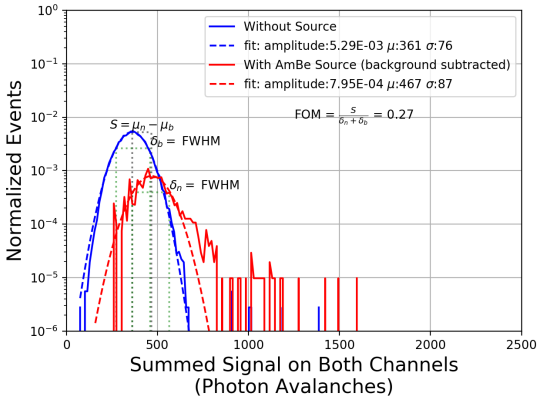

(c) 160816-4 BN:ZnS(Ag) ceramic, 1:87 Thin

Figure 4.18: Summed signal from both channels for neutron measurements taken with ceramics made from Phosphor Technology NC-1 ZnS(Ag) powders. (a) Shows some change in the amount of light collected in the presence of the AmBe source when the ceramic has no neutron sensitive material. (b) and (c) demonstrate how the response of the ceramics changes when BN is added to the ceramic.

Similar results are seen in the ceramics made with FS-1 powders, shown in Figure 4.19. Contrary to the NC-1 ceramics, the ceramic without any BN had, as expected, a negligible increase in high-integral events in the presence of the AmBe source. Both ceramics are expected to have similar carbon contamination, but this ceramic is nearly 4 times thinner than the comparable 160808-2 ceramic and may have some correlation in the difference of events if the events are indeed gamma-induced. The 170616-6A and

170621-1B ceramics have similar distributions to the comparable NC-1 ceramics made with BN. These two ceramics have differing amounts of BN suggesting the 170616-6A ceramic would have more events but with higher amplitudes/integrals. This effect is nearly imperceptible from these distributions except for the slight increase in events between 500 and 750 PA seen in Figure 4.19c compared to Figure 4.19b.

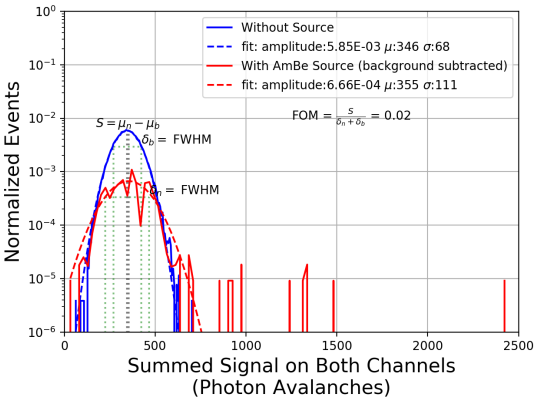

(a) 170615-3A ZnS(Ag) ceramic

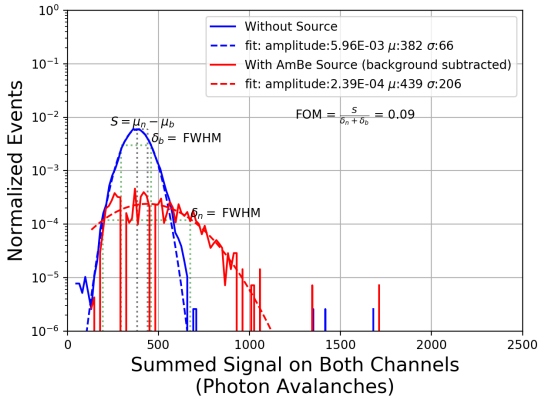

(b) 170616-6A BN:ZnS(Ag) ceramic, 1:87

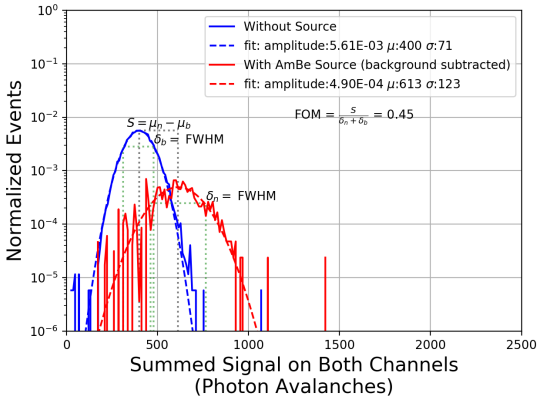

(c) 170621-1B BN:ZnS(Ag) ceramic, 1:22

Figure 4.19: Summed signal from both channels for neutron measurements taken with ceramics made from Phosphor Technology FS-1 ZnS(Ag) powders. (a) Shows little change in the amount of light collected in the presence of the AmBe source when the ceramic has no neutron sensitive material. (b) and (c) demonstrate how the response of the ceramics changes when BN is added to the ceramic in different mass ratios.

Table 4.5 presents the FOM values used to measure the separation of the background and signal distributions for each of the materials measured. These FOM are representative of the degree of PSD in the material, similar to the method to compare the intensities of the long and short components of the average waveforms shown in Table 4.4. The FOM method in Table 4.5 shows greater percent difference between the Scintacor screen and all the ceramics than the average waveform analysis in Table 4.4.

Table 4.5: PSD FOM from Summed Signal Distributions

Sample	FOM
Scintacor (Reference)	0.79
160808-2 ZnS(Ag) NC-1	0.77
160816-3 BN:ZnS(Ag) NC-1 1:87	0.29
160816-4 BN:ZnS(Ag) NC-1 1:87	0.27
170615-3A ZnS(Ag) FS-1	0.02
170616-6A BN:ZnS(Ag) FS-1 1:87	0.09
170621-1B BN:ZnS(Ag) FS-1 1:22	0.45

4.2.3 Light Yield Per Neutron Event

The last performance factor analyzed was light yield per neutron captured. This was estimated using the mean of the fit and calculating the mean of the summed signal for events classified as neutrons. Results of these calculations are presented in Table 4.6.

Table 4.6: Average Light Yield for Neutron Events with AmBe Source

Sample	Gaussian Fit μ (PA)	σ	Average of Classified Neutrons (PA)	σ
Scintacor	1135	331	1191	352
160816-3 (BN:ZnS(Ag) NC-1 1:87)	440	120	465	136
160816-4 (BN:ZnS(Ag) NC-1 1:87)	467	87	438	96
170616-6A (BN:ZnS(Ag) FS-1 1:87)	439	206	303	97
170621-1B (BN:ZnS(Ag) FS-1 1:22)	613	123	373	114

These methods resulted in values within about 5% of each other for the Scintacor screens and the NC-1 ceramics and about 40% difference in values for the FS-1 ceramics. The ceramics had a mean value of approximately 440 PA whereas the Scintacor screen had a mean value about 160% greater than the ceramics. The increased signal in the Scintacor screen was accompanied by greater deviation from the mean. Distributions of the summed integrals from neutron events of the Scintacor screen and a representative ceramic are presented in Figure 4.20 to illustrate the spread in light yield.

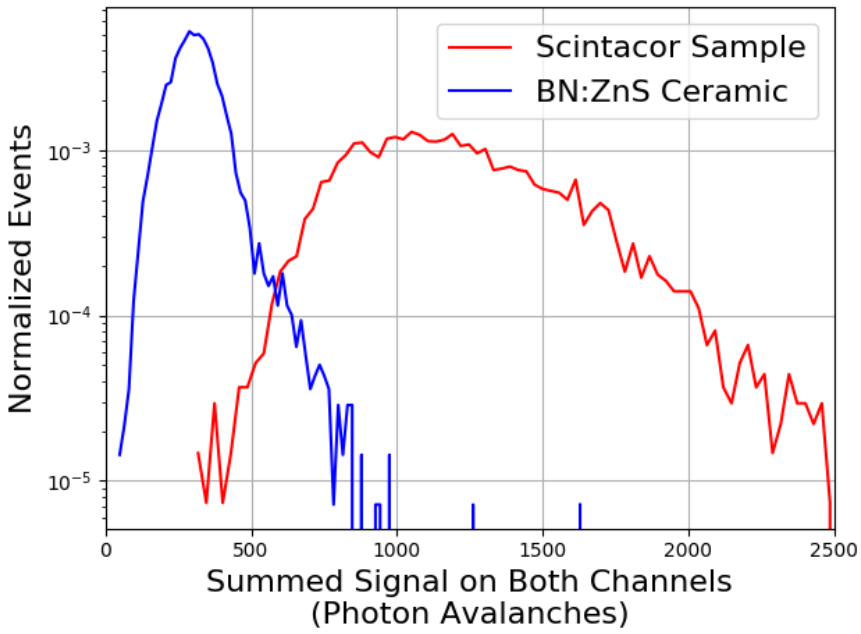

Figure 4.20: Summed signal from both channels for neutron events for the Scintacor sample and the 170616-6A BN:ZnS(Ag) ceramic with FS-1 powder.

The light yield of the ceramics was not as intense as predicted in Chapter 2; however, this analysis along with the neutron count rate and PSD confirms that the composite ceramics scintillate in the presence of neutrons and the waveform of light emitted has a shape sufficiently different from the background to be classified as a neutron. Although the light yield was less-than expected, the shapes of the distributions of light yield shown in Figure 4.20 do show some correlation to the models of energy deposition developed in Chapter 2. Figure 4.21 shows an overlay of the normalized light yield distributions and the energy deposition models to demonstrate the similarities. In particular, the relative variation in the distributions confirms the prediction of the energy deposition models.

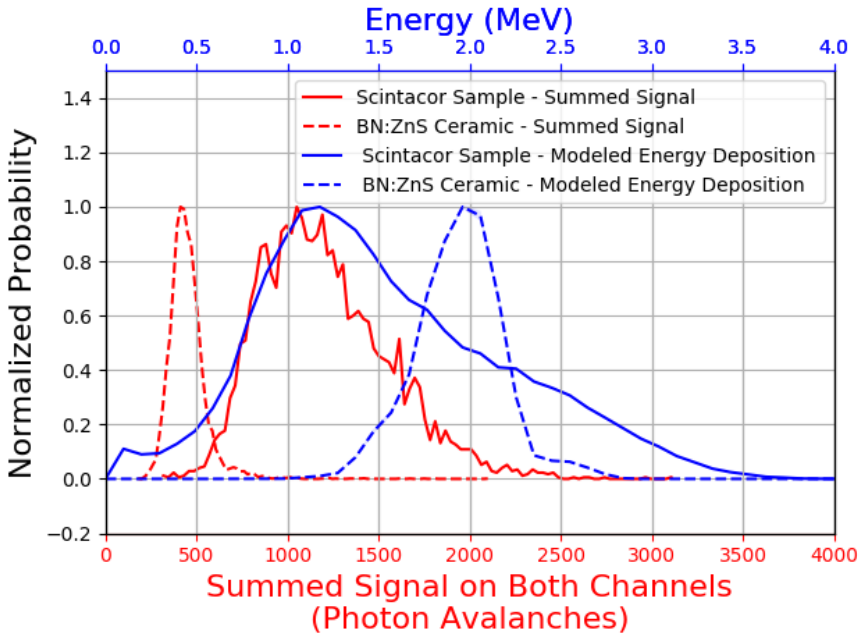

Figure 4.21: Comparison of energy deposition models to the summed signal from the phosphor screen and ceramic.

The models suggest the distribution of the ceramics should have a mean light yield greater than that of the Scintacor screen. The reduction in light yield could be from increased attenuation, degradation of the scintillation efficiency, or some other overlooked phenomenon. In Chapter 2, light yield was introduced as the combination of energy released per neutron capture, energy deposition in ZnS, scintillation efficiency of ZnS, attenuation of light as it escapes the sample, and the efficiency to collect light and convert it to a signal. These many factors make it difficult to isolate a single cause for the reduced emission. Additional analysis was conducted to explore these factors related to light yield.

4.2.4 Energy Deposition Comparison

The mathematical model for light yield developed in Chapter 2 was used to convert the summed signal data to an energy deposition distribution. This energy deposition distribution was then compared to the predictive models to identify factors that may have contributed to the reduced light yield. Parameters such as scintillation efficiency and attenuation were estimated and then adjusted to fit the two models. Attenuation was estimated by comparing the ratio of signals from each channel for events on the boundaries and compared to the attenuation models developed in Chapter 2. This attenuation estimate and the ratio of intensities was then used to estimate the depth of each event within the sample. Finally, these estimates were used with an estimate of the scintillation efficiency to derive the energy deposition based on the total light emitted for each event. This estimate was then compared to the energy deposition models derived in Chapter 2.

Attenuation

Attenuation of light was likely to be the prime cause for the reduced light yield despite the anticipated increase of transparency due to sintering. Attempts to measure attenuation experimentally proved difficult due to surface interactions and diffusion of light through the sides of the ceramics. An alternative method was derived using the data from the neutron measurements by comparing the ratio of light measured from either side of the sample. Specifically, a linear fit of events on the boundaries of the channel vs. channel distribution was compared to the mathematical model of attenuation. The parameters of the model, specifically average attenuation length, was modified until the model fit the slope of the fit.

To illustrate this methodology, a Monte-Carlo simulation of the entire light yield process was developed to show how modifying the attenuation length and the mathematical model used for attenuation effect the shape of a simulated channel vs. channel distribution. This model was based on parameters of a 290 μm thick phosphor screen. Each simulation sampled 5 000 events from an MCNP6 simulation of capture depth (discussed in Chapter 2). This event depth was used with a reasonable attenuation length (on the order of the thickness of the screen) in two models of attenuation to predict the attenuation to either side of the screen. Each simulation also sampled energy deposition and scintillation efficiency, respectively, from the optimal energy deposition model developed in Chapter 2 and a normal distribution with a mean of 90 000 photons MeV^{-1}. Figure 4.22 demonstrates the change in the shape of the distribution based on changing the attenuation length (200 and 500 μm) and the attenuation model (discussed in more detail below). From these simulations, it is apparent that decreasing the attenuation length (meaning a more opaque material) causes the distribution to be more densely populated near the axes rather than the diagonal. The simulations with 200 and 500 μm attenuation lengths shows that the more transparent samples (i.e. 500 μm) have a distribution more densely populated near $y = x$.

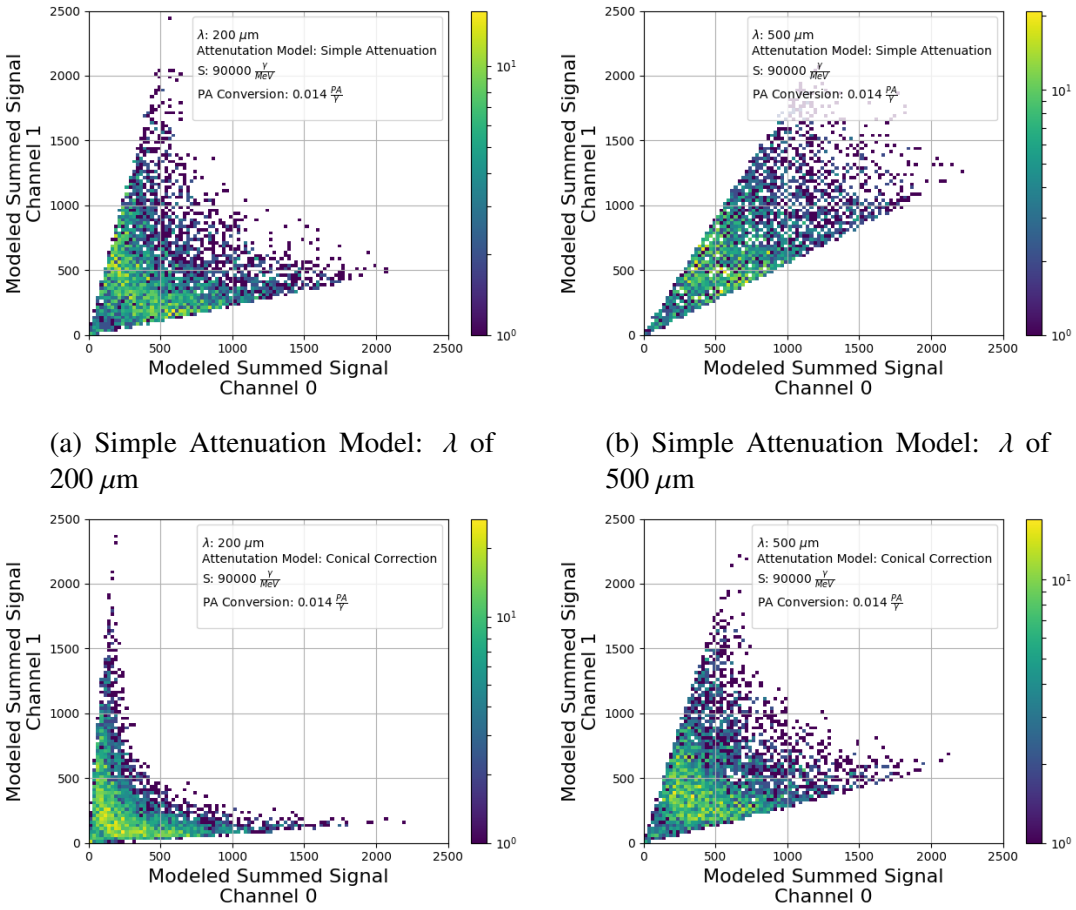

(a) Simple Attenuation Model: λ of 200 μm

(b) Simple Attenuation Model: λ of 500 μm

(c) Conical Attenuation Model: λ of 200 μm

(d) Conical Attenuation Model: λ of 500 μm

Figure 4.22: Comparison of Monte-Carlo simulations of emitted light from either side of the Scintacor screen. The simulations varied the attenuation length and the model used to demonstrate the expected change in the shape of the channel vs. channel distributions.

The simulated distributions using a simple attenuation model and an attenuation model with the conical correction presented in Figure 4.22 show the impact of using either model. Each model was discussed in detail in Chapter 2. Changing the model has a similar effect on the shape of each simulation as changing the attenuation length and either model could be used to match the shape of the data by adjusting the attenuation length. Comparing Figures 4.22a and 4.22d demonstrates the same shape results

from different models by adjusting the attenuation length. Therefore, no conclusion can be made regarding the accuracy of either model. These models can only be used to replicate the effects of attenuation and provide some indication as to the relative attenuation lengths of the selected samples. Both models were used throughout the analysis to estimate attenuation and provide a comparison.

As can be seen from Figure 4.22, the attenuation length and the general effects of attenuation can be estimated by the slope of events on the boundary of the channel vs. channel distribution. This was accomplished by comparing the slope of a linear fit of the boundary data with a ratio of the modeled attenuation at the edges of the sample.

The ratio of light emitted from one side of the sample to the other can be described by,

$$\frac{I_2}{I_1} = \frac{I_0\left(e^{\frac{-t+x}{\lambda_l}} - \alpha_H\,(t-x)\right)}{I_0\left(e^{\frac{-x}{\lambda_l}} - \alpha_H\,(x)\right)}, \tag{4.6}$$

where I_0 is the initial intensity of light emitted from the ZnS(Ag) determined by the scintillation efficiency and energy deposited in ZnS from the charged particles released from neutron capture. The attenuation term,

$$e^{\frac{-x}{\lambda_l}} - \alpha_H\,(x)\,, \tag{4.7}$$

comes from (2.11) which includes the simple attenuation law and Herzkamp's correction term for the conical path of light. This model assumes the light is emitted isotropically and that attenuation is homogeneous on either side of the event. By assuming a

depth near the edge of the sample ($x = t$ or $x = 0$), this ratio can be simplified to,

$$\frac{I_2}{I_1} = \frac{1}{\left(e^{\frac{-t}{\lambda_I}} - \alpha_H(t)\right)} \quad \text{for} \quad x = t, \qquad \text{and} \qquad \frac{I_2}{I_1} = \frac{\left(e^{\frac{-t}{\lambda_I}} - \alpha_H(t)\right)}{1} \quad \text{for} \quad x = 0. \tag{4.8}$$

These equations represent the theoretical boundary slopes for the extremes of the channel vs. channel integrals in Figures 4.8 to 4.11. These equations were compared to the slope of a linear fit of events in the 95$^{\text{th}}$ percentile of these distributions. Figure 4.23 shows an example of this fit for the Scintacor screen.

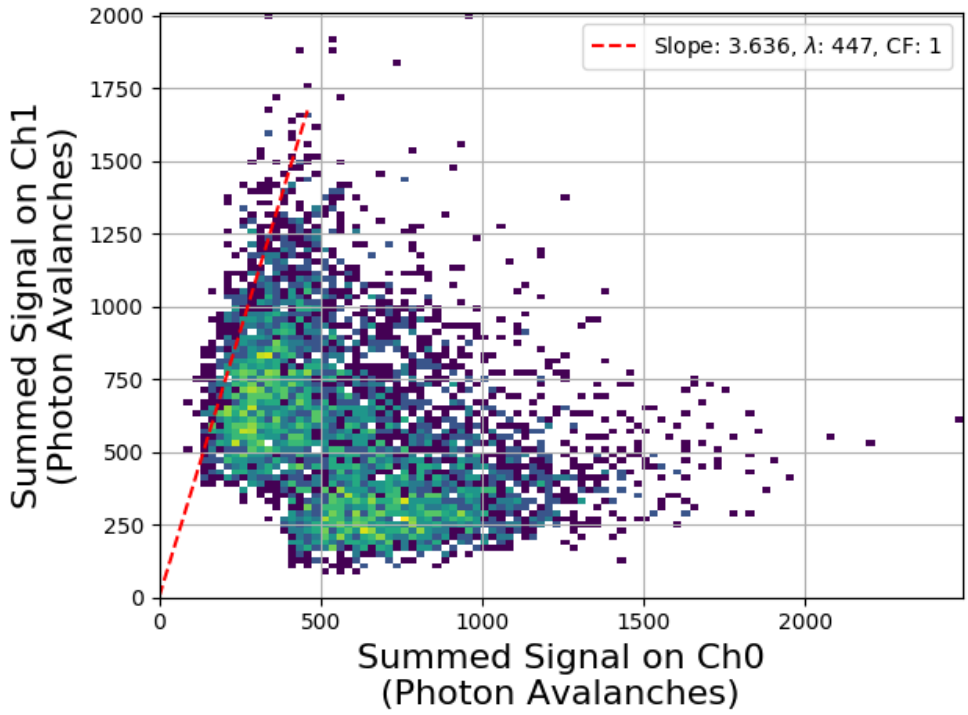

Figure 4.23: Distribution of summed signals on each channel with a fit of the outermost data using the attenuation model with the conical correction.

The attenuation length in (4.6) was modified until the resultant ratio was within 0.001% of the slope of the fit. This method yields different attenuation lengths with and without the attenuation correction factor. The attenuation length for each sample using this method with the two models is provided in Table 4.7.

Table 4.7: Attenuation Length Estimates

Sample	Thickness (μm)	λ_l (μm)	
		Simple Attenuation Model	Model with Conical Correction
Scintacor	290	216	447
160816-3 BN:ZnS(Ag) NC-1 1:87	1895	1201	2406
160816-4 BN:ZnS(Ag) NC-1 1:87	640	696	1628
170616-6A BN:ZnS(Ag) FS-1 1:87	590	304	569
170621-1B BN:ZnS(Ag) FS-1 1:22	1070	1143	2674

The attenuation lengths with the Herzkamp correction are roughly twice that without the correction. Based on these results it is still unclear which method makes a more accurate prediction of the attenuation length. Additional experiments are required to measure attenuation length and comment on the accuracy of the models.

The attenuation lengths do appear to show some correlation with the thickness of the sample independent of the model, as shown in Figure 4.24. This is problematic considering the attenuation length was assumed to be a microscopic material property independent of the macroscopic thickness.

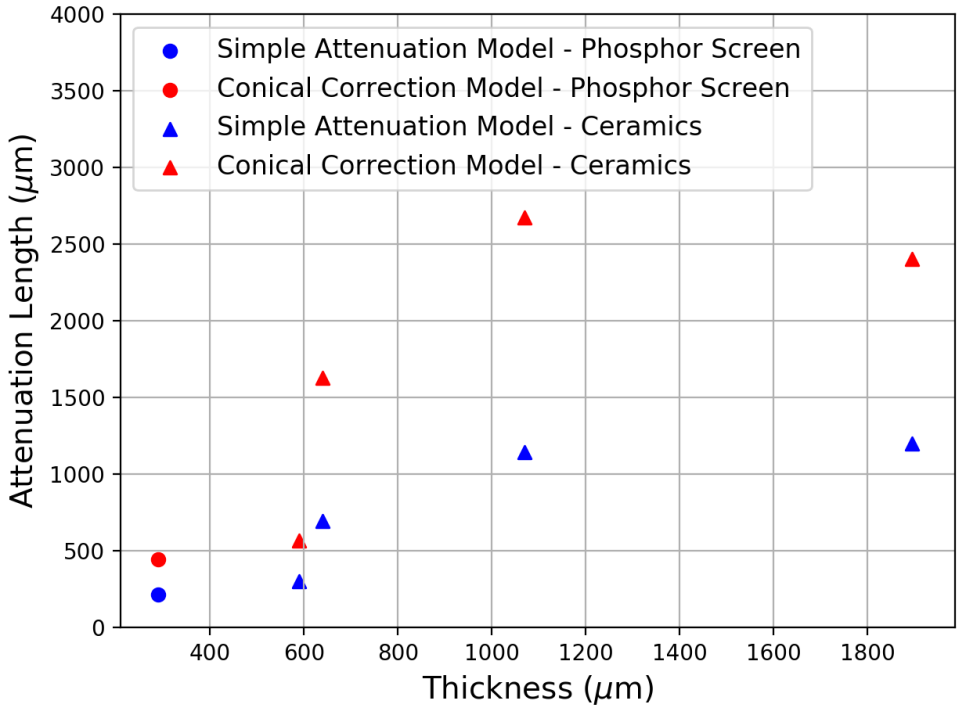

Figure 4.24: Attenuation Estimates Compared to Thickness

Event Depth

With an estimated attenuation length, the depth of each event classified as a neutron was estimated to calculate the amount of attenuation for that event. Depth was estimated by using the ratio of signals seen on both channels, in a similar method used to find the attenuation length. Figure 4.25 shows the results of these depth estimates using the attenuation model with the conical correction compared to MCNP6 models of capture depth. A noticeable void of events in the center of the samples is evident for the 170616-6A and 170621-1B samples. This region is likely to produce low amplitude events that were indistinguishable from the noise and therefore not classified as neutrons.

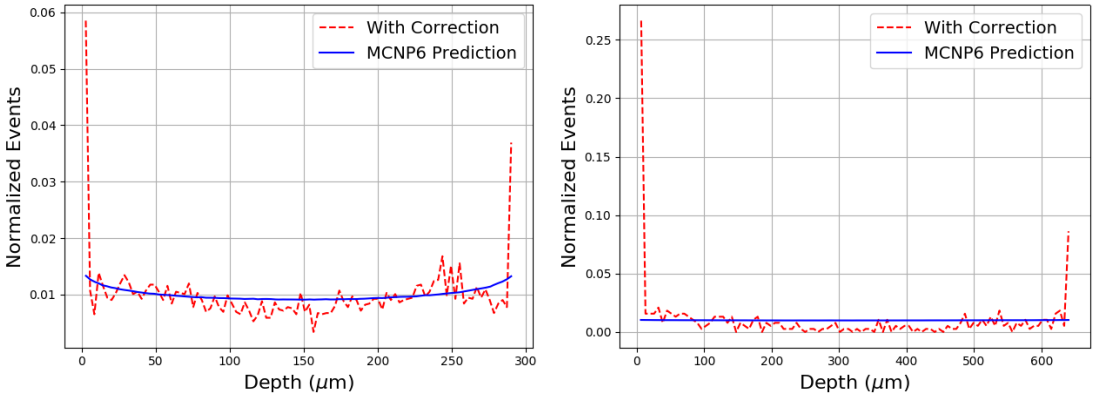

(a) Scintacor

(b) 160816-4

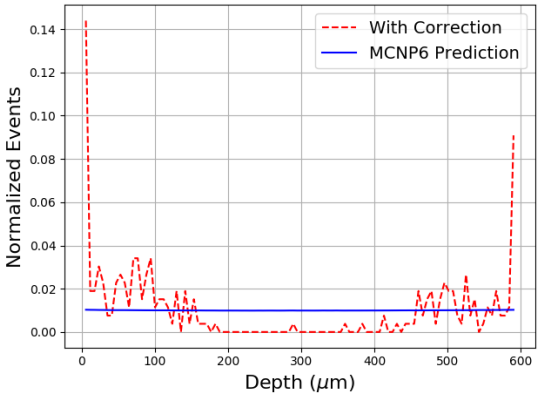

(c) 170616-6A

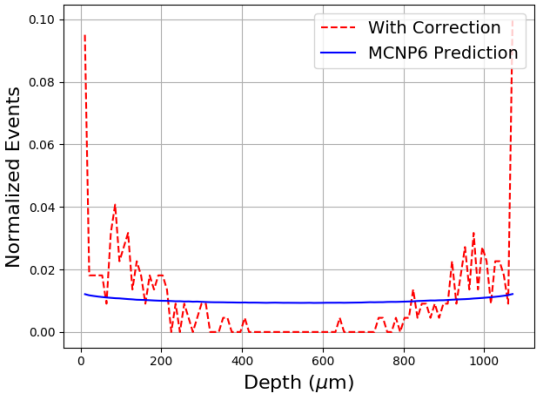

(d) 170621-1B

Figure 4.25: Estimates of event depth of neutrons for (a) the Scintacor screen, (b) the 160816-4 BN:ZnS(Ag) ceramic with NC-1 powder, (c) the 170616-6A BN:ZnS(Ag) ceramic with FS-1 powder, and (d) the 170621-1B BN:ZnS(Ag) ceramic with FS-1 powder in a 1:22 ratio.

Comparison to Energy Deposition Models

The depth assigned to each event and the estimated attenuation length were then used to estimate the attenuation for each channel for each event. The attenuation estimate, an estimate for scintillation efficiency, and an estimate for the efficiency of photon collection and conversion to signal were used to estimate the energy deposition of each event classified as a neutron.

The energy deposition in ZnS, E_n, can be related to the signal on each channel, Q_0 and Q_1, by,

$$E_n = \frac{Q_0 + Q_1}{\epsilon_{\text{scintillation}} \times \epsilon_{\text{SiPM}} \times \epsilon_{\text{LC}} \times (\alpha_l(x) + \alpha_l(t-x))}, \tag{4.9}$$

where $\alpha_l(x)$ and $\alpha_l(t-x)$ is the attenuation to either side of the sample based on the estimated depth and attenuation length. The scintillation efficiency, $\epsilon_{\text{scintillation}}$, is assumed to follows a normal distribution with a mean value in the range of 75 000 and 150 000 photons MeV^{-1}, based on the reported and theoretical limits of scintillation discussed in Chapter 1.

The conversion efficiency of the SiPM, ϵ_{SiPM}, is estimated to be 18%, based on a technical report claiming 18% of the photons incident on the SiPM cause a PA for 450 nm light at 1.5 V overvoltage [104]. The light collection efficiency, ϵ_{LC}, of the apparatus requires additional experimentation to measure its value. In the absence of those measurements, light collection efficiency was estimated at 8% and was based on fits of the data to the model that result in scintillation efficiencies less than the theoretical limit. This assumes each side of the apparatus has identical collection efficiency ignoring the reality that light propagates uniquely for each side. It is also assumed the emission wavelength of each sample is roughly 450 nm and therefore does not affect the collection or SiPM conversion efficiencies.

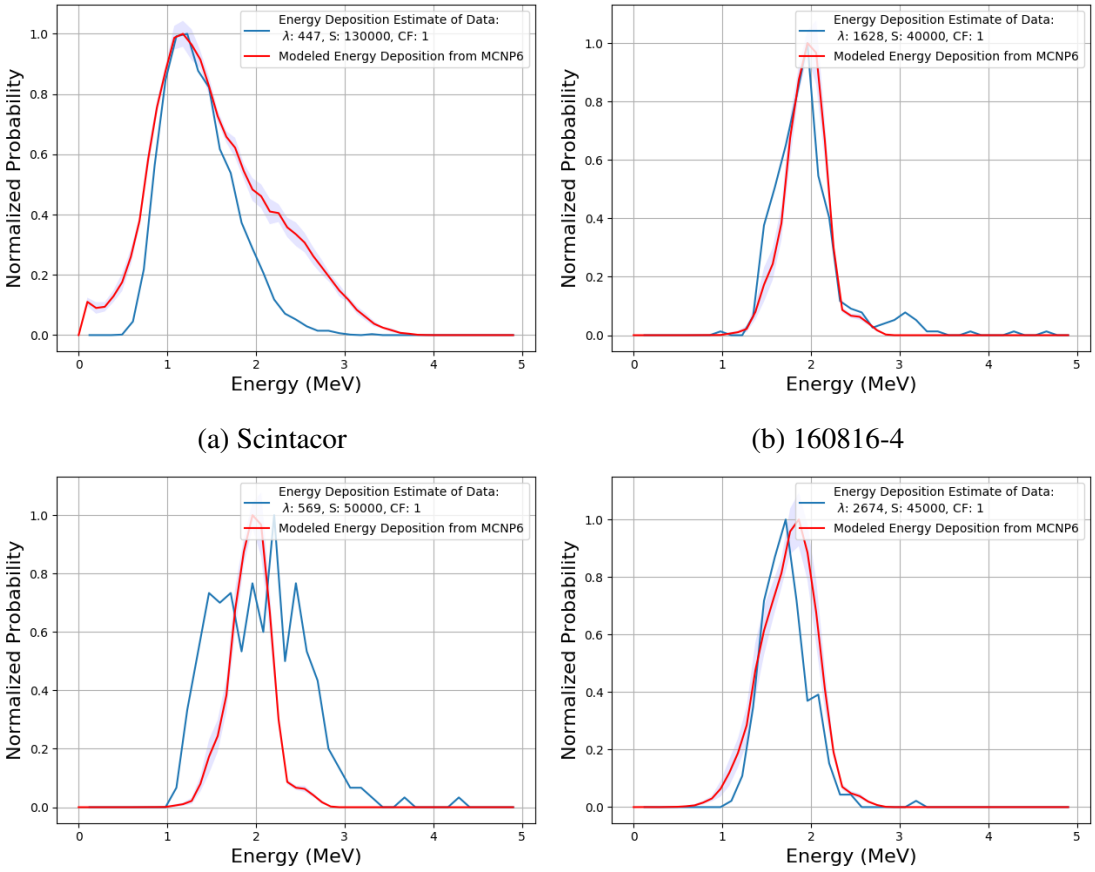

(a) Scintacor (b) 160816-4

(c) 170616-6A (d) 170621-1B

Figure 4.26: Comparison of energy deposition estimates using data from AmBe experiments and MCNP6 models for (a) the Scintacor screen, (b) the 160816-4 BN:ZnS(Ag) ceramic with NC-1 powder, (c) the 170616-6A BN:ZnS(Ag) ceramic with FS-1 powder, and (d) the 170621-1B BN:ZnS(Ag) ceramic with FS-1 powder in a 1:22 ratio. The scintillation efficiency was modified in each scenario to best match the estimate from the data to the MCNP6 model.

Figure 4.26 shows the results of the analysis of the data using equation (4.9) compared to the MCNP6 models for energy deposition. The mean value of the estimated energy deposition from the data was adjusted by decreasing or increasing the scintillation efficiency until the value corresponded to the mean value of the modeled energy deposition. Higher scintillation efficiencies resulted in a lower mean value and narrowed

the distribution due to the expectation that the scintillation efficiency followed a normal distribution. This resulted in a scintillation efficiency of 130 000 photons per MeV for the Scintacor screen which is below the theoretical limit of 150 000, but higher than the reported range of 75 000 to 90 000 photons per MeV. The scintillation efficiency of the ceramics using this method is around 45 000 photons per MeV, or roughly half the expected value.

It is feasible that the degradation in light yield can be attributed to degradation in scintillation efficiency, but there are too many unknown variables in equation (4.9) to definitively make that attribution to the scintillation efficiency or any one factor. It was originally assumed that the scintillation efficiency of the ZnS(Ag) powders used to fabricate the ceramics was comparable to the powders used by Scintacor. Various measurements to try and quantify this value were complicated by the experimental setups and therefore were not reported. Qualitatively, the powders used to fabricate the ceramics and the phosphor screens showed very similar responses to photoluminescence which provided some confidence that the scintillation efficiencies were similar. If the scintillation efficiency of the ceramics is degraded, this implies the degradation occurred in the sintering process and is not due to the powders. Additional measurements are needed to explore this possibility and should include quantifying the light collection and photon conversion efficiencies of the apparatus.

The light yield degradation could alternatively be due to uncertainty in the attenuation length or some overlooked attenuation phenomenon like total internal reflection in the ceramics. Methods to measure optical attenuation using traditional transmittance methods proved inconclusive due to complications in the measurements related to varying thicknesses, surface polishes, and light escaping the sides of the thicker ceramics. It is also possible that total internal reflection is different for the ceramic than the phos-

phor screen. The ceramic is predominantly ZnS which has an index of refraction of 2.47 [105] and has a critical angle of 24°. It is assumed that light transitions from the phosphor screen to the air via the binder which has an index of refraction of 1.44 (polydimethylsiloxane) [106] resulting in a critical angle of 44°. The difference in these angles results a solid angle that is three times larger for the screen than the ceramic meaning less light escapes the ceramic. Additional experiments are needed to confirm these possibilities as well.

Despite the uncertainty as to why the light yield in the ceramics is much less than the phosphor screen, the shape of the histograms (apart from the 170616-6A ceramic) show decent agreement with the models developed in Chapter 2. The difference between the shape of the model and the energy deposition estimate at high energies in the Scintacor screen may be due to unaccounted for phenomena. This could be edge effects (i.e. the triton escaping) resulting in fewer events at high energy depositions or the α deposits less energy than predicted. Figure 2.21 suggests the shape of the distribution at higher energies is more dependent on the additional contribution of the α and the shape of the energy deposition estimate more closely resembles the shape of the modeled triton energy deposition profile in Figure 2.21 rather than the combined deposition, as shown in Figure 4.27.

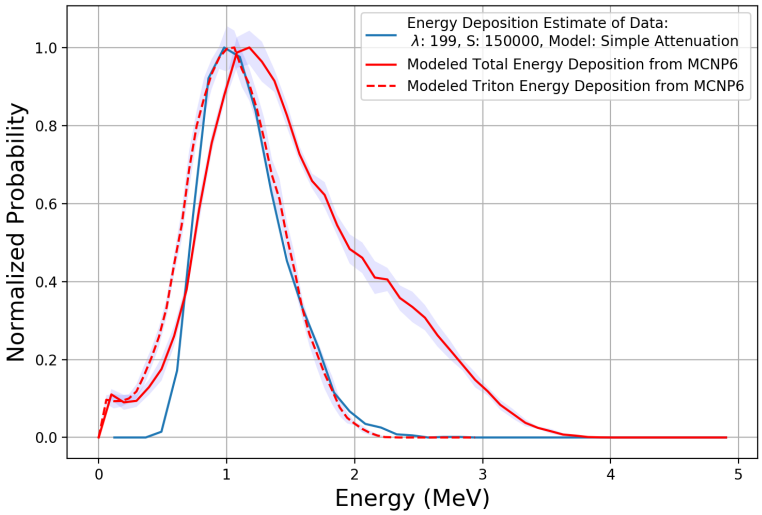

Figure 4.27: Comparison of the total and triton energy deposition models to the energy deposition estimate for the Scintacor screen. This energy deposition estimate uses the simple attenuation model and a scintillation efficiency of 150 000 photons MeV^{-1} to illustrate the similarities to the modeled triton deposition instead of the total deposition.

4.3 Conclusions and Recommendations

Measurements were conducted by exposing the samples to a neutron source in a test apparatus designed to maintain uniformity from run to run. Under these conditions, it was assumed each sample will experience the same dose rate of neutrons at similar energies. The neutron response of composite ceramics under these test conditions were compared to the response of a Scintacor screen. The results of these experiments indicate the ceramics detect neutrons, albeit, not at the same rate or with the same magnitude of light yield as the Scintacor screen. Further experiments are recommended to increase confidence in these results and explore causes of some of the unexpected results.

The test apparatus provided a method for maintaining uniformity of measurements

but the photon collection and conversion needs to be quantified. Redesigning the light collection apparatus may also provide improved light collection through optimizing the shape of the air gap between the sample and the SiPM, using PMTs rather than SiPMs (although this creates further deviation from the SoLid system), or possibly incorporating optical grease or optical fibers to better couple the sample to the photodetector.

The measurements indicate the scintillation of the ceramics was a product of neutrons and not gammas. However, further tests with sources that produce gammas at energies closer to the AmBe source should be conducted to definitively quantify the response of the samples and photodetectors to the gammas produced from the AmBe source.

The light yield analysis provides some validation of the model developed in Chapter 2. Unknowns in the analysis prevented attribution to just one factor related to light yield. Experiments to quantify attenuation, scintillation efficiency, and the collection and conversion efficiencies would provide additional insight into which factors are degrading the light yield of the ceramic and potentially insight to improve the ceramics. The attenuation analysis implies the ceramics are more transparent than the Scintacor screen, but additional measurements are needed to verify this and validate the models. Similarly, the results suggest the scintillation efficiency was degraded which can only be confirmed through additional measurements to quantify scintillation efficiency.

Ultimately, the ceramics successfully demonstrated the proof of concept and the neutron measurements provided some validation to the models developed in Chapter 2. Further development of the ceramics may lead to increased performance beyond the Scintacor screens.

Chapter 5

Conclusions and Recommendations

This effort culminated in the demonstration of a new material that can detect neutrons. This achievement was the product of developing:

- a new model to estimate the light yield based on simulating the microscopic process of energy deposition in ZnS with MCNP6,
- a method to sinter ZnS(Ag) using FAST while retaining the luminescent properties and providing greater translucency than phosphor screens,
- a method to cheaply fabricate composite ceramics of ZnS(Ag) and BN capable of detecting neutrons,
- a new experimental setup to characterize the response to neutrons, and
- a new analytic technique to characterize processes related to the light yield.

This research has produced results demonstrating the potential for further advancement of ceramic neutron detectors. Additional research to improve the fabrication process may realize a ceramic with higher neutron detection efficiency than the ^{6}LiF:ZnS(Ag)

phosphor screens. This effort also reaches conclusions that justify altering the fabrication technique. The modeling and simulation tools developed for this effort revealed gaps in understanding that also justify additional investigation. Furthermore, the methods to characterize the optical properties of the ceramics and quantify properties related to the neutron detection efficiency could be improved.

5.1 Material Fabrication

Ceramics of BN and ZnS(Ag) were successfully fabricated via sintering with the FAST method. The ceramics improved the translucency compared to the phosphor screens, maintained luminescent properties, and successfully detected neutrons. Further development of the ceramics could improve aspects of each of these areas.

Ceramic research would be aided by complementary improvement of techniques to assess the attenuation length and translucency. Early attempts with traditional techniques to assess the attenuation length were complicated by the varying quality of the polish which contributed to varied degree of reflection at the surface. Additionally, the diffuse scattering within the ceramic complicated measurements using standard spectrophotometers. Assessment of the optical properties of the ceramics should include measurements of the surface reflectivity, precise measurements of thickness, and measurements of all transmitted light. These measurements could be compared to the analysis of neutron measurements to validate that approach.

To further improve the luminescent properties of the ceramic, the current process should be refined. These refinements might include the sintering process, using alternative tooling and/or sacrificial layers, and changing the starting materials. The transparency and luminescent properties of the ceramics changed with the sintering profile.

This effort identified bounds to the peak temperature and dwell time, but further experimentation is needed to determine the optimal values. Aside from these parameters, this effort made no attempt to explore other parameters of the sintering process. In particular, other efforts indicated the heating rate impacted transparency [87]. In addition to exploring the heating rate, dynamic heating profiles may also improve transparency. Some of the most translucent samples in this effort were made during the PSD calibration of the FAST machine. This improved translucency may have been a result of the cyclic heating profile. Attempts to reproduce this cyclic heating profile was difficult due to variability noticed in the machine after months of use. The overall reproducibility using the FAST machine became a significant issue when trying to confirm results.

Another parameter of the heating profile that was not explored was the pressure. Due to strength limitations on the carbon punches and dies, 50 MPa could not be exceeded. Translucent ceramics using optimal heating rates were also sintered at a pressure of 80 MPa [87]. Other efforts pursuing transparent ZnS ceramics explored pressures as high as 100 MPa [57]. Higher pressures would require higher-strength tooling in the form of re-engineered dies and punches. An alternate vendor claims its carbon dies and punches can withstand the higher pressures. The only difference in the tooling appears to be the dimensions and potentially the density. Alternatively, this vendor also provides tungsten carbide tools that it claims can be used with FAST at higher pressures. Not only sintering at higher pressures, but new tools would require re-optimizing the heating profile.

The luminescent and optical properties would also likely improve by modifying the starting powders. The literature on sintering ZnS powders into ceramics suggests greater transparency is achievable with sub-micron sized powders [57, 84, 87]. These sub-micron sized powders can be achieved by either ball-milling commercial powders to reduce the powder size, purchasing commercial nano-sized powders, or synthesizing

nano-particles. A major concern in incorporating any of these options is the impact to the luminescent properties; a factor that was not considered in prior efforts. The manufacturer of the ZnS(Ag) powders in this effort claimed the intensity of luminescence decreased with decreasing particle size. Photoluminescent tests of the powders could not confirm this claim; however, this trend is confirmed in the literature for efforts to quantify the luminescence of ZnS nanoparticles. Luminescence of ZnS nanoparticles also experiences a blue-shift due to quantum confinement effects which would potentially effect the neutron detection properties [107, 108]. Like sintering with higher pressures, adjusting the particle size would require re-optimizing the heating profile of the sintering process.

A problem associated with sintering was the carbon migration that degraded the optical properties and possibly the luminescent properties. This carbon was almost assuredly from the sacrificial graphite rather than the tooling itself. Carbon contamination varied with heating profiles and was more prominent on one face of the ceramic than the other suggesting the joule heating had an effect. Some options to reduce the carbon contamination might include coating the graphite with a thin layer of BN. Hexagonal BN is a common lubricant (like graphite) and would be preferred to other lubricants. If the BN could not be removed during the polishing process or there was some migration, this would add to the boron content rather than introducing a contaminant. More expensive alternatives include replacing the graphite with thin sheets of conductive molybdenum or platinum. These larger atoms may be less likely to migrate into the ceramic compared to the carbon, but the additional cost may make any advantage cost-prohibitive.

Another means of reducing carbon migration may be to sinter using HUP rather than FAST. As suggested by the gradient of the carbon contamination, carbon migration may have increased due to joule heating. Furthermore, the FAST method proved difficult in

terms of reproducibility and optimizing the sintering process. Sintering with a traditional method like HUP may reduce the contamination and improve reproducibility at the expense of speed and the potential for increased grain-growth.

Another detriment to the optical properties is the BN. More involved means of incorporating boron may be beneficial to the optical/luminescent properties of the ZnS ceramic in addition to improving the coupling of energy to the ZnS, as suggested by the models in Chapter 2. One option is to synthesize boron-doped ZnS(Ag) nanoparticles. Luminescent ZnS(Ag) nanoparticles have been synthesized using various chemical precipitation methods [109, 110]. When substituting dopants like Ag onto Zn^{2+} lattice sites, it is common to oxidize the dopant to a similar oxidation state to maintain a neutral lattice (i.e. Ag^{2+}). Co-dopants or co-activators are often used in conjunction with the dopant to maintain the neutral lattice and in some cases enhance the light yield [111, 112]. For example, Ag^{+} might be co-doped with Al^{3+} at two Zn^{2+} sites or Ag^{+} might be co-doped with Cl^{-} where the Ag occupies a Zn^{2+} site while the Cl occupies a S^{2-} site [113]. The similarity in the valence state of B^{3+} to Al^{3+} makes it a reasonable substitute as a co-activator with Ag^{+}. Co-doping boron in the precipitation process would require modifications to the chemical processes, but boric acid could be incorporated into the process in a similar manner to precipitation methods used to dope boron into cadmium sulfide nano-particles [114]. Another advantage is that enriched boric acid is readily available from commercial vendors like Sigma Aldrich. If boron could be used as a co-activator, co-doping B^{3+} with Ag^{+} into ZnS would be the most efficient method of translating the energy released from neutron capture to luminescence.

These nanopowders could then be sintered using FAST or HUP or even loaded into scintillating plastics for other neutron-detecting applications. At one point during the SoLid detector's design, neutron-sensitive scintillating plastics were considered as a

substitute for the combination of the PVT and phosphor screens. At the time, these plastics did not have comparable light yield to the PVT, but improvements in recent years to increase light yield have made them an enticing alternative. A remaining drawback of these plastics is that the PSD is insufficient for SoLid. Loading boron-doped ZnS nanoparticles into a plastic like PVT might provide the discrimination and light yield needed for applications like SoLid.

Other methods to incorporate boron with ZnS is to dope the boron in the ceramic post sintering or to use CVD with boron incorporated in the growth process. Ion implantation or thin layer deposition accompanied with annealing of the ceramic could induce boron migration into the ceramic. As stated in Chapter 3, the most transparent ZnS materials are ceramics made from CVD/HIP or single crystals [93]. Rather than doping after the fact, the boron could be incorporated into the CVD or single crystal growth process; however, this would likely require significant effort to optimize the process.

While this effort focused on developing ceramics, results from the modeling and simulation revealed areas that might improve the performance of the phosphor screens. The energy deposition models indicated greater signals would be generated if both the particle size and the amount of binder used was reduced. The models also indicated using less dense binder would also generate greater signals in the phosphor screen. While these modifications would likely improve the signal, they would have no effect on increasing the probability of capture on the screens.

5.2 Modeling and Simulation

Models were developed to predict the energy released from neutron capture on Li and B and the subsequent microscopic process of energy deposition in ZnS for screens and

ceramics. Using these models, the light yield was predicted for varying compositions and grain sizes. The measured light yield from the ceramics and screens showed some correlation to these models though the light yield for the ceramic was less than predicted. It is possible the reduced light yield was due to an unaccounted phenomenon in the energy deposition model.

One such phenomenon could be the high carbon contamination within the ceramics. Like the binder in the phosphor screens, additional grains of carbon in the ceramic matrix would serve to reduce the energy deposited in ZnS. This could be modeled by adding additional cubes to the current ceramic model. Without microscopic investigation and quantification of the carbon content in the ceramic, this model would be the best approximation for incorporating carbon. Alternatively, the carbon may migrate into the ZnS crystal matrix which would be better modeled by adding carbon into the composition of the ZnS rather than creating a new shape. Such modification of the model would not likely change the energy deposited in the ZnS cubes. Rather this physical phenomenon would likely reduce the scintillation efficiency of the ZnS crystal.

As suggested in Chapter 4, discrepancies between the model and the data analysis of the Scintacor screen may be related to edge effects where tritons escape the screen or due to an unexpectedly low contribution to the energy deposition from the α particles. The simplest method to incorporate the edge effects would be to use a macroscopic model to estimate the energy deposited outside of the material and then use this value as a correction to the current microscopic model. As stated in Chapter 2, an initial model for these edge effects was already developed, but the correction was negligible and therefore was only mentioned in this effort. The low contributions of the α particle, on the other hand, may be related to variations in grain size that were not incorporated into the model or "clumping" of the LiF resulting in sub-optimal transport of α particles

to the ZnS. This could be explored by refining the placement of particles and developing methods to include grain size stochastics into each simulation.

The low contribution of light from the α may also be due to a non-linear scintillation response by the ZnS or a shift in the emission wavelength due to high ionization density. The α and triton (and ^{7}Li) have different ionization densities that may result in a non-linear response or relaxation through states that produce different wavelengths. This non-linear response would reduce the total light yield whereas a shift in wavelength form the peak efficiency wavelength would result in an overall lower detection efficiency of the SiPMs. This phenomenon may also play a factor in the reduced light yield related to the BN:ZnS ceramics where both the ^{7}Li and α would have high ionization densities. Experiments to test this hypothesis may reveal the non-linear and spectral dependence on particle mass and could be used to correct the respective scintillation distribution or conversion factor in the model.

Another process not considered in the model is the propagation and attenuation of light through the micro crystals in the ceramic and the phosphor screens. Modeling these processes at the microscopic level may aide in predicting how the grain size or composition may impact the light yield. This information would be valuable in design decisions to optimize the light yield.

5.3 Experimental Measurements

The test apparatus provided an effective tool of exploring the radioluminescent properties of screens and ceramics and provides a means of estimating attenuation length. It also utilized the SoLid readout, namely the SiPMs and DAQ, which simplifies the evaluation of substituting the ceramics for the phosphor screens. Further experiments

with the current batch of samples might include testing samples of the same composition but different thickness. This would enable better attribution of the neutron rates and light yields to the design parameters. These measurements would also provide means to better assess the attenuation length.

The analysis of the neutron measurements suggests the light collection efficiency of the apparatus is on the order of 8% and the photon detection efficiency of the SiPMs is on the order of 18%. Modifications to improve sensitivity to light might include replacing the SiPMs with more sensitive PMTs, improving the light collection properties of the cavity (i.e. shape and reflective surfaces), or replacing the cavities with optical coupling (i.e. either waveguides or directly coupling the photosensors to the sample with optical grease). While PMTs offer increased photosensitivity, there are also many drawbacks. PMTs are more expensive, are sensitive to magnetic fields, and are also more sensitive to gammas which would significantly increase the noise and possibly saturate the DAQ.

The apparatus was also designed to be modular with a vision of eventually incorporating spectroscopic measurements in the analysis. Further work on the apparatus to include spectroscopic measurements of neutron events and background may provide additional information regarding the luminescent mechanisms of ZnS or provide another means of discriminating neutrons from background. These measurements may also be a means for testing to confirm if different particles result in different luminescent wavelengths and hence change the light output.

In conjunction with exploring the spectroscopic differences in particle excitation, further tests should be conducted to characterize the neutron response of the apparatus. Neutrons may (although unlikely) activate atoms within the apparatus causing it to emit additional radiation. High neutron fluxes have also been measured to affect the response of SiPMs [115], although this effect should be negligible for the flux used in these

experiments and in SoLid. Neutrons may also cause carbon or hydrogen in the apparatus to recoil and interact with the sample. Recoiling carbon within the pure ZnS ceramics may be the cause of the neutron events.

Tests should also be conducted to characterize the scintillation of the ZnS in the presence of gamma, beta, ^{1}H, ^{3}H, ^{4}He, ^{7}Li, and ^{12}C to explore the possibility of a non-linear response of the ZnS. These experiments would have to be conducted at a facility such as the National Physical Laboratory (NPL) that provides access to particle accelerators. Such an experiment may need significant modifications to the existing test apparatus. The trigger in the DAQ would also need to be set such that all signals are read-out and not just the neutron signals. Conducting experiments at NPL would also present an opportunity to take absolute neutron measurements with the samples in the current apparatus. The portability of the apparatus would simplify taking measurements at this facility and would only require MCNP models of the apparatus to accurately predict the flux through the sample.

This effort has laid the groundwork for additional exploration of composite ceramics for neutron detection, predictive models of these ceramics, and methods to measure the neutron response. Additional research to improve and optimize the ceramics may result in a new material with increased sensitivity than phosphor screens at a fraction of the cost.

Bibliography

[1] J. Birks, *The Theory and Practice of Scintillation Counting*. Elsevier, 1964.

[2] W. R. Mills, R. L. Caldwell, and I. L. Morgan, "Low Voltage He^3-Filled Proportional Counter for Efficient Detection of Thermal and Epithermal Neutrons," *Review of Scientific Instruments*, vol. 33, no. 8, pp. 866–868, 8 1962.

[3] R. T. Kouzes, A. T. Lintereur, and E. R. Siciliano, "Progress in alternative neutron detection to address the helium-3 shortage," *Nuclear Instruments and Methods in Physics Research Section A: Accelerators, Spectrometers, Detectors and Associated Equipment*, vol. 784, pp. 172–175, 6 2015.

[4] T. Nakamura, T. Kawasaki, T. Hosoya, K. Toh, K. Oikawa, K. Sakasai, M. Ebine, A. Birumachi, K. Soyama, and M. Katagiri, "A large-area two-dimensional scintillator detector with a wavelength-shifting fibre readout for a time-of-flight single-crystal neutron diffractometer," *Nuclear Inst. and Methods in Physics Research, A*, vol. 686, pp. 64–70, 2012.

[5] N. J. Rhodes, E. M. Schooneveld, and R. S. Eccleston, "Current status and future directions of position sensitive neutron detectors at ISIS," *Nuclear Instruments and Methods in Physics Research A*, vol. 529, pp. 243–248, 2004.

[6] J. Ely, S. Robinson, M. Bliss, E. Siciliano, R. Kouzes, M. Swinhoe, A. Lintereur, and M. Woodring, "PNNL-23011," Pacific Northwest National Laboratory, Richland, Washington, Tech. Rep., 2013.

[7] K. Wilhelm, J. Nattress, and I. Jovanovic, "Development and operation of a ^{6}LiF:ZnS(Ag)—scintillating plastic capture-gated detector," *Nuclear Instruments and Methods in Physics Research Section A: Accelerators, Spectrometers, Detectors and Associated Equipment*, vol. 842, pp. 54–61, 1 2017.

[8] B. W. Miller, S. J. Gregory, E. S. Fuller, H. H. Barrett, H. Bradford Barber, and L. R. Furenlid, "The iQID camera: An ionizing-radiation quantum imaging detector," *Nuclear Instruments and Methods in Physics Research Section A: Accelerators, Spectrometers, Detectors and Associated Equipment*, vol. 767, pp. 146–152, 12 2014.

[9] G. Ban *et al.*, "SoLid: Search for Oscillations with Lithium-6 Detector at the SCK-CEN BR2 reactor," *Nuclear and Particle Physics Proceedings*, 2016.

[10] T. Tojo and T. Nakajima, "Preparation of thermal neutron scintillators based on a mixture of ZnS(Ag), ^{6}LiF and polyethylene," *Nuclear Instruments and Methods*, vol. 53, pp. 163–166, 1967.

[11] A. R. Spowart, "Measurement of the Absolute Scintillation Efficiency of Granular and Glass Neutron Scintillators," *Nuclear Instruments and Methods*, vol. 75, pp. 35–42, 1969.

[12] A. Spowart, "Optimising neutron scintillators for neutron radiography," *The British Journal for Non-Destructive Testing*, vol. 11, no. 1, pp. 2–11, 1969.

[13] T. Kojima, M. Katagiri, N. Tsutsui, K. Imai, M. Matsubayashi, and K. Sakasai, "Neutron scintillators with high detection efficiency," *Nuclear Instruments and Methods in Physics Research A*, vol. 529, pp. 325–328, 2004.

[14] C. Wu, B. Tang, Z. J. Sun, Q. Zhang, Z. Yang, J. Zhang, Y. D. Yang, J. C. Liang, and J. J. Wu, "A study of ZnS(Ag)/^{6}LiF with different mass ratios," *Radiation Measurements*, 2013.

[15] "Thermal Neutron Detector EJ-426," Eljen Technology, Sweetwater, Texas, Tech. Rep., 2016.

[16] A. Spowart, "Measurement of the gamma sensitivity of granular and glass neutron scintillators and films," *Nuclear Instruments and Methods*, vol. 82, pp. 1–6, 1970.

[17] Y. Abreu *et al.*, "A novel segmented-scintillator antineutrino detector," *Journal of Instrumentation*, vol. 12, pp. 1–18, 2017.

[18] J. D. Graves and J. P. Dyson, "A Scintillation Counter for Laboratory Counting of Alpha-Particles," *Citation: Review of Scientific Instruments Alpha-Particle Spec-*

trograph Rev. Sci. Instrum. Sci. Instrum. J. Phys. J. Phys. Ionization Chamber for Counting Alpha-Particles Rev. Sci. Instrum, vol. 20, no. 12, 1949.

[19] G. F. Knoll, *Radiation Detection and Measurement*, 2000, vol. 3.

[20] E. Marsden, "Large Area Thermal Neutron Detectors For Security Applications," Ph.D. dissertation, University of Sheffield, 2012.

[21] G. Barr, R. Devenish, R. Walczak, and T. Weidberg, *Particle Physics in the LHC Era*. Oxford University Press, 1 2016.

[22] A. Aguilar *et al.*, "Evidence for Neutrino Oscillations from the Observation of $\bar{\nu}_e$ Appearance in a $\bar{\nu}_\mu$ Beam," *Physical Review: D*, vol. 64, no. 11, p. 112007, 2001.

[23] Y. Fukuda *et al.*, "Evidence for Oscillation of Atmospheric Neutrinos," *Physical Review Letters*, vol. 81, no. 8, pp. 1562–1567, 8 1998.

[24] T. Kajita, "Atmospheric neutrino results from Super-Kamiokande and Kamiokande, Evidence for muon neutrino oscillations," *Nuclear Physics B - Proceedings Supplements*, vol. 77, no. 1, pp. 123–132, 1999.

[25] N. Jelley, A. B. McDonald, and R. H. Robertson, "The Sudbury Neutrino Observatory," *Annual Review of Nuclear and Particle Science*, vol. 59, no. 1, pp. 431–465, 11 2009.

[26] C. Athanassopoulos *et al.*, "Evidence for $\bar{\nu}_\mu \rightarrow \bar{\nu}_e$ Oscillations from the LSND Experiment at LAMPF," *Physical Review Letters*, vol. 77, pp. 3082–3085, 1996.

[27] G. Mention, M. Fechner, T. Lasserre, T. A. Mueller, D. Lhuillier, M. Cribier, and A. Letourneau, "Reactor antineutrino anomaly," *Physical Review D*, vol. 83, no. 7, p. 073006, 4 2011.

[28] P. Huber, "Determination of antineutrino spectra from nuclear reactors," *Physical Review C*, vol. 84, 2011.

[29] C. Giunti and M. Laveder, "Statistical significance of the gallium anomaly," *Physical Review C*, vol. 83, no. 6, p. 065504, 6 2011.

[30] J. N. Abdurashitov *et al.*, "Measurement of the response of the Russian-American Gallium Experiment to neutrinos from a Cr-51 source," *Physical Review C*, vol. 59, no. 4, p. 2246, 1998.

[31] W. Hampel *et al.*, "Final results of the Cr-51 neutrino source experiments in GALLEX," *Physics Letters B*, vol. 420, no. 1-2, pp. 114–126, 2 1998.

[32] K. N. Abazajian *et al.*, "Light Sterile Neutrinos: A White Paper," 2012.

[33] J. Abdurashitov *et al.*, "Measurement of the solar neutrino capture rate with gallium metal. III: Results for the 2002–2007 data-taking period," *Physical Review C*, vol. 80, no. 1, p. 015807, 1 2009.

[34] J. Choi *et al.*, "Observation of Energy and Baseline Dependent Reactor Antineutrino Disappearance in the RENO Experiment," *Physical Review Letters*, vol. 116, no. 21, p. 211801, 5 2016.

[35] F. P. An *et al.*, "Improved Measurement of the Reactor Antineutrino Flux and Spectrum at Daya Bay," *Chinese Physics C*, vol. 41, no. 1, p. 013002, 2017.

[36] Y. J. Ko *et al.*, "Sterile Neutrino Search at the NEOS Experiment," *Physical Review Letters*, vol. 118, no. 12, p. 121802, 2017.

[37] G. Mention, M. Vivier, J. Gaffiot, T. Lasserre, A. Letourneau, and T. Materna, "Reactor antineutrino shoulder explained by energy scale nonlinearities?" *Physics Letters B*, vol. 773, pp. 307–312, 10 2017.

[38] I. Michiels, "SoLid: Search for Oscillation with a ^{6}Li Detector at the BR2 research reactor," in *NuPhys2015, Prospects in Neutrino Physics, London, UK, Dec 16–18, 2015*, 2015.

[39] L. On Arnold, "Trigger for the SoLid Reactor Antineutrino Experiment," Tech. Rep., 2017.

[40] A. Vacheret, "Novel compact neutrino detector development," in *XXVII International Conference on Neutrino Physics and Astrophysics (Neutrino 2016), London, UK, 4-9 Jul, 2016*, 2016.

[41] A. Oralbaev, M. Skorokhvatov, and O. Titov, "The inverse beta decay: a study of cross section," *Journal of Physics: Conference Series*, vol. 675, 2016.

[42] Y. Abreu *et al.*, "Commissioning and Operation of the Readout System for the SoLid Neutrino Detector," 2018.

[43] M. Chadwick *et al.*, "ENDF/B-VII.1 Nuclear Data for Science and Technology: Cross Sections, Covariances, Fission Product Yields and Decay Data," *Nuclear Data Sheets*, vol. 112, no. 12, pp. 2887–2996, 12 2011.

[44] E. Rutherford, "The scattering of α and β particles by matter and the structure of the atom," *Philosophical Magazine*, vol. 92, no. 4, pp. 379–398, 2016.

[45] C. van Eijk, A. Bessière, and P. Dorenbos, "Inorganic thermal-neutron scintillators," *Nuclear Instruments and Methods in Physics Research Section A: Accelerators, Spectrometers, Detectors and Associated Equipment*, vol. 529, no. 1, pp. 260–267, 2004.

[46] P. Dorenbos, "Light output and energy resolution of Ce^{3+}-doped scintillators," *Nuclear Instruments and Methods in Physics Research A*, vol. 486, pp. 208–213, 2002.

[47] P. G. Koontz, G. R. Keepin, and J. E. Ashley, "ZnS(Ag) Phosphor Mixtures for Neutron Scintillation Counting," *The Review of Scientific Instruments*, vol. 26, no. 26, pp. 352–356, 1955.

[48] R. Stedman, "Scintillator for Thermal Neutrons using ^{6}LiF and ZnS(Ag)," *Review of Scientific Instruments*, vol. 31, no. 10, pp. 1156–1167, 1960.

[49] J. F. Ziegler, M. Ziegler, and J. Biersack, "SRIM – The stopping and range of ions in matter (2010)," *Nuclear Instruments and Methods in Physics Research Section B: Beam Interactions with Materials and Atoms*, vol. 268, no. 11-12, pp. 1818–1823, 6 2010.

[50] P. A. Rodnyi, *Physical Processes in Inorganic Scintillators*. CRC Press LLC, 1997.

[51] J. Randall, M. Wilkins, and M. Oliphant, "Phosphorescence and electron traps II. The interpretation of long-period phosphorescence," *Proceedings of the Royal Society of London. Series A. Mathematical and Physical Sciences*, vol. 184, no. 999, pp. 390–407, 1945.

[52] P. A. Rodnyi, P. Dorenbos, and C. W. E. van Eijk, "Energy Loss in Inorganic Scintillators," *Physica Status Solidi: B*, vol. 187, no. 1, pp. 15–29, 1 1995.

[53] J. H. Ely, M. Bliss, R. T. Kouzes, A. T. Lintereur, S. M. Robinson, E. R. Siciliano, M. T. Swinhoe, and M. L. Woodring, "Final Technical Report for the Neutron Detection without Helium-3 Project," Pacific Northwest National Laboratory, Richland, Washington, Tech. Rep., 2013.

[54] R. K. Crawford, "Position-sensitive detection of slow neutrons: survey of fundamental principles," in *SPIE*, vol. 1737, 1993.

[55] M. Herzkamp, R. Engels, G. Kemmerling, T. Brueckel, A. Stahl, and S. v. Waasen, "Simulation and Optimization of a Position Sensitive Scintillation Detector with Wavelength Shifting Fibers for Thermal Neutrons," *Verhandlungen der Deutschen Physikalischen Gesellschaft*, 2015.

[56] Y. Li and Y. Wu, "Transparent and Luminescent ZnS Ceramics Consolidated by Vacuum Hot Pressing Method," *Journal of the American Ceramic Society*, vol. 98, no. 10, pp. 2972–2975, 2015.

[57] C. Chlique, G. Delaizir, O. Merdrignac-Conanec, C. Roucau, M. Dollé, P. Rozier, V. Bouquet, and X. H. Zhang, "A comparative study of ZnS powders sintering by Hot Uniaxial Pressing (HUP) and Spark Plasma Sintering (SPS)," in *Optical Materials*, 2011.

[58] Y. W. Hong, Y. B. Kim, Y. J. Lee, S. K. Kim, J. H. Paik, and J. H. Kim, "Sintering and of ZnS by hot pressing (HP) and spark plasma sintering (SPS) and optical properties of sintened materical," vol. 53, no. 12, pp. 883–889, 12 2015.

[59] Y. Li, L. Zhang, K. Kisslinger, and Y. Wu, "Green phosphorescence of zinc sulfide optical ceramics," *Optical Materials Express*, vol. 4, no. 6, p. 1140, 6 2014.

[60] J. S. McCloy, M. Bliss, B. Miller, Z. Wang, and S. Stave, "Scintillation and luminescence in transparent colorless single and polycrystalline bulk ceramic ZnS," *Journal of Luminescence*, vol. 157, pp. 416–423, 2015.

[61] S.-B. Kim, T. Lasserre, and Y. Wang, "Reactor Neutrinos," *Advances in High Energy Physics*, vol. 2013, pp. 1–34, 4 2013.

[62] R. Bossi and A. Robinson, "Monte Carlo computer model to optimize light yield from LiF–ZnS scintillators," *Transactions of the American Nuclear Society*, vol. 22 p. 153, 1975.

[63] A. C. Stephan, S. Dai, S. A. Wallace, and L. F. Miller, "Modelling of Composite Neutron Scintillators," *Radiation Protection Dosimetry*, vol. 116, no. 1-4, pp. 165–169, 2005.

[64] Y. Yehuda-Zada, I. Orion, L. Dongwon, O. Hen, A. Beck, Y. Kadmon, Y. Cohen, J. Zigler, N. Maliszewskyj, and A. Osovizky, "Monte Carlo Simulation for Optimizing ^{6}LiF:ZnS(Ag) based Neutron Detector Configuration," vol. 13, p. 30, 2014.

[65] F. B. Brown, W. R. Martin, W. Ji, J. L. Conlin, and J. C. Lee, "Stochastic Geometry and HTGR Modeling with MCNP5," in *ANS Monte Carlo 2005 Topical Meeting*. Chattanooga, Tennessee: American Nuclear Society, 2005.

[66] J. T. Goorley *et al.*, "Initial MCNP6 Release Overview - MCNP6 version 1.0," Los Alamos National Laboratory, Tech. Rep., 2013.

[67] M. Tanabashi *et al.*, "Particle Data Group," Tech. Rep., 2018.

[68] M. Thomson, *Modern Particle Physics*. Cambridge University Press, 2013.

[69] "PNNL-21609," Pacific Northwest National Laboratory, Richland, Washington, Tech. Rep., 2012.

[70] E. K. Goharshadi, R. Mehrkhah, and P. Nancarrow, "Synthesis, characterization, and measurement of structural, optical, and phtotoluminescent properties of zinc sulfide quantum dots," *Materials Science in Semiconductor Processing*, vol. 16, no. 2, pp. 356–362, 4 2013.

[71] W. Lehmann, "On the Optimum Efficiency of Cathodoluminescence of Inorganic Phosphors," *Journal of The Electrochemical Society*, vol. 118, no. 7, p. 1164, 7 1971.

[72] C. A. Klein, "Bandgap Dependence and Related Features of Radiation Ionization Energies in Semiconductors," *Journal of Applied Physics*, vol. 39, p. 2029, 1968.

[73] S. Steele and J. Pappis, "Chemical vapor deposition of IR materials," Tech. Rep., 1971.

[74] J. S. McCloy *et al.*, "Photoluminescence in Chemical Vapor Deposited ZnS: insight into electronic defects," *Optical Materials Express*, vol. 3, no. 9, pp. 1273–1278, 2013.

[75] Y. Li, "Photoluminescent Zinc Sulfide Optical Ceramics," Ph.D. dissertation, Alfred University, 2015.

[76] N. Kubota, M. Katagiri, K. Kamijo, and H. Nanto, "Evaluation of ZnS-family phosphors for neutron detectors using photon counting method," *Nuclear Instruments and Methods in Physics Research, Section A: Accelerators, Spectrometers, Detectors and Associated Equipment*, vol. 529, pp. 321–324, 2004.

[77] T. Nakamura, E. Schooneveld, N. Rhodes, M. Katagiri, K. Sakasai, and K. Soyama, "Evaluation of the performance of a fibre-coded neutron detector with a ZnS/$^{10}B_2O_3$ ceramic scintillator," *Nuclear Instruments and Methods in Physics Research Section A: Accelerators, Spectrometers, Detectors and Associated Equipment*, vol. 600, no. 1, pp. 164–166, 2 2009.

[78] E. Walentynowicz and M. A. Czajkowski, "Zinc Sulphide Blue Electroluminescence in Boric Acid-Glass Matrix," *Physica Status Solidi A*, vol. 57, pp. 21–24, 1980.

[79] E. Gatti, E. Germagnoli, A. Persano, and E. Zimmer, "Boron layer scintillation neutron detectors," *Il Nuovo Cimento*, 1952.

[80] G. Will, G. Nover, and J. von der Gönna, "New Experimental Results on the Phase Diagram of Boron Nitride," *Journal of Solid State Chemistry*, vol. 154, no. 1, pp. 280–285, 2000.

[81] Z. A. Munir, U. Anselmi-Tamburini, and M. Ohyanagi, "The effect of electric field and pressure on the synthesis and consolidation of materials: A review of the spark plasma sintering method," *Journal of Materials Science*, vol. 41, no. 3, pp. 763–777, 2 2006.

[82] O. Guillon, J. Gonzalez-Julian, B. Dargatz, T. Kessel, G. Schierning, J. Räthel, and M. Herrmann, "Field-Assisted Sintering Technology/Spark Plasma Sintering: Mechanisms, Materials, and Technology Developments," *Advanced Engineering Materials*, vol. 16, no. 7, pp. 830–849, 7 2014.

[83] L. A. Xue and R. Raj, "Effect of hot-pressing temperature on the optical transmission of zinc sulfide," *Applied Physics Letters*, vol. 58, no. 5, p. 441, 1991.

[84] C. Chlique, O. Merdrignac-Conanec, N. Hakmeh, X. Zhang, and J. L. Adam, "Transparent ZnS ceramics by sintering of high purity monodisperse nanopow-

ders," *Journal of the American Ceramic Society*, vol. 96, no. 10, pp. 3070–3074, 2013.

[85] C. Yeh, Z. W. Lu, S. Froyen, and A. Zunger, "Zinc-blende — wurtzite polytypism in semiconductors," *Physical Review B*, vol. 46, no. 16, pp. 10 086–10 097, 1992.

[86] D. R. Lide, Ed., *Handbook of Chemistry and Physics*, 85th ed. CRC Press.

[87] Y. Chen, L. Zhang, J. Zhang, P. Liu, T. Zhou, H. Zhang, D. Gong, D. Tang, and D. Shen, "Fabrication of transparent ZnS ceramic by optimizing the heating rate in spark plasma sintering process," *Optical Materials*, vol. 50, pp. 36–39, 2015.

[88] Y. Uehara, "Electronic structure of luminescence center of ZnS:Ag phosphors," *The Journal of Chemical Physics*, vol. 62, no. 8, pp. 2982–2994, 1975.

[89] S. Wageh, Z. S. Ling, and X. Xu-Rong, "Growth and optical properties of colloidal ZnS nanoparticles," *Journal of Crystal Growth*, vol. 255, no. 3, pp. 332–337, 2003.

[90] F. A. Kröger and H. J. Vink, "The Origin of the Fluorescence in Self-Activated ZnS, CdS, and ZnO," *The Journal of Chemical Physics*, 1954.

[91] J. McCloy and R. Tustison, *Chemical vapor deposited zinc sulfide*. SPIE, 2013.

[92] T. Yanagida, Y. Fujimoto, and S. Yanagida, "Evaluation of undoped zinc sulfide crystal scintillator," in *IEEE Nuclear Science Symposium Conference Record*, 2013.

[93] T. Koda and S. Shionoya, "Nature of the Self-Activated Blue Luminescence Center in Cubic ZnS:Cl Single Crystals," *Physical Review*, vol. 136, no. 2A, pp. A541–A555, 10 1964.

[94] J. C. Lee and D. H. Park, "Self-defects properties of ZnS with sintering temperature," *Materials Letters*, 2003.

[95] A. N. Georgobiani, M. S. Kotlyarevskii, V. N. Mikhalenko, and Y. V. Shvetsov, "Nature of luminescence in zinc sulfide with intrinsic-defect hole conductivity," *Journal of Applied Spectroscopy*, vol. 35, no. 4, pp. 1097–1100, 10 1981.

[96] D. Gao and T. S. Stefanik, "Transparent zinc sulfide processed from nanocrystalline powders," in *SPIE 8708, Window and Dome Technologies and Materials XIII*, 2013, pp. 1–87 080.

[97] C. Li, T. Xie, J. Dai, H. Kou, Y. Pan, and J. Li, "Hot-pressing of zinc sulfide infrared transparent ceramics from nanopowders synthesized by the solvothermal method," *Ceramics International*, vol. 44, no. 1, pp. 747–752, 2018.

[98] "Crystallography Open Database: Search."

[99] K. Kanaya and S. Okayama, "Penetration and Energy-Loss Theory of Electrons in Solid Targets," *Journal of Physics D: Applied Physics*, vol. 5, 1972.

[100] G. H. Bertrand, M. Hamel, S. Normand, and F. Sguerra, "Pulse shape discrimination between (fast or thermal) neutrons and gamma rays with plastic scintillators: State of the art," *Nuclear Instruments and Methods in Physics Research Section A: Accelerators, Spectrometers, Detectors and Associated Equipment*, vol. 776, pp. 114–128, 3 2015.

[101] E. A. Lorch, "Neutron Spectra of Am-241/B, Am-241/Be, Am-241/F, Cm-242/Be, Pu-238/C-13 and Cf-252 Isotopic Neutron Sources," *International Journal of Applied Radiation and Isotopes*, vol. 24, pp. 585–591, 1973.

[102] H. Kluge and K. Weise, "The Neutron Energy Spectrum of a Am-241-Be (α,n) Source and Resulting Mean Fluence to Dose Equivalent Conversion Factors," *Radiation Protection Dosimetry*, vol. 2, no. 2, pp. 85–93, 1982.

[103] N. Zaitseva, L. Carman, A. Glenn, J. Newby, M. Faust, S. Hamel, N. Cherepy, and S. Payne, "Application of solution techniques for rapid growth of organic crystals," *Journal of Crystal Growth*, vol. 314, no. 1, pp. 163–170, 1 2011.

[104] A. Ghassemi, K. Sato, K. Kobayashi, Y. Ohashi, Y. Enomoto, and Y. Adachi, "MPPC," Hamamatsu, Tech. Rep.

[105] M. Debenham, "Refractive indices of zinc sulfide in the 0405–13-μm wavelength range," *Applied Optics*, vol. 23, no. 14, p. 2238, 7 1984.

[106] F. Schneider, J. Draheim, R. Kamberger, and U. Wallrabe, "Process and material properties of polydimethylsiloxane (PDMS) for Optical MEMS," *Sensors and Actuators A: Physical*, vol. 151, no. 2, pp. 95–99, 4 2009.

[107] A. Yoffe, "Low-dimensional systems: quantum size effects and electronic properties of semiconductor microcrystallites (zero-dimensional systems) and some quasi-two-dimensional systems," *Advances in Physics*, vol. 42, no. 2, pp. 173–262, 4 1993.

[108] W. Chen, Z. Wang, Z. Lin, and L. Lin, "Absorption and luminescence of the surface states in ZnS nanoparticles," *Journal of Applied Physics*, vol. 82, no. 6, p. 3111, 8 1998.

[109] K. B. Lin and Y. H. Su, "Photoluminescence of Cu:ZnS, Ag:ZnS, and Au:ZnS nanoparticles applied in Bio-LED," *Applied Physics B: Lasers and Optics*, 2013.

[110] V. Ramasamy, K. Praba, and G. Murugadoss, "Synthesis and study of optical properties of transition metals doped ZnS nanoparticles," *Spectrochimica Acta Part A: Molecular and Biomolecular Spectroscopy*, vol. 96, pp. 963–971, 10 2012.

[111] P. Yang, C. Song, M. Lu È, G. Zhou, Z. Yang, D. Xu, and D. Yuan, "Photoluminescence of Cu^{+}-doped and Cu^{2+}-doped ZnS nanocrystallites," *Journal of Physics and Chemistry of Solids*, vol. 63, pp. 639–643, 2002.

[112] P. Yang, M. Lü, D. Xü, D. Yuan, and G. Zhou, "Photoluminescence properties of ZnS nanoparticles co-doped with Pb^{2+} and Cu^{2+}," *Chemical Physics Letters*, 2001.

[113] K. Era, S. Shionoya, Y. Wasfflzawa, and H. Ohmatsu, "Mechanism of broadband luminescences in ZnS phosphors—II. Characteristics of pair emission type luminescences," *Journal of Physics and Chemistry of Solids*, vol. 29, no. 10, pp. 1843–1857, 10 1968.

[114] A. Fakhri and R. Khakpour, "Synthesis and characterization of carbon or/and boron-doped CdS nanoparticles and investigation of optical and photoluminescence properties," *Journal of Luminescence*, vol. 160, pp. 233–237, 2015.

[115] M. Angelone, M. Pillon, R. Faccini, D. Pinci, W. Baldini, R. Calabrese, G. Cibinetto, A. Cotta Ramusino, R. Malaguti, and M. Pozzati, "Silicon photo-multiplier radiation hardness tests with a beam controlled neutron source," *Nuclear Instruments and Methods in Physics Research Section A: Accelerators, Spectrometers, Detectors and Associated Equipment*, vol. 623, no. 3, pp. 921–926, 11 2010.